Late Pleistocene Orbital-Scale Indian Summer Monsoon Hydroclimates Reconstructed Using Leaf Wax Hydrogen and Carbon Isotopes from the Northeast Indian Margin and Andaman Sea

by

Sarah M. McGrath

B.A., The College of Wooster, 2017

M.Sc., Brown University, 2019

A dissertation submitted in partial fulfillment of the requirements for the degree of Doctor of Philosophy in the Department of Earth, Environmental and Planetary Sciences at Brown University

Providence, Rhode Island, USA

October 2022

SIGNATURE PAGE

This dissertation by Sarah M. McGrath is accepted in its present form

by the Department of Earth, Environmental, and Planetary Sciences as satisfying the

dissertation requirement for the degree of Doctor of Philosophy.

Date: _______________ _____________________________________

Steven C. Clemens, Ph.D., Advisor

Date: _______________ _____________________________________

Yongsong Huang, Ph.D., Advisor

Recommended to the Graduate Council

Date: _______________ _____________________________________

Pallavi Anand, Ph.D., Reader

Date: _______________ _____________________________________

Colleen Dalton, Ph.D., Reader

Date: _______________ _____________________________________

Timothy Herbert, Ph.D., Reader

Date: _______________ _____________________________________

James Russell, Ph.D., Reader

Approved by the Graduate Council

Date: _______________ _____________________________________

Thomas A. Lewis, Dean of the Graduate School

CURRICULUM VITAE

Sarah McGrath
Department of Earth, Environmental, and Planetary Sciences
Brown University • Providence, RI 02906
sarah_mcgrath@brown.edu

EDUCATION

Brown University, Providence, Rhode Island

2022 Ph.D. in Earth, Environmental, and Planetary Sciences

2019 MSc in Earth, Environmental, and Planetary Sciences, GPA: 4.0/4.0
Thesis title: *Indian summer monsoon rainfall variability over the last glacial- interglacial period*

The College of Wooster, Wooster, Ohio

2017 BA in Geology *summa cum laude* with Math minor, GPA: 3.975/4.0
Thesis title: *Western tropical Atlantic hydrology changes during abrupt climate events in the last glacial interval*

RESEARCH EXPERIENCE

Graduate Research

2017 to present **Paleoclimate Research**: co-advised by Steven Clemens and Yongsong Huang

- Investigating Indian summer monsoon rainfall variability and forcing mechanisms over millennial and orbital timescales using multi-proxy approach.
- Projects include:
  - Reconstructing orbital scale precipitation isotopes and environmental change through leaf wax δD and vegetation changes through leaf wax $\delta^{13}C$.
  - Analyzing millennial scale variability in sea water isotopes through foraminifera $\delta^{18}O$ and Mg/Ca analysis with comparison to precipitation isotope proxies (speleothem $\delta^{18}O$ and leaf wax δD).
  - Examining modern precipitation isotopes to ground truth precipitation isotope proxies
- Expanding the limits of alkenone sea surface temperature proxies through modern core top and Plio-Pleistocene down core studies.
  - Mentored two undergraduate students, empowering them to execute independent publishable research projects and publish a paper

2019 Summer **Sedimentologist** on *RV Joides Resolution* Expedition 379T, JR100 program

- Sailed in the South Pacific as a member of the team describing and analyzing marine sediment cores

Undergraduate Research

2016 to 2017 **Independent Study**, earned Honors, Geology Department, College of Wooster

- Paleoclimate and paleoceanography research: mentored by Dr. Mark Wilson and Dr. Delia Oppo
- Wrote capstone thesis based on summer student fellowship research.

2016 Summer **Summer Student Fellow**, Woods Hole Oceanographic Institution

- Paleoclimate and paleoceanography research: mentored by Dr. Delia Oppo
- Researched western tropical Atlantic Ocean hydrology changes during abrupt climate changes in the last glacial interval though an ocean sediment core, running planktic foraminifera isotope and XRF analysis.

2015 Summer **Lamont-Doherty Earth Observatory Summer Intern**, Columbia University

- Paleoclimate and paleoceanography research: mentored by Dr. Jerry McManus and Allison Jacobel
- Conducted a geochemical signature comparison of *Globigerinoides ruber* chromotypes through isotopic, elemental, and radiocarbon analysis.

2014 to 2016 **Clare Boothe Luce Research Scholar**, College of Wooster

- Dendrochronology research: mentored by Dr. Greg Wiles
  - Alaskan Yellow Cedar Project: investigated the response of yellow cedar to a changing climate over the last 1,000 years
  - Geoarchaeology Project: through tree ring dating, studied the native Tlingit movements and cultural changes
- Paleosol research: mentored by Dr. Shelley Judge
  - Conducted field work in Sanpete Valley, Utah examining and collecting, paleosol rocks that were from the Paleocene-Eocene Thermal Maximum

2014 Spring **Research Assistant**, Geology Department, College of Wooster

- Structural geology research: mentored by Dr. Shelley Judge Initiated project to investigate fluid composition within a sandstone.

TEACHING EXPERIENCE

Spring 2022 **Seminar for Transformation around Anti-Racist Teaching (START) Fellow**

- Graduate fellow for the change team in the Department of Earth, Environmental, and Planetary Sciences (DEEPS) for the START program hosted by the Sheridan Center for Teaching and Learning at Brown University.
- Facilitated departmental efforts to advance inclusive and anti-racist change work in teaching, learning, and curriculum development.

Fall 2021 **Teaching Assistant**, Introduction to Oceanography, Brown University

- Introductory level Earth Science course for primarily non-majors that examines the ocean's role in Earth's global environment, emphasizing the dynamical interaction of the ocean with the atmosphere, biosphere, cryosphere, and lithosphere.
- Responsible for assisting in daily class activities and field trips, holding office hours and review sessions, creating assignments, and grading.

Fall 2021 **Experienced Sheridan Teaching Consultant**

- Invited to return as a Sheridan Teaching Consultant, based on the positive reviews from participants in Fall 2020. As an experienced Sheridan Teaching Consultant, I am a leader, guiding new Teaching Consultants through the program.
- Facilitated 8 workshops for Sheridan Teaching Seminar.

Spring 2021 **Sheridan Course Design Seminar**

- Explored integrated course design principles and developed 2 syllabi complete with sample assignments and activities for college-level courses.
- Learned how to create student-centered learning outcomes, creating assessments and scaffolding learning activities to support the course goals.

Fall 2020 **Sheridan Teaching Consultant**

- Expanded on knowledge of research-based teaching practices and philosophies.
- Lead 6 workshops for Sheridan Teaching Seminar, refining skills in workshop facilitation, discussion, and providing feedback.

Spring 2020 **Teaching Assistant**, Earth: Evolution of a Habitable Planet, Brown University

- Introductory level Earth Science course for majors that examines the Earth system through climate, chemistry, and physical makeup.
- Taught lab sections, held office hours and review sessions, graded assignments, and aided in shifting class to fully remote learning.

- Oversaw 4 undergrad Teaching Assistants.

Fall 2018 **Sheridan Teaching Seminar in Reflective Teaching**

- Developed fundamental, evidence-based teaching skills and strategies that include establishing inclusive learning environments, practicing public speaking, applying principles of learning design, exploring methods of evaluating learning, and investigating active learning activities that lead to lasting and deep forms of learning.

Fall 2016 **Teaching Assistant**, Mathematical Modeling, College of Wooster

- Upper-level math course in analyzing mathematical models through computational tools to construct mathematical models and test their validity against empirical data.
- Assisted in classroom activities, held office hours, and taught students how to code and problem solve in MATLAB.

2016 to 2017 **Peer Tutor**, Geology, College of Wooster

- Learned about different teaching and tutoring strategies.
- Tutored in one-on-one sessions and developed personalized learning plans.

Fellowships, Grants, and Awards

2022	START Fellow, Sheridan Center for Teaching and Learning, Brown University
2021	Dissertation Fellowship, DEEPS, Brown University
2021	IBES Research, Training, and Travel Award, Brown University
2020 to 2021	Schlanger Ocean Drilling Fellowship**,** U.S. Science Support Program
2019	GSA Graduate Research Grant, Geologic Society of America
2019	IBES Research, Training, and Travel Award, Brown University
2017 to 2018	First Year Fellowship, DEEPS, Brown University
2018 & 2017	NSF Graduate Research Fellowship Program Honorable Mention
2017	Endowed Faculty Scholarship, College of Wooster
2015 to 2017	Goldwater Scholarship, Barry Goldwater Scholarship Program
2014 to 2016	Clare Boothe Luce Scholarship for Women in STEM
2014 to 2016	Named Endowed Scholarships including Charles B. Moke, Margaret Kate Moke, Margaret Reed, & John O. Clay Endowed Scholarships, Wooster Geology
2013 to 2016	Scholar of Distinction & National Academic Squad, DIII Field Hockey

Publications

McGrath, S. M., Clemens, S. C., Huang, Y., & Yamamoto, M. (2021). Greenhouse gas and ice volume drive Pleistocene Indian Summer Monsoon precipitation isotope variability. *Geophysical Research Letters*, 48, e2020GL092249. https://doi.org/10.1029/2020GL092249

Clemens, S. C., Yamamoto, M., Thirumalai, K., Giosan, L., Richey, J. N., Nilsson-Kerr, K., Rosenthal, Y., Anand, P., McGrath, S. (2021). Remote and Local Drivers of Pleistocene South Asian Summer Monsoon Precipitation: A Test for Future Predictions. *Science Advances*, 7, eabg3848. https://doi.org/10.1126/sciadv.abg3848

Novak, J.*, McGrath, S.M., Wang, K. J., Lao, S., Clemens, S.C., Kuhnt, W., Huang, Y. (2022) $U^{K'}_{38ME}$ Expands the Linear Dynamic Range of the Alkenone Sea Surface Temperature Proxy, *Geochimica et Cosmochimica Acta*. *https://doi.org/10.1016/j.gca.2022.04.021* .
*Indicates undergrad mentee

Presentations and Published Abstracts:

Orbital Scale Indian Summer Monsoon Precipitation Isotopes over the last 640 kyr. *American Geophysical Union Fall Meeting*, New Orleans, LA, 2021 oral presentation, Sarah McGrath, Steve Clemens, and Yongsong Huang.

What Drives the Indian Summer Monsoon? New Perspectives from the Bay of Bengal. *U.S. Advisory Committee for Scientific Ocean Drilling (USAC) Meeting*, virtual, 2021 oral presentation, Sarah McGrath.

Greenhouse Gas and Ice Volume Drive Pleistocene Indian Summer Monsoon Precipitation Isotope Variability. *American Geophysical Union Fall Meeting*, virtual, 2020 oral presentation, Sarah McGrath, Steve Clemens, Yongsong Huang, and Masanobu Yamamoto.

The Indian Summer Monsoon Over the Past 640,000 Years: Reconstructed from $\delta D_{\text{leaf wax}}$. *AGU Chapman Conference on the Evolution of the Monsoon, Biosphere and Mountain Building in Cenozoic Asia*, Washington, D.C., 2020 oral presentation, Sarah McGrath, Steve Clemens, Yongsong Huang, and Masanobu Yamamoto.

The Indian Summer Monsoon Over the Past 640,000 Years: Reconstructed from $\delta D_{\text{leaf wax}}$. *American Geophysical Union Fall Meeting*, San Francisco, CA, 2019 oral presentation, Sarah McGrath, Steve Clemens, Yongsong Huang, and Masanobu Yamamoto.

Indian Summer Monsoon Rainfall Reconstruction over the past 640 kyr. *Graduate Climate Conference*, Woods Hole, MA, 2019 poster presentation, Sarah McGrath, Steve Clemens, Yongsong Huang, and Masanobu Yamamoto.

The Indian Summer Monsoon Over the Past 640,000 Years: Reconstructed from $\delta D_{\text{leaf wax}}$. *Water Isotopes and Climate Workshop*, Boulder, CO, 2019 poster presentation, Sarah McGrath, Steve Clemens, Yongsong Huang, and Masanobu Yamamoto.

Indian Summer Monsoon Paleohydrology Reconstruction from U1446 $\delta D_{\text{leaf wax}}$. *Goldschmidt Conference*, Boston, MA 2018, accepted (but not delivered), Sarah McGrath, Steve Clemens, Yongsong Huang, and Masanobu Yamamoto.

Western Tropical Atlantic Hydrologic change during the last 130,000 years. *2016 American Geophysical Union Fall Meeting*, San Francisco, CA, 2016 poster presentation, Sarah McGrath, Nicholas Lavoie, and Delia Oppo.

Examining the Effects of a Changing Climate on Alaska Yellow Cedar: Analyses of Ring Width and Blue Intensity Tree Ring Chronologies. *Geological Society of America Annual Meeting*, Denver, CO, 2016 poster presentation, Sarah McGrath, Eduardo Luna, Nick Wiesenberg, and Gregory Wiles.

Geochemical comparison of pink and white *Globigerinoides ruber*: Investigating habitat niches and their paleoclimatic significance. *Geological Society of America Annual Meeting*, Baltimore, MD, 2015 poster presentation, Sarah McGrath, Allison Jacobel, and Jerry McManus.

Three Hundred Years of Continuity: A Yellow Cedar Bark Stripping Site on Pleasant Island, Icy Strait, Southeast Alaska. *Geological Society of America Annual Meeting*, Vancouver, British Columbia, Canada, 2014 oral presentation, Sarah McGrath, Wayne Howell, Nick Wiesenberg, Colin Mennett, and Gregory Wiles.

Outreach and Service

2021	Unlearning Racism in the Geosciences (URGE) DEEPS pod member
2020 to 2022	First Year Mentoring Coordinator
2018 to 2019	GeoClub Co-President, Brown University
2017 to 2019	Volunteer for DEEPS Student Teaching Education Program (STEP)
2017 to present	Member of Graduate Women in Science and Education (GWISE)
2016 to 2017	Geology Club President, The College of Wooster

Professional Affiliations and Honor Societies:

Institute at Brown for Environment and Society (IBES),
American Geophysics Union (AGU),
Geological Society of America (GSA),
Sigma Xi,
Phi Beta Kappa,
Pi Mu Epsilon,
National Honor Society.

ACKNOWLEDGEMENTS

This research was made possible by grant funding from National Science Foundation, Schlanger Ocean Drilling Fellowship, Institute at Brown for Environment and Society, and the Geological Society of America.

I would like to thank my advisors Steven Clemens and Yongsong Huang for their mentorship and support. I thank Ewerton Santos, Marcelo Alexandre, and Joe Orchardo for their lab management and help with the isotope ratio mass spectrometers.

Thank you to my family for always supporting and encouraging me.

Table of Contents

LIST OF TABLES

CHAPTER 1:

CHAPTER 2:

CHAPTER 3:

LIST OF ILLUSTRATIONS

CHAPTER 1:

CHAPTER 2:

CHAPTER 3:

INTRODUCTION

Indian summer monsoon rainfall is a critical source of water for Southeast Asia, the most densely populated area of the world accounting for over a fifth of the world's population (UN, 2017). Variability of Indian summer monsoon rainfall can be disastrous, leading to flooding or droughts. Projections of changes in Indian summer monsoon rainfall is a key challenge for global and regional circulation models (Asharaf & Ahrens, 2015; Shukla, 2007; B. Wang et al., 2015), particularly under climate change scenarios. To understand Indian summer monsoon rainfall variability, we need to understand the forcing mechanisms.

I turn to paleoclimate studies to understand Indian summer monsoon driving mechanisms over timescales with large scale climate forcings. Study of orbital-scale climate change over the Late Pleistocene is unique; the external forcing function, insolation, is known (Berger, 1978; Laskar et al., 1993), and two of the critical internal forcing functions, greenhouse gases and terrestrial ice volume, are well-constrained from ice core and benthic foraminifera oxygen isotope records respectively (Lisiecki & Raymo, 2005; Loulergue et al., 2008; Petit et al., 1999). Conducting spectral analysis of monsoon proxy records relative to external insolation and internal forcing mechanisms allows one to test the possible physical mechanisms underlying monsoon variability. Spectral power, as a function of frequency indicates relative influence of the orbital cycles in a proxy record. Coherence is a measure of the linear relationship between two records, as a function of frequency. Phase indicates the temporal leads and lags critical to understand forcing and response relationships. Hence, it is possible to ascertain the relative influence of these internal and external drivers on monsoonal circulation.

Two prominent, but opposing hypotheses on the mechanisms controlling the Asian monsoon system on orbital time scales have been developed from early proxy records: the Arabian sea wind/upwelling proxy stacks (Caley et al., 2011; Clemens & Prell, 2003) and East Asian speleothems (Cheng et al., 2016; Y. Wang et al., 2008), with divergent implications on the sensitivity of monsoonal circulation to changes in high latitude and greenhouse gas forcing. The first hypothesis, based largely upon the early Arabian Sea proxy records, suggested that monsoon changes are strongly coupled to internal climate dynamics. The timing of the strongest monsoon circulation is sensitive to latent heat imported from the southern hemisphere, greenhouse gas concentrations, and high-latitude ice volume (Caley et al., 2011; Clemens & Prell, 2003). The second hypothesis, based on East Asian speleothem $\delta^{18}O$, posits that external insolation forcing is the primary driver of monsoon intensity. This suggests that the monsoon “intensity” and rainfall is strongest during times with the highest incoming solar radiation during Boreal summer (Cheng et al., 2016; Y. Wang et al., 2008). These divergent results and interpretations suggest that the monsoon systems over Indian and East Asia are uncoupled, that proxy interpretations are incorrect, or some combination thereof.

The Bay of Bengal, the core convective region of summer monsoon rainfall, lies geographically between the Arabian Sea wind/upwelling and East Asian speleothem sites. Recently collected marine sediment cores offer an unprecedented opportunity to examine these divergent hypotheses by investigating hydrologic changes surrounding and within the Bay of Bengal. These sites offer the first opportunity to develop orbital-scale marine and terrestrial proxies at the same site for the Indian Summer Monsoon that capture multiple aspects of the monsoon variability including runoff, sea surface salinity, sea surface temperature, precipitation isotopes and vegetation changes.

IODP Expedition 353 (Clemens, Kuhnt, & LeVay, 2016) recovered sediment from Indian margin Site U1446 (19°5.0'N, 85°44.0'E, 1440mbsl, 70km offshore) located near the mouth of the Mahanadi River (western Bay of Bengal) (Clemens, Kuhnt, LeVay, & Scientists, 2016). This site targets hydrologic and environmental changes from the Mahanadi River Basin and drainage basins in northern Bay of Bengal. During the monsoon summer season, the Mahanadi River Basin receives over 90% of the total annual rainfall with monthly precipitation averages about 300mm of rain and the average temperature is about 28°C (Mitchell & Jones, 2005). Site U1446 has a remarkable, turbidite free continuous stratigraphy.

Site U1448 (10°38.0'N, 93°00.0'E, 1091mbsl, 44km offshore) is located on a rise in the Andaman Sea (eastern Bay of Bengal) (Clemens et al., 2016). This site targets hydrologic and environmental changes from the Irrawaddy basin, Salween basin, and Andaman Islands. These areas experience over 90% of total annual rainfall during the summer monsoon season with about 500 mm of rain per month and an average temperature of 28°C (Mitchell & Jones, 2005). Terrigenous sediment supply to the Andaman Sea is dominantly from the Irrawaddy and Salween Rivers (Colin et al., 1999, 2006) with contributions from the Indo-Burman-Arakan mountain ranges as well as the Andaman Islands (Awasthi et al., 2014). Site U1448 benthic foraminifera $\delta^{18}O$ record demonstrates a complete, continuous stratigraphy. Sea surface salinity (SSS; $\delta^{18}O_{seawater}$) and sea surface temperature (SST; derived from $\delta^{18}O$ and Mg/Ca analysis) proxy records have been recently published from nearby site NGHP-17 (Gebregiorgis et al., 2018). However, NGHP-17 is a relatively low-resolution record with discontinuities related to drilling only a single hole. Site U1448 (multiple offset holes with a complete section) is ideally located (near NGHP-17) allowing for us to build upon the published $\delta^{18}O_{seawater}$ record using additional proxies at a higher resolution.

Here I create proxy records of precipitation isotopes and vegetation from leaf waxes. Long-chain (>n-C_{25}) lipid *n*-alkanoic acids, components of waxy coatings on terrestrial plant leaves, are transported into the ocean and are preserved in sediments (Sachse et al., 2012). Both Sites U1446 and U1448 collect leaf wax fatty acids from large catchment basins: western Bay of Bengal Site U1446 from the Mahanadi River Basin along with the Ganges-Brahmaputra River basin and Andaman Sea Site U1448 from the proximal Andaman Islands, Irrawaddy River, and Salween River basins. Integrating leaf waxes from a large catchment reduces the variability from different vegetation or microclimates, providing larger-scale, integrated climate signals (Douglas et al., 2012). In the Ganges-Brahmaputra basin fatty acid leaf waxes have short residence times (from 0.015 to 1.2 kyr) (French et al., 2018; Galy & Eglinton, 2011). Leaf wax hydrogen isotopes (δD_{wax}) is a proxy for precipitation isotopes (δD_{precip}) which record changes in monsoonal precipitation, moisture source and transport dynamics. Leaf wax carbon isotopes ($\delta^{13}C_{wax}$) is a proxy for vegetation change as a function of C_3/C_4 proportion. Study of modern δD_{wax} and $\delta^{13}C_{wax}$ in the Ganges–Brahmaputra basin has been demonstrated as a reliable proxy for basin-integrated δD_{precip} and $\delta^{13}C_{wax}$, respectively (Galy et al., 2011).

Through construction of late-Pleistocene orbital scale δD_{wax} and $\delta^{13}C_{wax}$ records, I investigate the drivers and mechanisms that influence Indian Summer Monsoon variability. In Chapter one, I create a δD_{precip} record from Site U1446. I interpret δD_{precip} as a proxy for monsoon circulation encompassing changes in precipitation, moisture source, and moisture transport dynamics. I find that Indian Summer Monsoon precipitation isotope proxies, including both speleothems and leaf wax proxies, are quantitatively coherent and show a consistent response to greenhouse gas and ice volume forcing. Additionally, I observe that orbital scale Indian and East Asian monsoon precipitation isotopes are uncoupled, responding differently to internal and external forcings.

In Chapter two, I create a δD_{wax} record from Site U1448 to study precipitation isotope gradients across the Bay of Bengal. Compared to U1446 $\delta D_{wax\text{-}veg}$, I find that U1448 $\delta D_{wax\text{-}veg,}$ has half the glacial-interglacial variability, and lacks large obliquity and precession spectra power variability suggesting a more stable, proximal moisture source feeds the Indian Summer Monsoon branch over Andaman Islands, Irrawaddy River, and Salween River basins. This proxy spatial pattern is opposite of the modeled precipitation isotopes, which suggest the Indian Summer Monsoon branch over Andaman Islands, Irrawaddy River, and Salween River basins exhibits larger orbital scale precipitation isotope changes than the core monsoon zone (Hu et al., 2019; Tabor et al., 2018). I find the stable water isotope tracer-enabled version of the Community Earth System Model (iCESM) consistently underestimates precipitation isotope ranges and does not replicate proxy precipitation isotope gradients across the Bay of Bengal over orbital timescales.

In Chapter three, I create a $\delta^{13}C_{wax}$ record at Site U1448 to study Southeast Asian vegetation variability. I find an expansion of C_4 vegetation during glacial periods since 250 ka across the Southeast Asian peninsula and maritime continent. This C_4 expansion is driven by submersion of the Sunda Shelf and an enhanced El Nino- like climate state that promotes relatively drier, warmer Indian Summer Monsoon during glacial intervals.

Taken together, these results show the Indian Summer Monsoon is primarily driven by internal climate feedbacks - not solely by external insolation forcing. These late Pleistocene orbital scale Indian Summer Monsoon reconstructions provide insights on how the Indian Summer Monsoon will change with modern climate change. The precipitation isotope reconstructions indicate that with increased radiative forcing from greenhouse gasses and less ice volume, monsoon circulation will strengthen bringing more moisture and precipitation from the Southern Indian Ocean to the core monsoon zone. The carbon isotopes C_3/C_4 vegetation reconstruction indicate that with more frequent or intense El Nino events and warmer tropical Indian Ocean Sea surface temperatures, the Indian Summer Monsoon will weaken, threatening the C_3 dominating tropical forests and favoring the expansion of C_4 plants.

References

Asharaf, S., & Ahrens, B. (2015). Indian summer monsoon rainfall processes in climate change scenarios. *Journal of Climate*, 28(13), 5414–5429. https://doi.org/10.1175/JCLI-D-14-00233.1

Awasthi, N., Ray, J. S., Singh, A. K., Band, S. T., & Rai, V. K. (2014). Provenance of the Late Quaternary sediments in the Andaman Sea: Implications for monsoon variability and ocean circulation. *Geochemistry, Geophysics, Geosystems*, 15(10), 3890–3906. https://doi.org/10.1002/2014GC005462

Berger, A. L. (1978). Long-Term Variations of Caloric Insolation Resulting from the Earth's Orbital Elements. *Quaternary Research*, 9(02), 139–167. https://doi.org/10.1016/0033-5894(78)90064-9

Caley, T., Malaizé, B., Zaragosi, S., Rossignol, L., Bourget, J., Eynaud, F., et al. (2011). New Arabian Sea records help decipher orbital timing of Indo-Asian monsoon. *Earth and Planetary Science Letters*, 308(3–4), 433–444. https://doi.org/10.1016/J.EPSL.2011.06.019

Cheng, H., Edwards, R. L., Sinha, A., Spötl, C., Yi, L., Chen, S., et al. (2016). The Asian monsoon over the past 640,000 years and ice age terminations. *Nature*, 534(7609), 640–646. https://doi.org/10.1038/nature18591

Clemens, S. C., & Prell, W. L. (2003). A 350,000 year summer-monsoon multi-proxy stack from the Owen Ridge, Northern Arabian Sea. *Marine Geology*, 201(1–3), 35–51. https://doi.org/10.1016/S0025-3227(03)00207-X

Clemens, S. C., Kuhnt, W., LeVay, L. J., & Scientists, E. 353. (2016). Site U1446. *Proceedings of the International Ocean Discovery Program*, 353. https://doi.org/10.14379/iodp.proc.353.106.2016

Clemens, S. C., Kuhnt, W., LeVay, L. J., Anand, P., Ando, T., Bartol, M., et al. (2016). Site U1448. *Proceedings of the International Ocean Discovery Program*, 353. https://doi.org/10.14379/iodp.proc.353.108.2016

Clemens, S. C., Kuhnt, W., & LeVay, L. J. (2016). Volume 353: Indian Monsoon Rainfall. *Proceedings of the International Ocean Discovery Program*, 353. https://doi.org/10.14379/IODP.PROC.353.2016

Colin, C., Turpin, L., Bertaux, J., Desprairies, A., & Kissel, C. (1999). Erosional history of the Himalayan and Burman ranges during the last two glacial–interglacial cycles. *Earth and Planetary Science Letters*, 171(4), 647–660. https://doi.org/10.1016/S0012-821X(99)00184-3

Colin, C., Turpin, L., Blamart, D., Frank, N., Kissel, C., & Duchamp, S. (2006). Evolution of weathering patterns in the Indo-Burman Ranges over the last 280 kyr: Effects of sediment provenance on 87 Sr/86 Sr ratios tracer. *Geochemistry, Geophysics, Geosystems*, 7(3), 1–16. https://doi.org/10.1029/2005GC000962

Douglas, P. M. J., Pagani, M., Brenner, M., Hodell, D. A., & Curtis, J. H. (2012). Aridity and vegetation composition are important determinants of leaf-wax δD values in southeastern Mexico and Central America. *Geochimica et Cosmochimica Acta*, 97, 24–45. https://doi.org/10.1016/j.gca.2012.09.005

French, K. L., Hein, C. J., Haghipour, N., Wacker, L., Kudrass, H. R., Eglinton, T. I., & Galy, V. (2018). Millennial soil retention of terrestrial organic matter deposited in the Bengal Fan. *Scientific Reports*, 8(1). https://doi.org/10.1038/s41598-018-30091-8

Galy, V., & Eglinton, T. (2011). Protracted storage of biospheric carbon in the Ganges–Brahmaputra basin. *Nature Geoscience*, 4(12), 843–847. https://doi.org/10.1038/ngeo1293

Galy, V., Eglinton, T., France-Lanord, C., & Sylva, S. (2011). The provenance of vegetation and environmental signatures encoded in vascular plant biomarkers carried by the Ganges-Brahmaputra rivers. *Earth and Planetary Science Letters*, 304(1–2), 1–12. https://doi.org/10.1016/j.epsl.2011.02.003

Gebregiorgis, D., Hathorne, E. C., Giosan, L., Clemens, S., Nürnberg, D., & Frank, M. (2018). Southern Hemisphere forcing of South Asian monsoon precipitation over the past ~1 million years. *Nature* Communications, 9(1), 4702. https://doi.org/10.1038/s41467-018-07076-2

Hu, J., Emile-Geay, J., Tabor, C., Nusbaumer, J., & Partin, J. (2019). Deciphering Oxygen Isotope Records From Chinese Speleothems With an Isotope-Enabled Climate Model. *Paleoceanography and Paleoclimatology*, 2019PA003741. https://doi.org/10.1029/2019PA003741

Laskar, J., Joutel, F., & Boudin, F. (1993). Orbital, precession, and insolation quantities for the Earth from -20Myr to +10 Myr. *Astronomy and Astrophysics*, 270, 522–533. https://doi.org/:10.1161/atvbaha.109.193201

Lisiecki, L. E., & Raymo, M. E. (2005). A Pliocene-Pleistocene stack of 57 globally distributed benthic $\delta^{18}O$ records. *Paleoceanography*, 20(1), 1–17. https://doi.org/10.1029/2004PA001071

Loulergue, L., Schilt, A., Spahni, R., Masson-Delmotte, V., Blunier, T., Lemieux, B., et al. (2008). Orbital and millennial-scale features of atmospheric CH_4 over the past 800,000 years. *Nature*, 453(7193), 383–386. https://doi.org/10.1038/nature06950

Mitchell, T. D., & Jones, P. D. (2005). An improved method of constructing a database of monthly climate observations and associated high-resolution grids. *International Journal of Climatology*, 25.

Petit, J. R., Jouzel, J., Raynaud, D., Barkov, N. I., Barnola, J.-M., Basile, I., et al. (1999). Climate and atmospheric history of the past 420,000 years from the Vostok ice core, Antarctica. *Nature*, 399(6735), 429–436. https://doi.org/10.1038/20859

Sachse, D., Billault, I., Bowen, G. J., Chikaraishi, Y., Dawson, T. E., Feakins, S. J., et al. (2012). Molecular Paleohydrology: Interpreting the Hydrogen-Isotopic Composition of Lipid Biomarkers from Photosynthesizing Organisms. *Annu. Rev. Earth Planet. Sci*, 40(1), 221–49. https://doi.org/10.1146/annurev-earth-042711-105535

Shukla, J. (2007). Monsoon mysteries. *Science*, 318(5848), 204–205. https://doi.org/10.1126/science.1150045

Tabor, C. R., Otto-Bliesner, B. L., Brady, E. C., Nusbaumer, J., Zhu, J., Erb, M. P., et al. (2018). Interpreting Precession-Driven $\delta^{18}O$ Variability in the South Asian Monsoon Region. *Journal of Geophysical Research: Atmospheres*, 123(11), 5927–5946. https://doi.org/10.1029/2018JD028424

UN. (2017). World population prospects: Data booklet 2017 Revision. *Population Division*, 1–24. Retrieved from https://esa.un.org/unpd/wpp/Publications/Files/WPP2017_DataBooklet.pdf

Wang, B., Xiang, B., Li, J., Webster, P. J., Rajeevan, M. N., Liu, J., & Ha, K. J. (2015). Rethinking Indian monsoon rainfall prediction in the context of recent global warming. *Nature Communications*, 6(1), 7154. https://doi.org/10.1038/ncomms8154

Wang, Y., Cheng, H., Edwards, R. L., Kong, X., Shao, X., Chen, S., et al. (2008). Millennial- and orbital-scale changes in the East Asian monsoon over the past 224,000 years. *Nature*, 451(7182), 1090–3. https://doi.org/10.1038/nature06692

CHAPTER 1:

Greenhouse Gas and Ice Volume Drive Pleistocene Indian Summer Monsoon Precipitation Isotope Variability

S. M. McGrath[1], S. C. Clemens[1], Y. Huang[1], and M. Yamamoto[2]

1 Department of Earth, Environmental, and Planetary Sciences, Brown University, Providence, Rhode Island, USA,

2 Graduate School of Environmental Earth Science, Hokkaido University, Sapporo, Japan

Published: *Geophysical Research Letters (2021), 48*(4).

https://doi.org/10.1029/2020GL092249

Key Points:

- Orbital scale Indian Summer Monsoon precipitation isotope record reconstructs precipitation, moisture source and transport dynamics
- Indian precipitation isotope proxies are quantitatively coherent and show a consistent response to greenhouse gas and ice volume forcing
- Orbital scale Indian and East Asian monsoon precipitation isotopes are uncoupled, responding differently to internal and external forcings

Abstract:

Orbital-scale Indian Summer Monsoon variability is often interpreted as a direct response to northern hemisphere summer insolation. Here we present a continuous (0-640 kyr) orbital scale precipitation isotope (δD_{precip}) record using leaf wax δD from the core monsoon zone of India. The δD_{precip} record is quantitatively coherent with, and δD_{precip} minima in phase with, greenhouses gas maxima, and ice volume minima across all orbital bands. The δD_{precip} record is also coherent and in phase with the two existing orbital-scale Indian speleothem $\delta^{18}O$ records, demonstrating a consistent regional response among independent proxies. These findings preclude interpretation of Indian precipitation isotope records as a direct response to northern hemisphere summer insolation. Rather, they dominantly reflect changes in moisture source and transport paths associated with changes in greenhouse gases and ice volume. The orbital-scale precipitation isotope responses of the Indian and East Asian monsoon systems are uncoupled and are driven by different forcings.

Plain Language Summary

Understanding the variability and forcing mechanisms of the Indian Summer Monsoon is a key socioeconomic concern. Late Pleistocene orbital-scale proxy records provide a unique opportunity to study monsoonal change since both external (insolation) and internal climate forcing functions (greenhouse gases and high-latitude ice volume) are well constrained. Here we present the first long, continuous orbital-scale precipitation isotope proxy record using leaf wax hydrogen isotopes. Precipitation isotopes reflect precipitation amount, moisture source, and moisture transport path dynamics making them ideal proxies for summer monsoon variability. We document a regionally consistent precipitation isotope signal driven by changes in greenhouse gas and ice volume. This diverges from previous studies that interpret the orbital-scale precipitation isotope signal as a direct response to external insolation forcing. Our findings are consistent with model results showing that anthropogenic increases in greenhouse gas will alter large-scale Indian Summer Monsoon circulation leading to increased precipitation and more distal moisture sources.

1. Introduction

Indian Summer Monsoon (ISM) variability is consequential, leading to flooding or droughts, and is tied to the socio-economic stability of India (Gadgil & Gadgil, 2006). Projecting changes in the ISM is a key challenge for global and regional circulation models (e.g., Asharaf & Ahrens, 2015; Seth et al., 2019; Shukla, 2007; Wang et al., 2015), particularly under future climate change scenarios. Orbital-scale proxy records over the Late Pleistocene provide a unique opportunity to study monsoonal change in which the external forcing function, insolation, is known (Berger, 1978; Laskar et al., 2004), and two of the critical internal forcing functions, greenhouse gases and terrestrial ice volume, are well constrained from ice core and benthic foraminifera $\delta^{18}O$ records respectively (Bereiter et al., 2015; Lisiecki & Raymo, 2005; Loulergue et al., 2008). The relative sensitivity of monsoonal proxy records to these external and internal drivers can be evaluated using cross-spectral analysis, a means of quantifying coherence and phase relationships among them.

Previous orbital-scale studies do not yield consistent interpretations with regard to the timing or causes of ISM variability. The phase of the Arabian Sea proxies suggests that the timing of the strongest summer monsoon winds is sensitive to latent heat imported from the southern hemisphere, greenhouse gas concentrations, and high-latitude ice volume and sea ice cover (Caley et al., 2011; Clemens & Prell, 2003). Runoff (Gebregiorgis et al., 2020) and wind-driven stratification proxies (Bolton et al., 2013) from the Bay of Bengal support these internal forcing inferences, providing evidence that ISM winds and precipitation are coupled at precession frequencies. However, both Bay of Bengal wind and runoff records have different obliquity phases compared to the Arabian Sea wind records.

Currently there exists two speleothem $\delta^{18}O$ records of sufficient length (~200 kiloyears; 200 kyr) to monitor orbital-scale ISM dynamics using time-series analytical approaches. Xiaobailong (XBL) speleothem $\delta^{18}O$ from southwestern China, shows precession and glacial-interglacial variability interpreted to reflect changes in regional ISM precipitation and variable moisture trajectories (Cai et al., 2015). Bittoo speleothem $\delta^{18}O$ from northwestern Indian Himalayan foothills, shows precession variability similar to that in the East Asian speleothem composite (Cheng et al., 2016); interpreted to reflect a consistent Indian and East Asian monsoon precipitation isotope response to northern hemisphere summer insolation forcing (Kathayat et al., 2016). Both XBL and Bittoo precession variability are interpreted as direct responses to northern hemisphere summer insolation forcing.

None of these proxies capture monsoon variability in the core monsoon zone (CMZ) of India, an area that receives significant summer monsoon rainfall and correlates to all-India summer monsoon rainfall (Gadgil, 2003). Here we present the first such proxy record, a precipitation isotope (δD_{precip}) record, based on leaf wax δD (Text S1), spanning the last 640 kyr from International Ocean Discovery Program Site U1446, northwestern

Bay of Bengal (Figure 1). We interpret the δD_{precip} variability to reflect ISM circulation; changes in precipitation, moisture source, and moisture transport dynamics. Hence, our use of the term “circulation” refers to the large-scale cross-equatorial overturning circulation of the atmosphere that carries moisture associated with monsoon rainfall.

Quantitative spectral analysis of the variance, coherence, and phase of δD_{precip} relative to existing records clarifies the sensitivity of Indian precipitation isotopes to external and internal climate forcing. The δD_{precip} response across precession and obliquity is consistent with that of the speleothem $\delta^{18}O$ records, all of which are in phase with greenhouse gas radiative forcing maxima and ice volume minima. This indicates large-scale ISM circulation encompassing precipitation, moisture source, and moisture transport changes are driven by the radiative forcing effects of greenhouse gasses and ice volume.

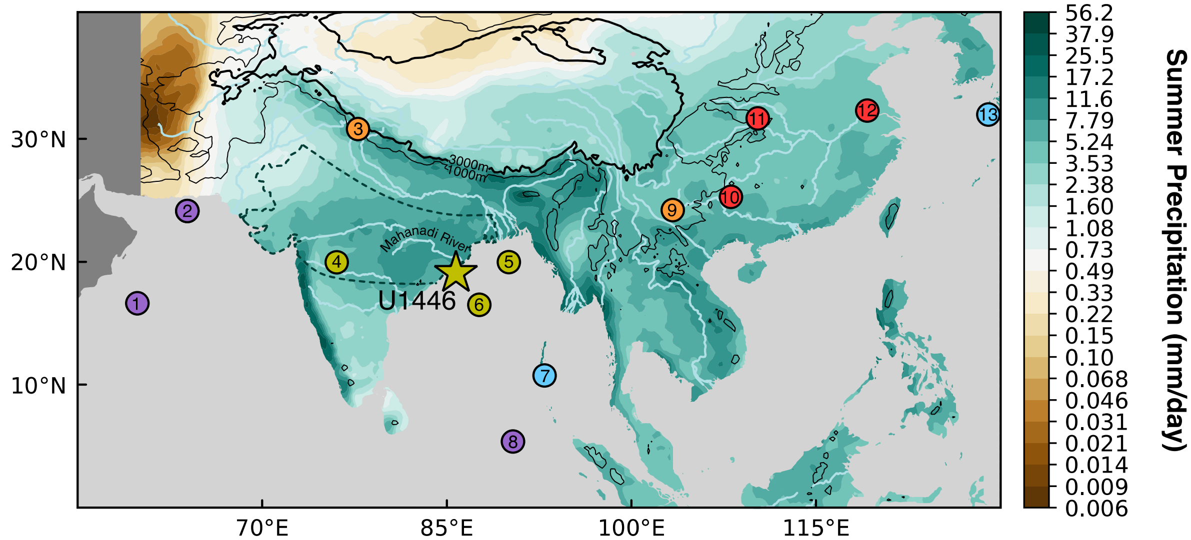

Figure 1.

Mean June-September precipitation from APHRODITE (mm day-1; 1998-2015; V1901) (Yatagai et al., 2012) plotted with a logarithmic scale. The dashed line outlines the CMZ of India (Gadgil, 2003) and star marks Site U1446. Dots are color-coded by proxy record type: yellow indicates δDwax, purple indicates wind, orange indicates ISM speleothems, red indicates East Asian summer monsoon speleothems, and blue indicates δ18Oseawater. Sites of 1) RC27-61 and 722B (Clemens & Prell, 2003) 2) MD04-2861 (Caley et al., 2011), 3) Bittoo Cave Speleothem (Kathayat et al., 2016), 4) Lonar Lake (Sarkar et al., 2015), 5) SO188-342 KL (Contreras-Rosales et al., 2014), 6) SO93-117 KL, SO93-118 KL, and SO93-120 KL (Hein et al., 2017), 7) NGHP 17 (Gebregiorgis et al., 2018), 8) Site 758 (Bolton et al., 2013), 9) Xiaobailong Cave (Cai et al., 2015), 10) Dongge Cave (Cheng et al., 2016), 11) Sanbao Cave (Cheng et al., 2016), 12) Hulu Cave (Cheng et al., 2016), and 13) Site U1429 (Clemens et al., 2018).

2. Background and Approach

2.1 Site Description

Indian margin Site U1446 (19°5.0'N, 85°44.0'E, 1440mbsl, 70km offshore) (Figure 1) is located near the mouth of the Mahanadi catchment (Clemens et al., 2016). The majority of sediment and terrestrial organic matter at Site U1446 comes from the Mahanadi River Basin (Dunlea et al., 2020) (Figure S1). The Mahanadi River Basin receives ~85% of the annual rainfall during the ISM (June-August) (Figures 1, S2 and Text S2). The age model was constructed by mapping of U1446 benthic foraminifera $\delta^{18}O$ (Text S3) to the LR04 stack (Lisiecki & Raymo, 2005) using Analyseries (Paillard et al., 1996). Correlations and tie points are shown in Figure 2 and Table S1.

2.2 Precipitation Isotope Drivers

Modern interannual precipitation isotopes over India are weakly correlated with the "amount effect": greater precipitation amount leads to lighter precipitation isotopes (Rao et al., 2016). Proximal to Site U1446, GNIP stations (IAEA/WMO, 2019) in Bangladesh indicate that annual weighted precipitation isotopes are weakly correlated with total annual precipitation amount (r^2=0.32) and annual average water vapor pressure (r^2=0.29) but have no relationship with annual average temperature (r^2=0.01) (Figure S3). Hence, the modern precipitation "amount effect" explains about 32% of the total modern variance. Changes in moisture source origin and transport also impact precipitation isotopes (Text S4).

2.3 δD_{wax} Proxy

Long-chain lipid *n*-alkanoic acids are components of waxy coatings on terrestrial plant leaves that are transported by wind and water into the ocean and are preserved in sediments (Sachse et al., 2012). Multiple lines of evidence support interpretation of the hydrogen isotopic composition of these waxy coatings (δD_{wax}) as a proxy for precipitation isotopic composition (δD_{precip}) over the ISM region. Site U1446 collects leaf wax fatty acids predominantly from the proximal Mahanadi River Basin and small coastal catchments (Dunlea et al., 2020), and we infer that δD_{wax} should be representative of Mahanadi basin-integrated δD_{precip}. Catchment studies in the nearby larger Ganges-Brahmaputra catchment finds the exported signal records the basin-integrated δD_{precip} (Galy et al., 2011). Integrating leaf waxes from a large catchment reduces the variability from different vegetation and microclimates, providing clearer climate signals (Douglas et al., 2012). Although residence time could impose a lag in sedimentary systems, even in the much larger floodplain system of the Ganges-Brahmaputra catchment, leaf wax fatty acids have been shown to have short residence times (from 0.015 to 1.2 kyr) (French et al., 2018; Galy & Eglinton, 2011) that do not interfere with the timing of the forcing and response investigated here.

Holocene records support δD_{wax} as an ISM proxy. Two multi-proxy studies in the Bay of Bengal fan interpret Ganges-Brahmaputra basin δD_{wax} as a monsoonal precipitation proxy which exhibits similar variability to monsoonal proxies including speleothem $\delta^{18}O$, salinity, vegetation structure, and runoff records (Contreras-Rosales et al., 2014; Hein et al., 2017). Located within the CMZ, Lonar Lake δD_{wax} record is interpreted to reflect monsoonal precipitation, moisture source, and moisture transport changes, demonstrating similar variability to local speleothem and vegetation records (Sarkar et al., 2015). Thus, we can use δD_{wax} from Site U1446 to reconstruct late Pleistocene ISM circulation variability within the local Mahanadi River Basin in the CMZ.

3. δD_{wax} and δD_{precip} Records

Hydrogen isotopes of C_{28} *n*-acid (δD_{wax}) were analyzed at ~2 kyr resolution in sediments from Site U1446 over the last 640 kyr (Text S5). δD_{wax} is converted to δD_{precip} using ice volume and vegetation corrections (Text S6). δD_{precip} is heavier by about 95‰ with a nominally increased range of 3‰ (Figure 2a). All climatic interpretations are made from the corrected δD_{precip} record. However, the results and interpretation of the δD_{wax} record would be the same regardless of whether or not the corrections are incorporated.

3.1 Spectral Structure

Both the δD_{wax} and δD_{precip} records show heavier values during glacial periods and lighter values during interglacial periods (Figure 2a). Superimposed on the glacial-interglacial pattern are higher frequency variations driven by precession and obliquity. This is clearly reflected in the spectral analysis of the records relative to ETP, a normalize average record of eccentricity, tilt (obliquity) and precession (June 21 perihelion). δD_{wax} spectral structure is dominated by 100 kyr eccentricity, 41 kyr obliquity, 23 kyr and 19 kyr precession cycles (Figure 2b). δD_{precip} has the same peaks, but with relatively increased 19 kyr precession-band variance due to the vegetation and ice volume corrections lowering the spectral power across eccentricity, obliquity, and precession 23 kyr frequencies (Figure 2b).

3.2 Coherence and Phase

Coherence provides a measure of linear correlation among variables as a function of frequency while phase indicates the temporal leads and lags critical to understand forcing and response relationships (Tables S1 and S3). δD_{wax} and δD_{precip} are highly coherent with one another (Tables S3) and in phase at the 100 kyr eccentricity, 41 kyr obliquity, and 23 kyr precession cycles (Table S2). The δD_{wax} and δD_{precip} are highly coherent with orbital parameters (eccentricity, obliquity, and precession) (Table S2) as well as with ice volume and greenhouse gas concentration (Tables S3).

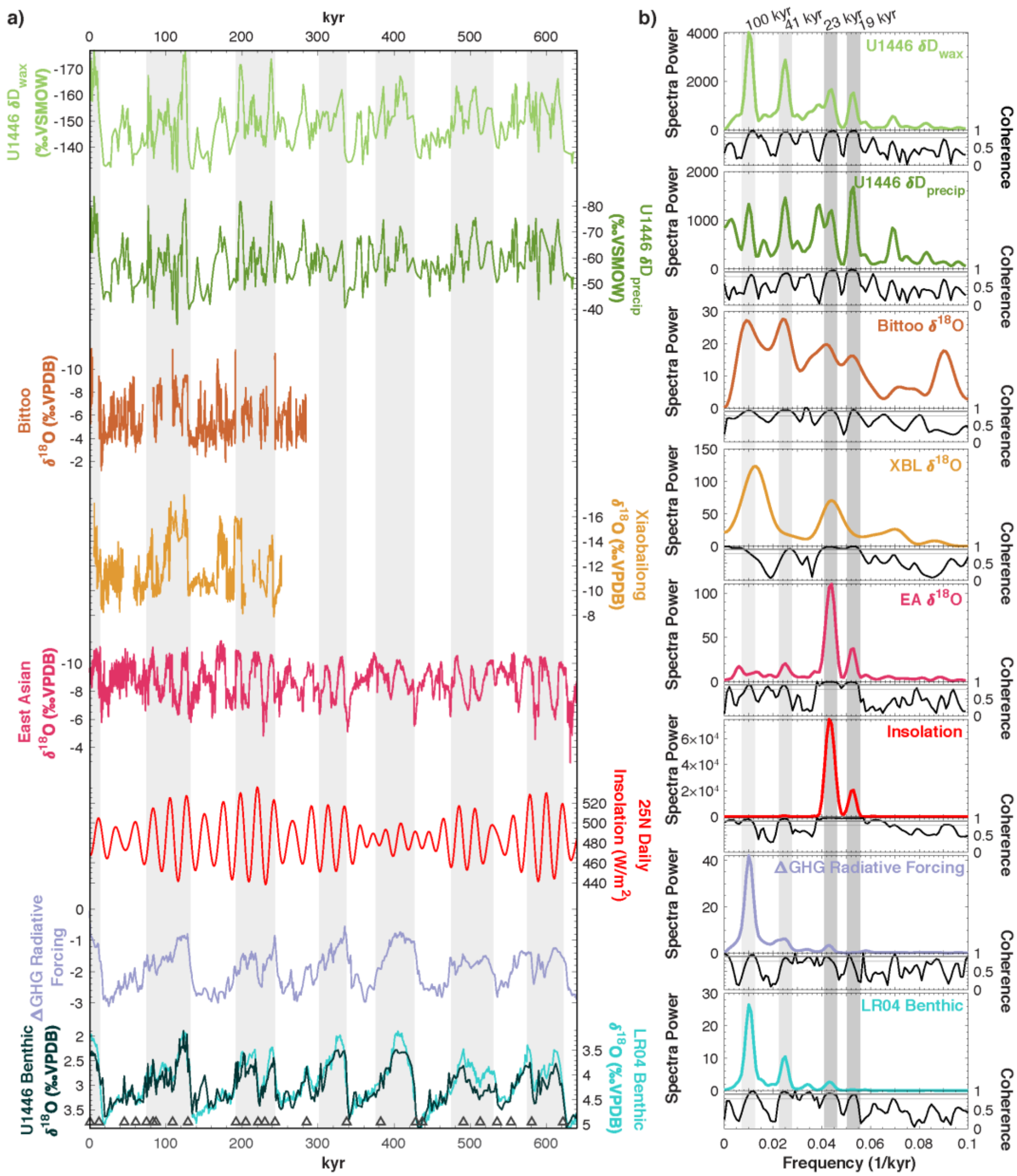

Figure 2.

Timeseries and spectra. From top to bottom: U1446 δD_{wax}, U1446 δD_{precip}, Bittoo speleothem $\delta^{18}O$ (Kathayat et al., 2016), Xiaobailong (XBL) speleothem $\delta^{18}O$ (Cai et al., 2015), East Asian (EA) speleothem $\delta^{18}O$ composite (Cheng et al., 2016), daily insolation for June 21 at 25°N (Laskar et al., 2004), radiative forcing of greenhouse gas (Lo et al., 2017) calculated using CO_2 and CH_4 concentration (Bereiter et al., 2015; Loulergue et al., 2008), and the global benthic stack (Lisiecki & Raymo, 2005). a) Timeseries with light gray bands highlight interglacial periods. At bottom, the U1446 benthic $\delta^{18}O$ stratigraphy overlays the LR04 stack with triangles indicating tie points. b) Proxy spectra and coherence relative to ETP up to 640kyr or maximum record length with a 50% lag calculated on ARAND software (Howell et al., 2006). For coherence, thin and thick gray lines represent 80% and 95% confidence intervals, respectively. Gray bands highlight eccentricity, obliquity, and precession frequencies.

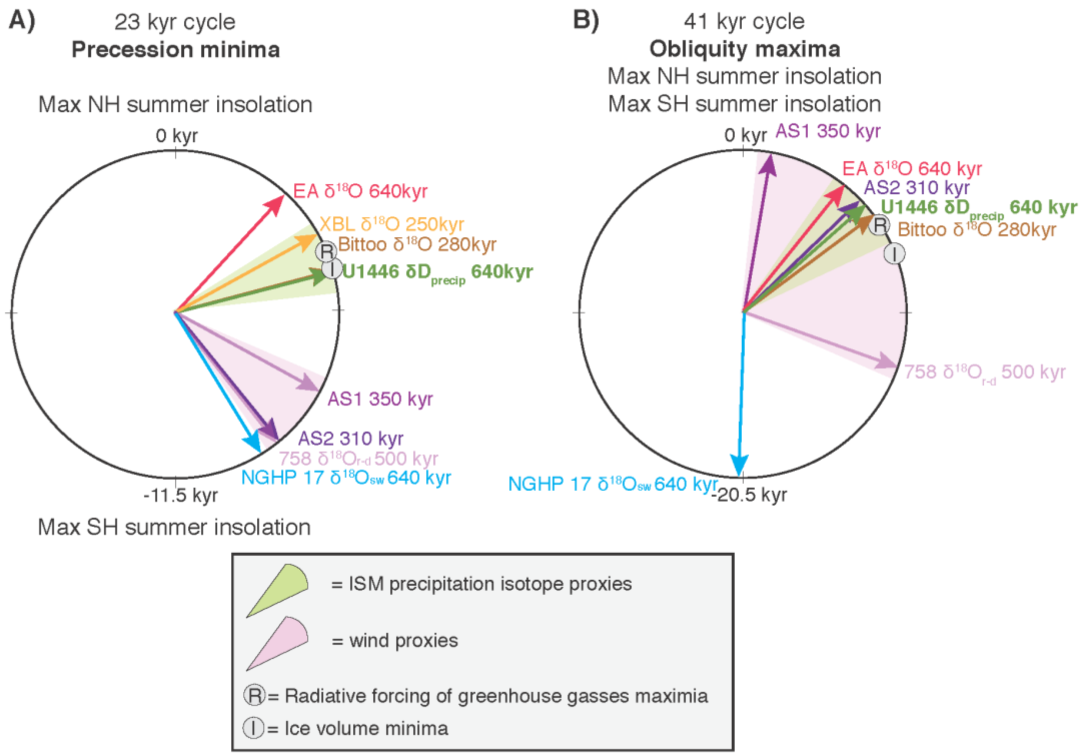

Figure 3.

Phase wheels of a) precession and b) obliquity ISM records. U1446 δDprecip, Bittoo speleothem δ18O (Kathayat et al., 2016), and XBL speleothem δ18O (Cai et al., 2015), compared with East Asian speleothem composite (EA δ18O: Cheng et al., 2016), wind proxies (AS2: Caley et al., 2011; AS1: Clemens & Prell, 2003; 758 δ18Or-d: Bolton et al., 2013), and runoff proxy (NGHP17 δ18Osw: Gebregiorgis et al., 2018). Dots represent greenhouse gasses radiative forcing maxima from CO2 and CH4 (Bereiter et al., 2015; Loulergue et al., 2008) calculated by the method from Lo et al. (2017), and ice volume minima (Lisiecki & Raymo, 2005). Negative/positive phases are measured in the clockwise/anticlockwise direction and represent phase lags/leads relative to precession minima or obliquity maxima. Phase errors are reported in Table S2.

4. Discussion

4.1 Consistent Indian Summer Monsoon Precipitation Isotope Signal

The δD_{precip} spectral structure is similar to Indian monsoon speleothem $\delta^{18}O$ spectral structure. Bittoo speleothem $\delta^{18}O$ has variance at the 100- and 41- kyr spectral bands exceeding that at the precession band (Figure 2b). XBL speleothem $\delta^{18}O$ has 100-kyr variance exceeding that at the precession band as well (Figure 2b). Local insolation is dominated by precession variance while internal climate forcings including ice volume and greenhouse gas radiative forcing are all dominated by eccentricity and obliquity variance. The existence of significant of variance at the 100- and 41-kyr spectral bands indicates the ISM precipitation isotopes are strongly sensitive to internal climate drivers, as opposed to direct insolation forcing. Both the speleothem $\delta^{18}O$ and U1446 δD_{precip} records show large-amplitude changes at terminations, further linking variability in these proxies to climate change boundary conditions driven by ice volume and greenhouse gas.

Beyond spectral structure, coherence and phase analysis offer a means of quantifying relationships among time series. At precession, δD_{precip} lags precession minima by about 4.9 kyrs and obliquity maxima by 5.6 kyrs. At both precession and obliquity, δD_{precip} is coherent and in phase with Bittoo speleothem $\delta^{18}O$ as well (Figure 3, Tables S2 and S3). Finally, at precession, δD_{precip} is coherent and in phase with XBL speleothem $\delta^{18}O$ (Figure 3, Tables S2 and S3). These relationships indicate a consistent ISM precipitation isotope response in records recovered from both terrestrial and marine archives, using two independent (organic and inorganic) proxies. δD_{precip} is consistently in phase with ice volume minimum and greenhouse gas maxima at both precession and obliquity (Figure 3, Table S2). In short, $\delta D_{precip,}$ Bittoo and XBL speleothem $\delta^{18}O$ are all coherent with ice volume and greenhouse gas across the orbital frequencies (Table S3). Since Bittoo and XBL are highly coherent with each other, a Bittoo-XBL composite was created, filling in the gaps in Bittoo with XBL (Figure S4). This composite is also highly coherent with both δD_{precip} and the internal climate parameters (Table S3). This multi-proxy ISM precipitation isotope response is maximized (lightest values) at times of maximum greenhouse gas radiative forcing and minimum high-latitude ice-volume indicating a common, strong response to internal climate forcings. Below we place these findings in context with other proxies and provide our climatic interpretation.

4.2 Indian Summer Monsoon Proxy Comparison

Beyond the ISM precipitation isotope proxies discussed above, a range of summer monsoon wind and seawater $\delta^{18}O$ records from the Arabian Sea and Bay of Bengal also have significant spectral structure outside of precession, further documenting ISM sensitivity to ice volume and greenhouse gas forcing. However, these wind and seawater $\delta^{18}O$ proxies significantly lag the three terrestrial precipitation isotope records at precession. At obliquity the wind proxies are widely distributed (Figure 3).

Andaman Sea site NGHP 17 seawater $\delta^{18}O$ is interpreted as a salinity indicator, responding to eastern Bay of Bengal rainfall and runoff from the Salween and Irrawaddy catchments to the north (Gebregiorgis et al., 2018). NGHP 17 seawater $\delta^{18}O$ lags δDprecip by about 4 kyrs at precession and about 6 kyrs at obliquity (Figures 1, 3). These phase differences indicate that terrestrial precipitation isotope and seawater isotope records capture different aspects of the monsoon system. Runoff proxies in the Andaman Sea may be delayed in phase relative to North Indian precipitation isotopes due to differences in rainfall on the eastern and western sides of the Bay of Bengal.

Additionally, ISM precipitation isotopes are sensitive to moisture source and moisture transport isotopic effects that may not be reflected in Andaman seawater isotopes.

Wind proxies from the Arabian Sea at sites RC27-61, 722B, and MD04-2861 (Clemens & Prell, 2003, Caley et al., 2011) as well as from eastern equatorial Indian site 758 (Bolton et al., 2013) also lag δD_{precip} at the precession band, by about 4 kyrs (Figures 1, 3). The uniform wind response at precession indicates Arabian Sea and Bay of Bengal winds both strengthen closer to precession maxima than precession minima. At the obliquity band, the Arabian Sea wind records slightly lead or are in phase with the δDprecip suggesting potential links to moisture transport. The equatorial eastern Indian Ocean wind record significantly lags, indicating wind strength in the Arabian Sea and Bay of Bengal are uncoupled at obliquity. We look to simulations to help interpret these phase relationships.

4.3 Model Comparison

U1446 δD_{precip} shows strong glacial-interglacial variability with heavier isotopic signatures during glacials and lighter signatures during interglacials, consistent with isotope-enabled simulations for the ISM region (Cai et al., 2015). If the modern precipitation isotope and rainfall amount regression (Figure S3) is extrapolated back in time, then interglacials were ~30% wetter and glacials ~40% drier compared to modern. A 40% reduction of ISM rainfall during glacial periods aligns with model results indicating precipitation reduction over India between 10% and 50% compared to modern (Chabangborn et al., 2014; Dinezio & Tierney, 2013).

Idealized climate models driven only by insolation show increased ISM precipitation at times of increased summer insolation (minimum precession and maximum obliquity), accompanied by a redistribution of precipitation and convection from ocean to land (Bosmans et al., 2018). Similarly, idealized insolation only isotope-enabled models show that changes in moisture sources and transport paths also impact precipitation isotopes on orbital timescales (Hu et al., 2019; Tabor et al., 2018), indicating lighter precipitation isotopes in India during high insolation and heavier precipitation isotopes during low insolation (Battisti et al., 2014; Hu et al., 2019; Tabor et al., 2018). However, these models are limited to the equilibrium monsoon responses to orbital forcing only and cannot address phase lags attributed to atmospheric CO2 and ice volume. These models, as well as time-dependent models that include changes in insolation, ice volume, and greenhouse gas concentration (Caley et al., 2014), all underestimate the isotopic range in both leaf wax δDprecip and speleothem δ18Oprecip records over India; models indicate about 8‰ change in δDprecip (Battisti et al., 2014; Tabor et al., 2018) whereas proxy data indicate about 20‰ change in δD_{precip} at the precession-band time scale.

The δDprecip phase relative to runoff proxies suggests that δDprecip is capturing more than just precipitation amount but also moisture source and transport variability. Orbital-scale modeling indicates that moisture source varies as a function of monsoonal circulation, with stronger large-scale circulation leading to lighter precipitation isotopes; due to sourcing from distal regions and longer transport paths (Tabor et al., 2018). At the precession band, two moisture routes are present, feeding into the CMZ of India: a longer path during precession minima and a shorter path during precession maxima (Figure 4). During precession minima, enhanced distal moisture sourcing leads to lighter precipitation isotopes (Tabor et al., 2018) which is supported by a narrow, concentrated low-level jet during precession minima (Jalihal et al., 2019) (Figure 4a). During precession maxima, enhanced proximal moisture sourcing leads to shorter transport distances and heavier precipitation isotopes (Tabor et al., 2018) which is supported by a wider, dispersed low-level jet with stronger Bay of Bengal winds, possibly leading to enhanced (proximal) Bay of Bengal moisture sourcing (Jalihal et al., 2019) (Figure 4b). A similar monsoon circulation pattern is also seen at glacial-interglacial scales with longer moisture transport paths during interglacials, leading to lighter precipitation isotopic values, and shorter moisture transport paths during glacials, leading to heavier precipitation isotopic values (Cai et al., 2015). These models support the interpretation of ISM precipitation isotopes as capturing these large-scale moisture circulation changes.

Additionally, models show there is a difference in the timing of maximum terrestrial versus marine rainfall for the ISM. Increased precipitation over the CMZ at precession minima and increased precipitation over the Bay of Bengal during precession maxima is observed in multiple climate models forced only by insolation (Jalihal et al., 2019; Lee et al., 2019; Tabor et al., 2018). Jalihal et al. (2019) interpret the out of phase precipitation over the CMZ and Bay of Bengal as a function of low-level jet dynamics driven by insolation influence on terrestrial precipitation and surface fluxes and driven by vertical stability influence on precipitation over the ocean. This opposite precession precipitation variability over the India CMZ and Bay of Bengal is reflected in the ~90° phase difference between the Indian δDprecip and Andaman Sea seawater $\delta^{18}O$, consistent with the two proxies capturing different components of the monsoon system.

In summary, monsoon proxies are broadly consistent with insolation only model results (which can only yield precipitation and precipitation isotope responses that are in phase with orbital maxima or minima); the proxy δD_{precip} phase falls closer to precession minima while Andaman $\delta^{18}O_{seawater}$ phase falls closer to precession maxima. Neither of the proxy records indicate phase responses aligned with orbital extremes, rather, the phases are drawn away from these orbital positions because of their sensitivity to coupled ice volume and greenhouse gas forcing.

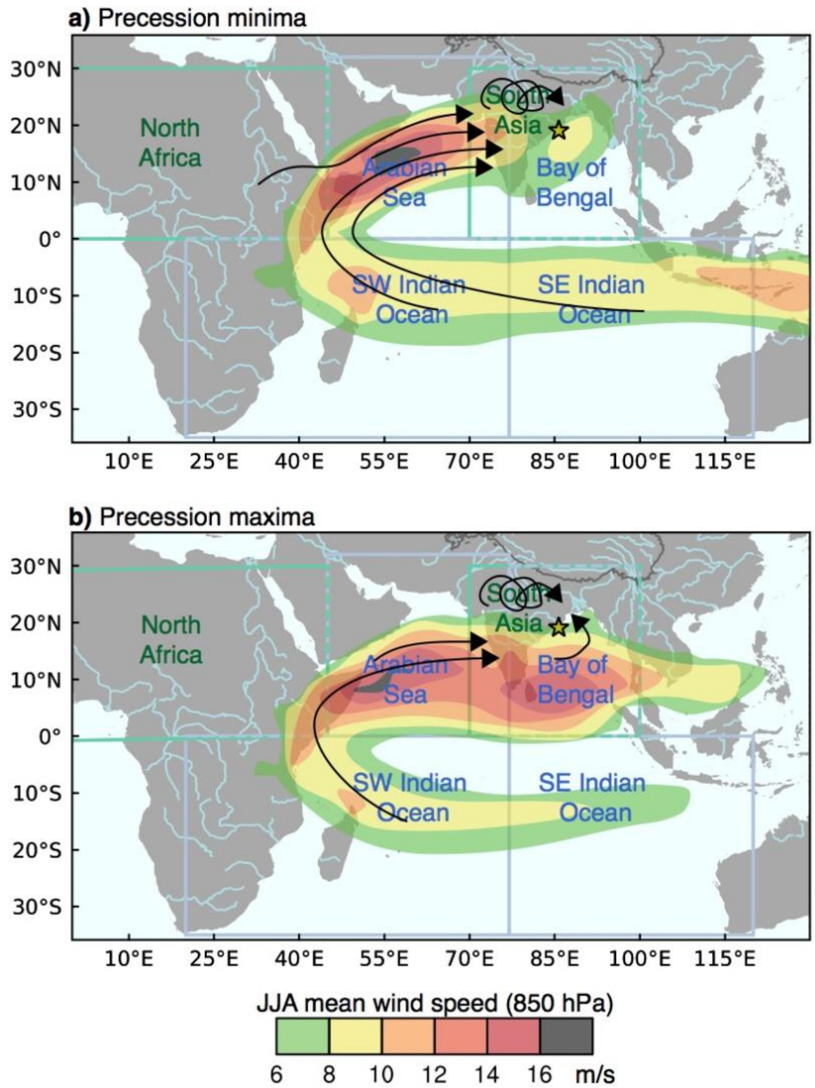

Figure 4

Schematic of precession-band ISM moisture transport. The arrows represent moisture sources from Tabor et al. (2018) and follow the simulated wind field response from Jalihal et al. (2019). The spiral arrow over South Asia represents recycled water from the ISM region. The shading shows June-August mean wind speed (850 hPa) of greater than 6 m/s (after Jalihal et al., 2019). a) At precession minima, maximum summer wind strength is concentrated in a narrow low-level jet (Jalihal et al., 2019) supporting more distal moisture sources and longer transport paths (Tabor et al., 2018). b) At precession maxima, maximum summer wind strength is dispersed in a broader low-level jet (Jalihal et al., 2019) supporting more proximal moisture sources and shorter transport paths (Tabor et al., 2018).

4.4 Interpretation of Indian vs East Asian Summer Monsoon Records

East Asian speleothem $\delta^{18}O$ records have been used to infer Asian monsoon intensity, grouping together the Indian (South Asian) summer monsoon with the East Asian summer monsoon (e.g., Cheng et al., 2016). East Asian speleothem $\delta^{18}O$ from the Yangtze River valley (YRV) exhibits a dominant precession-band response (Figure 2b) and thus insolation is interpreted as the primary driver of Asian monsoon intensity. This is in contrast to the East China Sea seawater $\delta^{18}O$ record that monitors YRV runoff; having removed the temperature and global ice-volume signals, YRV runoff has little to no precession-band variance (Clemens et al., 2018). As well, isotope enabled climate models suggest that East Asian speleothem $\delta^{18}O$ does not reflect local precipitation amount at the orbital timescale (Battisti et al., 2014; Caley et al., 2014; Hu et al., 2019). Instead, orbital scale East Asian speleothem $\delta^{18}O$ variation is thought to represent large scale dynamics along moisture transport paths (Battisti et al., 2014; Caley et al., 2014; Hu et al., 2019; Zhang et al., 2020)

The spectral structures of U1446 δD_{precip}, Bittoo $\delta^{18}O$, and XBL $\delta^{18}O$ records have significant spectral structure outside of precession, unlike the East Asian speleothem $\delta^{18}O$ (Figure 2b). As well, both Bittoo $\delta^{18}O$ and δD_{precip} slightly lag East Asian speleothem $\delta^{18}O$ at precession and obliquity and are in phase with CO_2 maxima and ice volume minima (Figure 3). The spectral structure and phase of U1446 δD_{precip}, Bittoo, and XBL precipitation $\delta^{18}O$ clearly indicate sensitivity to greenhouse gas radiative forcing and ice volume, a finding very different from that based on the East Asian speleothem $\delta^{18}O$ record. On the basis of the difference in spectral structure, coherence, and phase relationships demonstrated here, the precipitation isotope responses of the Indian and

East Asian subsystems are uncoupled, responding in different ways to internal and external driving mechanisms at orbital time scales.

5. Conclusions

The ISM δD_{precip} and speleothem $\delta^{18}O$ signals exhibit strong spectral structure outside of precession, show strong glacial-interglacial changes, and are coherent and in phase with greenhouse gas maxima and ice volume minima. This indicates large-scale ISM circulation encompassing precipitation, moisture source, and moisture transport changes are dominated by these internal climate drivers. Proxy phase responses are broadly consistent with insolation-only model experiments showing increased precipitation, more distal moisture sources and longer transport paths leading to lighter isotopes at precession minima and interglacials (Bosmans et al., 2018; Cai et al., 2015; Jalihal et al., 2019; Tabor et al., 2018). On the basis of our results indicating strong sensitivity to CO_2 maxima and ice volume minima, future anthropogenic increases in greenhouse gas radiative forcing may change large-scale ISM circulation leading to increased precipitation and more distal moisture sources.

Acknowledgments, Samples, and Data

This research used samples provided by the Integrated Ocean Drilling Program (IODP). This research was supported by NSF Grant #1634774 to S. Clemens and Y. Huang and JSPS grant JPMXS05R2900001 to M. Yamamoto. We are grateful for the lab support provided by Marcelo Alexandre, Ewerton Santos, and Yuko Tsuchiya. We thank the science and ship crew of IODP Exp 353. The U1446 δD_{wax}, δD_{precip}, $\delta^{13}C_{wax}$, and benthic $\delta^{18}O$ data presented in this paper are archived at NOAA's National Centers for Environmental Information (https://www.ncdc.noaa.gov/paleo/study/32374). Supporting

paleoclimate datasets are available in these in-text data citation references: Bittoo speleothem $\delta^{18}O$ (Kathayat et al., 2016), Xiaobailong speleothem $\delta^{18}O$ (Cai et al., 2015), East Asian speleothem $\delta^{18}O$ composite (Cheng et al., 2016), wind proxies (AS2: Caley et al., 2011; AS1: Clemens & Prell, 2003; 758 $\delta^{18}O_{r\text{-}d}$: Bolton et al., 2013), runoff proxy (NGHP17 $\delta^{18}O_{sw}$: Gebregiorgis et al., 2018), daily insolation for June 21 at 25°N (Laskar et al., 2004), radiative forcing of greenhouse gas (Lo et al., 2017) calculated using CO_2 and CH_4 concentration (Bereiter et al., 2015; Loulergue et al., 2008), and the global benthic stack (Lisiecki & Raymo, 2005). The authors declare no conflicts of interest.

Supporting Information

Text S1. Utility of the Leaf Wax Hydrogen Isotope Proxy for the Indian Summer Monsoon

Precipitation isotopes reflects the isotopic composition of rainfall which, in turn reflects a number of critical aspects of monsoonal hydroclimate including moisture source area, evaporation and condensation along the transport path, and local rainfall amount (Ansari et al., 2020; Breitenbach et al., 2010; Rao et al., 2016). Additionally, precipitation isotopes are now being added into climate models and allow direct proxy-model comparisons (e.g., Tabor et al., 2018). Leaf wax hydrogen isotopes (δD_{wax}) offer a complementary, independent means of assessing continental precipitation isotopes, relative to that based on speleothem $\delta^{18}O$. While speleothem $\delta^{18}O$ can be readily and accurately dated, records are limited to regions with karst lithologies and can be influenced by factors influencing groundwater transport through the soil and subsurface karst environments. δD_{wax} reflects the δD of the plant source waters and is offset by soil evaporation, biosynthesis, and plant transpiration processes (Sachse et al., 2012). Plant type can influence the apparent D/H fractionation between meteoric water and wax; thus, we use paired carbon isotope of leaf waxes to correct for potential influences of changes in C3 and C4 plant abundances on reconstructed precipitation isotopes (Sachse et al., 2012; Dunlea et al., 2020) (Text S6). Leaf waxes are abundant in a wide variety of sedimentary settings, well-preserved for long periods of time, and can yield long, continuous records, exceeding in length those from radiometrically dated cave deposits.

In addition, leaf waxes preserved in marine sediments allow continental-marine multi-proxy comparisons that are built off the same chronology.

Text S2. Mahanadi River Basin Climatology

The Mahanadi River Basin is within the area of the Indian core monsoon zone that receives the most summer rainfall (Figure 1). Precipitation averages ~250mm per month during the summer monsoon (S1). Temperature changes seasonally, peaking in May before the monsoon season begins. The monthly average temperature ranges from 22°C in the winter to 32°C in the summer. During the monsoon season, the average temperature is ~28°C.

The modern Mahanadi Basin consists of both agriculturally developed and natural landscapes. The natural flora is made up of closed-canopy, moist tropical deciduous forests, and woodlands with some savannas (Giosan et al., 2017; Roy et al., 2015). In past colder and dry periods since the last glacial maximum, C4 tropical grasses and savanna expanded, indicating the basin vegetation is sensitive to climate changes (Zorzi et al., 2015).

Text S3. Benthic Foraminifera $\delta^{18}O$ Analyses

Individual *Uvigerina spp* and *Cibicidoides wuellerstorfi* (depending on availability) were picked from the 250–355 μm and >355 μm (when necessary) fractions. Samples were analyzed on a MAT252 IRMS coupled to a Kiel III carbonate device; reacted by individual acid addition (99% H3PO4 at 70 °C). Repeated analyses of Brown Yule Marble (n = 72, 1σ) yields −6.40 ± 0.08 for δ18O. Carrara Marble (n = 108, 1σ) yield −1.85 ± 0.05 for δ18O. Replicate analysis of foraminifera samples (n = 42, 1σ) yields a median half range of 0.03 for δ18O. Isotopic offsets between C. wuellerstorfi and Uvigerina spp were accounted for by subtracting 0.61 Uvigerina spp values for $\delta^{18}O$, based median offsets of paired samples (n=452). All results were calibrated to National Institute of Standards and Technology (Gaithersburg, Maryland) carbonate isotope standard NBS19 and are reported as ‰ VPDB.

Text S4. Modern Moisture Sources

The modern Indian Summer Monsoon moisture supply is dominated by oceanic sources. During the first of them half of the monsoon, the western Indian Ocean supplies the most moisture to the core monsoon zone. During the end of the monsoon season in August and September, continental moisture sources increase with the increase of soil water availability and evapotranspiration in the Ganges Basin (Pathak et al., 2017). Strong monsoon years are associated with enhanced Indian Ocean moisture transport. Weak monsoon years are associated with lower contribution from oceanic sources and are sustained by the evapotranspiration from land surface processes (Pathak et al., 2017). Thus, the strength of the meridional moisture flux over the Indian Ocean is a key factor in Indian Summer Monsoon variability.

On synoptic scales, moisture supply from the Bay of Bengal feeds monsoonal low-pressure systems. Monsoonal low-pressure systems occur on average 14 times per monsoon season with half forming stronger Indian monsoon depressions (Hurley & Boos, 2015). These low-pressure systems bring moisture from the Bay of Bengal into the core monsoon zone (Hurley & Boos, 2015) and account for 45% to 55% of the modern total Indian rainfall (Yoon & Chen, 2005).

Changes in moisture source origin and transport also impact precipitation isotopes. In the modern, the Bay of Bengal is fresher than the Arabian Sea, which is reflected in the seawater isotopes: the average Bay of Bengal $\delta^{18}O_{seawater}$ is about -0.5‰ and Arabian Sea $\delta^{18}O_{seawater}$ is about 0.6‰ (Kumar et al., 2010). Longer transport paths enable more fractionation of the precipitation isotopes, leading to lighter isotopic values. Sub-seasonal studies of precipitation isotopes in northeast and eastern India show weak amount effects and show moisture source origin and transport strongly influence the precipitation isotopes (Ansari et al., 2020; Breitenbach et al., 2010). Thus, source location and transport path of the moisture supply influences precipitation isotopes in the modern Indian Summer Monsoon region.

Text S5. Leaf Wax Analyses

Lipids are extracted from 3 to 8g of dry sediment with an Accelerated Solvent Extractor 200 (Dionex). The extracts are dried under N_2 and separated on aminopropyl silica gel flash columns, eluting neutral fractions with dichloromethane (DCM): isopropanol 2:1 (v:v) and acid fractions with 4% acetic acid in diethyl ether. All flash column separations use three column volumes of each eluent. Acid fractions are methylated in anhydrous 5% HCl in methanol at 60°C overnight. Samples are further cleaned using silica gel flash columns: polar compounds are removed with hexane, fatty acid methyl esters (FAMEs, our target compounds) are eluted with DCM. The δD of the C_{28} n-alkanoic acid are measured using Gas Chromatography-Pyrolysis Isotope Ratio Mass Spectrometry at Brown University. Samples are run in triplicate. The pooled standard deviation of triplicate samples is 1.6‰, and the standard deviation of a standard run every 3 injections is 2.5‰. The $\delta^{13}C$ of the C_{28} n-alkanoic acid are measured using an Agilent 6890 series gas chromatograph combined with a Finnigan MAT delta Plus mass spectrometer at Hokkaido University. The reproducibility of the $\delta^{13}C$ measurement based on repeated analyses was better than ± 0.1 ‰. Samples have been corrected for the methyl group added during fatty acid derivatization using the known isotopic composition of the acidified methanol used in methylation.

Text S6: Ice Volume and Vegetation Corrections

δD_{wax} are corrected for both ice volume and vegetation effects. The effect of global ice volume on the ocean isotopic reservoir is corrected by assuming a 1‰ ^{18}O-enrichment in the LGM oceans (Schrag et al., 1996) scaled to changes in global ice volume recorded by the U1446 benthic foraminifera. On average the ice volume correction decreases the δD_{wax} value by 5 ± 3 ‰. The average ice correction applied to $\delta D_{wax\ during}$ glacial periods is -7 ± 2‰ and the average ice correction applied to $\delta D_{wax\ during}$ interglacial periods is -3 ± 2 ‰:

Equation 1: $$\boldsymbol{\delta D_{wax-ice} = \delta D_{wax} - [(\delta^{18}O_{benthic} - coretop\ \delta^{18}O_{benthic}) \times \varepsilon_{ice} \times \frac{8\text{‰}\ \delta D}{1\text{‰}\ \delta^{18}O}]}$$

where: coretop $\delta^{18}O_{benthic}$ = 2.36‰ and ε_{ice} = 1‰ ^{18}O-enrichment.

The resulting ice-volume-corrected δD values were then corrected for variable hydrogen isotope fractionation by each C3 and C4 vegetation endmembers to estimate precipitation δD values (δD_{precip}) by using paired $\delta^{13}C_{wax}$ measurements and methods outlined in Konecky et al. (2016) and C28*n*-acid endmember $\delta^{13}C$ values of -36.9‰ and -19.5‰ for C3 and C4 plants, respectively. The vegetation correction holds significant uncertainty (+/- 34‰). On average the vegetation correction increases the $\delta D_{wax\ value}$ by 96‰. The average correction applied to $\delta D_{wax\ during}$ glacial periods is 96‰ and average correction applied to δD_{wax} during interglacial periods is 95‰:

Equation 2: $\%\mathbf{C_4} = \frac{\boldsymbol{\delta^{13}C_{wax} - \delta^{13}C_{C3}}}{\boldsymbol{\delta^{13}C_{C4} - \delta^{13}C_{C3}}}$

Equation 3: $\%\mathbf{C_3} = \mathbf{100} - \%\mathbf{C_4}$

where: $\delta^{13}C_{C3} = -19.5‰$ and $\delta^{13}C_{C4} = -36.9‰$

Equation 4: $\boldsymbol{\varepsilon}_{\mathbf{wax-Pveg}} = \left(\%\mathbf{C_3} * \boldsymbol{\varepsilon}_{\mathbf{C27.alk-P_{C3}}}\right) + \left(\%\mathbf{C_4} * \boldsymbol{\varepsilon}_{\mathbf{C27.alk-P_{C4}}}\right) + \boldsymbol{\varepsilon}_{\mathbf{alkane-acid}}$

where: $\varepsilon_{C27.alk-P_{C3}} = 128.9 \pm 29.8‰$,

$\varepsilon_{C27.alk-P_{C4}} = -125.4 \pm 34.0‰$, and $\varepsilon_{alkane-acid} = 25‰$.

Equation 5: $\boldsymbol{\delta}\mathbf{D_{precip}} = \frac{\boldsymbol{\delta}\mathbf{D_{wax-ice}+1000}}{\boldsymbol{\varepsilon}_{\mathbf{wax-Pveg}}\mathbf{/1000+1}} - \mathbf{1000}$

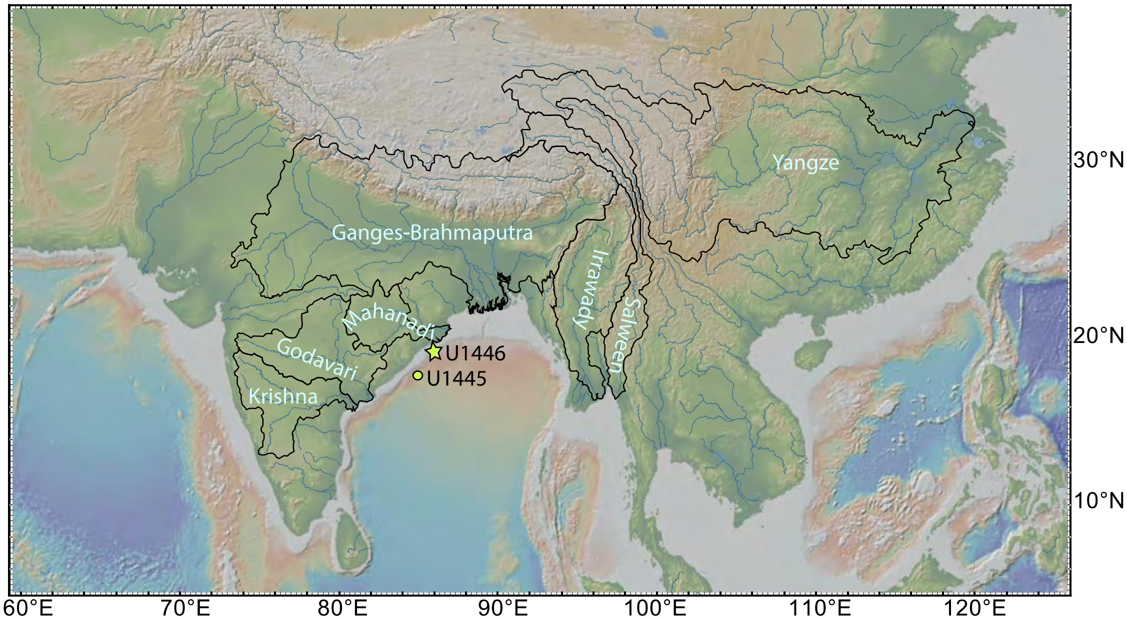

Figure S 1.

Selected major river basin map. Site U1445 is composed of Mahanadi River basin sediment (Dunlea et al., in press). Site U1446 is indicated by the star and is positioned at the mouth of the Mahanadi River basin. Map made using GEOMAPAPP (http://www.geomapapp.org, Ryan et al., 2009).

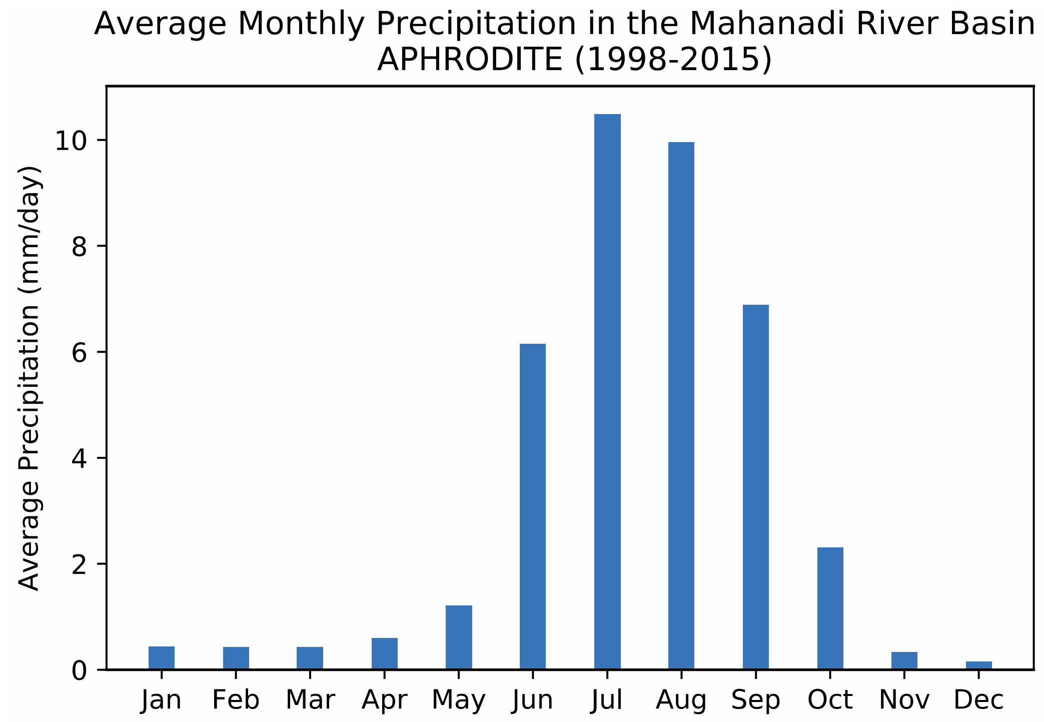

Figure S 2.

Average monthly precipitation over 1998-2015 for Mahanadi River basin from APHRODITE V1901 dataset (Yatagai et al., 2012). Mahanadi River basin ranges from 80°28′E to 86°43′E and 19°8′N to 23°32′N. On average about 85% of annual rainfall occurs during the summer monsoon season from June to September.

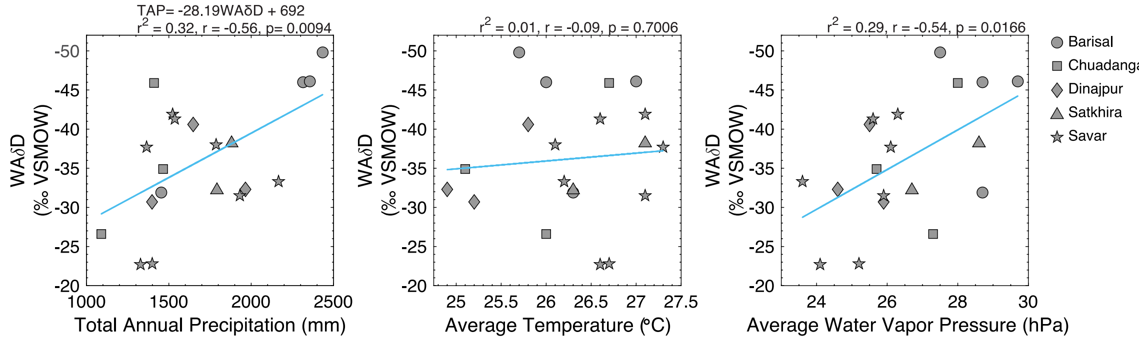

Figure S 3.

Average annual precipitation isotopes from 5 GNIP station sites (Savar, Barisal, Chuadanga, Dinajpur, and Satkhira) in Bangladesh over 2009-2016 (n=20) (IAEA/WMO, 2019). From left to right: Weighted annual average precipitation δD verses total annual precipitation, average annual temperature, and average annual water vapor pressure. Weighted average precipitation isotopes show an interannual amount effect and water vapor pressure effect but no relationship with interannual temperature. About 30% of the modern precipitation isotope variance is explained by water vapor pressure, with lighter isotopes occurring during higher water vapor pressures and increased rainfall during the monsoon season. These are closest GNIP sites to the core summer monsoon zone in India with sufficient annually resolved data.

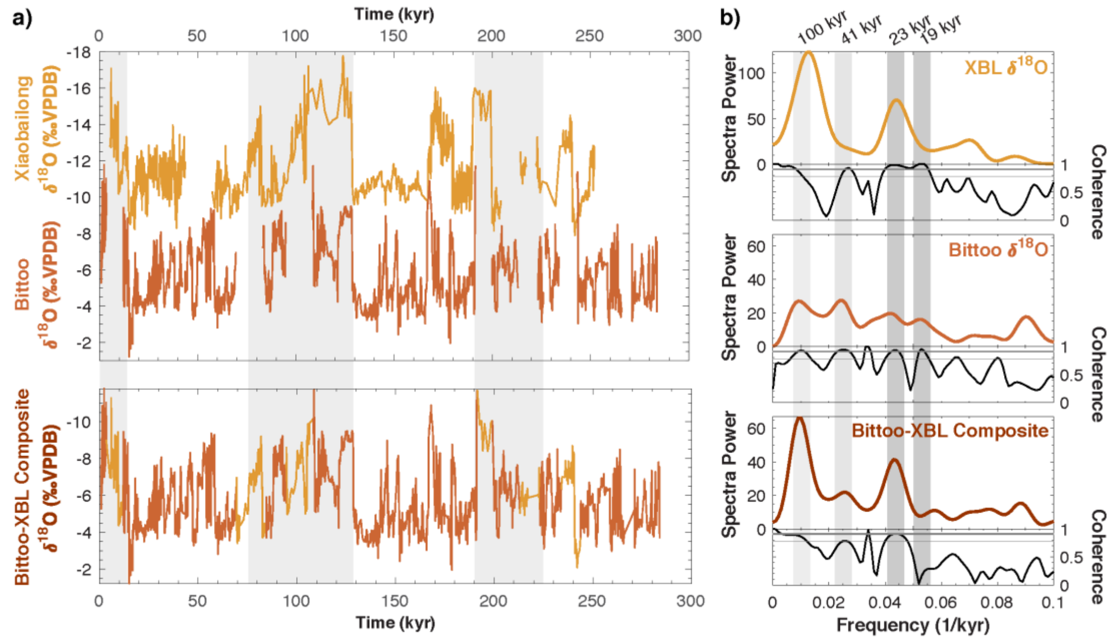

Figure S 4.

Timeseries and spectra of Bittoo-XBL composite. a) On top: the discontinuous timeseries of Bittoo and XBL speleothem δ18O. The offset of the two records is likely due longer moisture transport path to XBL. On bottom, the timeseries of Bittoo-XBL composite. Similar to East Asian composite speleothem methods, Bittoo-XBL composite was made by adding 5.81‰ (difference between the averages of the two records) to XBL and splicing in XBL where Bittoo had missing data. Light gray shading highlights interglacial periods. b) Power spectra and coherence of records compared to ETP. Spectra and coherence calculated using ARAND software (Howell et al., 2006) with 50% lags, on timesteps of 0.05 for Bittoo and 0.1kyr for XBL and Bittoo-XBL composite. Gray bands highlight eccentricity, obliquity, and precession bands. For coherence, thin and thick gray lines represent 80% and 95% confidence intervals, respectively.

Table S 1.

Depth-Age tie points. The Toba ash datum is at 15.64 CCSFD.

U1446 CCSFD (m)	Time (kyr)	Accumulation Rate (m/kyr)
0.05	0.32	0.518
6.11	12.03	0.144
10.91	45.40	0.204
13.95	60.33	0.119
15.64	74.49	0.477
19.72	83.05	0.266
20.73	86.85	0.292
27.15	108.81	0.257
32.33	128.96	0.109
39.23	192.09	0.359
43.83	204.89	0.316
48.97	221.18	0.218
50.90	230.02	0.239
54.09	243.37	0.134
59.65	284.94	0.145
67.27	337.51	0.138
73.43	382.27	0.171
81.30	428.24	0.090
82.07	436.77	0.135
89.39	490.93	0.189
93.57	513.00	0.130
96.45	535.18	0.112
98.50	553.43	0.164
102.95	580.61	0.158
109.46	621.71	0.096
113.35	662.21	0.171

Table S 2.

Proxy coherence and phase relationships relative to orbital parameters.

	Eccentricity (~100 kyr)		Obliquity (~41 kyr)		Precession (~23 kyr)	
Record	Coherence	Phase (°)	Coherence	Phase (°)	Coherence	Phase (°)
U1446 δD_{wax}	0.88	-8.6 ± 16.6	0.92	-57.7 ± 13.2	0.94	-78.4 ± 11.1
U1446 δD_{precip}	0.77	-17.5 ± 24.5	0.85	-50.2 ± 19.3	0.92	-76.5 ± 13.4
GHG RF	0.89	17.0 ± 15.7	0.81	-60.1 ± 21.6	0.86	-70.4 ± 17.7
Ice volume	0.91	-0.63 ± 13.6	0.97	-61.6 ± 7.8	0.93	-73.9 ± 12.3
Bittoo $\delta^{18}O$	0.93	-4.97 ± 12.2	0.94	-54.3 ± 11.61	0.93	-76.3 ± 12.2
XBL $\delta^{18}O$	0.81	-1.1 ± 21.1	0.75	-115.3 ± 25.9	0.99	-60.3 ± 4.8

Note. All coherence and phase calculated over the 0 to 640 ka intervals except for Bittoo (0-284 ka) and XBL (0-252 ka).

U1446 δD_{wax}, U1446 δD_{precip}, LR04 (ice volume), Bittoo $\delta^{18}O$, XBL $\delta^{18}O$ are multiplied by -1 such that the phase of isotopic proxies reflects lighter isotopic values; calculated using ARAND software (Howell et al., 2006) with 50% lags, on timesteps from 0.05 to 2kyr.

0.55 is the confidence interval for coherency.

Values above 0.78 pass statistical test for non-zero coherency at 80% level.

Values above 0.91 pass statistical test for non-zero coherency at 95% level.

All are within phase error of U1446 δD_{precip} (excluding XBL $\delta^{18}O$ at obliquity).

Table S 3.

Coherence among proxy records. A Bittoo-XBL composite is used for cave coherence comparison to aid in filling the discontinuities.

		U1446 δD_{wax}	U1446 δD_{precip}	GHG RF	Ice volume	Bittoo $\delta^{18}O$	XBL $\delta^{18}O$	Bittoo XBL Composite
Eccentricity	U1446 δD_{wax}	1	0.96	0.95	0.98	0.95	0.78	0.96
	U1446 δD_{precip}		1	0.87	0.91	0.84	0.73	0.87
	GHG RF			1	0.99	*	0.69	0.93
	Ice volume				1	*	0.72	0.95
	Bittoo $\delta^{18}O$					1	0.94	1
	XBL $\delta^{18}O$						1	0.92
Obliquity	U1446 δD_{wax}	1	0.97	0.89	0.93	0.86	0.79	0.82
	U1446 δD_{precip}		1	0.85	0.83	0.86	0.73	0.76
	GHG RF			1	0.84	0.85	0.86	0.93
	Ice volume				1	0.92	0.89	0.9
	Bittoo $\delta^{18}O$					1	0.99	0.82
	XBL $\delta^{18}O$						1	0.76
Precession	U1446 δD_{wax}	1	0.99	0.79	0.94	*	0.91	0.95
	U1446 δD_{precip}		1	0.69	0.87	*	0.85	0.91
	GHG RF			1	0.95	0.8	0.87	0.82
	Ice volume				1	0.95	0.92	0.93
	Bittoo $\delta^{18}O$					1	0.96	1
	XBL $\delta^{18}O$						1	0.99

Note. All coherence values calculated over the 0 to 640 ka intervals except for Bittoo (0-284 kyr), XBL (0-252 kyr), Bittoo-XBL composite (0-284 kyr).
U1446 δD_{wax}, U1446 δD_{precip}, LR04 (ice volume), Bittoo $\delta^{18}O$, XBL $\delta^{18}O$ are multiplied by -1 such that the phase of isotopic proxies reflects lighter isotopic values, calculated using ARAND software (Howell et al., 2006) with 50% lags, on timesteps of 2kyr.
0.5523 is the confidence interval for coherency.
Values above 0.784 pass statistical test for non-zero coherency at 80% level.
Values above 0.911 pass statistical test for non-zero coherency at 95% level.
* Unable to assess due to the discontinuities at 2 kyr timestep resolution.

References

Ansari, M. A., Noble, J., Deodhar, A., & Saravana Kumar, U. (2020). Atmospheric factors controlling the stable isotopes ($\delta^{18}O$ and $\delta^{2}H$) of the Indian summer monsoon precipitation in a drying region of Eastern India. *Journal of Hydrology*, 584, 124636. https://doi.org/10.1016/j.jhydrol.2020.124636

Asharaf, S., & Ahrens, B. (2015). Indian summer monsoon rainfall processes in climate change scenarios. *Journal of Climate*, 28(13), 5414–5429. https://doi.org/10.1175/JCLI-D-14-00233.1

Battisti, D. S., Ding, Q., & Roe, G. H. (2014). Coherent pan-Asian climatic and isotopic response to orbital forcing of tropical insolation. *Journal of Geophysical Research: Atmosp*heres, 119(21), 11,997-12,020. https://doi.org/10.1002/2014JD021960

Bereiter, B., Eggleston, S., Schmitt, J., Nehrbass-Ahles, C., Stocker, T. F., Fischer, H., et al. (2015). Revision of the EPICA Dome C CO_2 record from 800 to 600 kyr before present. *Geophysical Research Letters*, 42(2), 542–549. https://doi.org/10.1002/2014GL061957

Berger, A. L. (1978). Long-Term Variations of Caloric Insolation Resulting from the Earth's Orbital Elements. *Quaternary Research*, 9(02), 139–167. https://doi.org/10.1016/0033-5894(78)90064-9

Bolton, C. T., Chang, L., Clemens, S. C., Kodama, K., Ikehara, M., Medina-Elizalde, M., et al. (2013). A 500,000 year record of Indian summer monsoon dynamics recorded by eastern equatorial Indian Ocean upper water-column structure. *Quaternary Science Reviews*, 77, 167–180. https://doi.org/10.1016/j.quascirev.2013.07.031

Bosmans, J. H. C., Erb, M. P., Dolan, A. M., Drijfhout, S. S., Tuenter, E., Hilgen, F. J., et al. (2018). Response of the Asian summer monsoons to idealized precession and obliquity forcing in a set of GCMs. *Quaternary Science Reviews*, 188, 121–135. https://doi.org/10.1016/j.quascirev.2018.03.025

Breitenbach, S. F. M., Adkins, J. F., Meyer, H., Marwan, N., Kumar, K. K., & Haug, G. H. (2010). Strong influence of water vapor source dynamics on stable isotopes in precipitation observed in Southern Meghalaya, NE India. *Earth and Planetary Science Letters*, 292(1–2), 212–220. https://doi.org/10.1016/j.epsl.2010.01.038

Cai, Y., Fung, I. Y., Edwards, R. L., An, Z., Cheng, H., Lee, J. E., et al. (2015). Variability of stalagmite-inferred Indian monsoon precipitation over the past 252,000 y. *Proceedings of the National Academy of Sciences*, 112(10), 2954–2959. https://doi.org/10.1073/pnas.1424035112

Caley, T., Malaizé, B., Zaragosi, S., Rossignol, L., Bourget, J., Eynaud, F., et al. (2011). New Arabian Sea records help decipher orbital timing of Indo-Asian monsoon. *Earth and Planetary Science Letters*, 308(3–4), 433–444. https://doi.org/10.1016/J.EPSL.2011.06.019

Caley, T., Roche, D. M., & Renssen, H. (2014). Orbital Asian summer monsoon dynamics revealed using an isotope-enabled global climate model. *Nature Communications*, 5(1), 5371. https://doi.org/10.1038/ncomms6371

Chabangborn, A., Brandefelt, J., & Wohlfarth, B. (2014). Asian monsoon climate during the Last Glacial Maximum: paleo-data-model comparisons. *Boreas*, 43(1), 220–242. https://doi.org/10.1111/bor.12032

Cheng, H., Edwards, R. L., Sinha, A., Spötl, C., Yi, L., Chen, S., et al. (2016). The Asian monsoon over the past 640,000 years and ice age terminations. *Nature*, 534(7609), 640–646. https://doi.org/10.1038/nature18591

Clemens, S. C., Holbourn, A., Kubota, Y., Lee, K. E., Liu, Z., Chen, G., et al. (2018). Precession-band variance missing from East Asian monsoon runoff. *Nature Communications*, 9(1), 3364. https://doi.org/10.1038/s41467-018-05814-0

Clemens, S.C., Kuhnt, W., LeVay, L. J., & Scientists, E. 353. (2016). Site U1446. *Proceedings of the International Ocean Discovery Program*, 353. https://doi.org/10.14379/iodp.proc.353.106.2016

Clemens, Steven C, & Prell, W. L. (2003). A 350,000 year summer-monsoon multi-proxy stack from the Owen Ridge, Northern Arabian Sea. *Marine Geology*, 201(1–3), 35–51. https://doi.org/10.1016/S0025-3227(03)00207-X

Contreras-Rosales, L. A., Jennerjahn, T., Tharammal, T., Meyer, V., Lückge, A., Paul, A., & Schefuß, E. (2014). Evolution of the Indian Summer Monsoon and terrestrial vegetation in the Bengal region during the past 18 ka. *Quaternary Science Reviews*, 102, 133–148. https://doi.org/10.1016/J.QUASCIREV.2014.08.010

Dinezio, P. N., & Tierney, J. E. (2013). The effect of sea level on glacial Indo-Pacific climate. *Nature Geoscience*, 6(6), 485–491. https://doi.org/10.1038/ngeo1823

Douglas, P. M. J., Pagani, M., Brenner, M., Hodell, D. A., & Curtis, J. H. (2012). Aridity and vegetation composition are important determinants of leaf-wax δD values in southeastern Mexico and Central America. *Geochimica et Cosmochimica Acta*, 97, 24–45. https://doi.org/10.1016/j.gca.2012.09.005

Dunlea, A., Giosan, L., & Huang, Y. (2020). Pliocene expansion of C4 vegetation in the core monsoon zone on the Indian Peninsula. *Climate of The Past*, 16, 2533–2546. https://doi.org/10.5194/cp-16-2533-2020

French, K. L., Hein, C. J., Haghipour, N., Wacker, L., Kudrass, H. R., Eglinton, T. I., & Galy, V. (2018). Millennial soil retention of terrestrial organic matter deposited in the Bengal Fan. *Scientific Reports*, 8(1). https://doi.org/10.1038/s41598-018-30091-8

Gadgil, S. (2003). The Indian Monsoon and its Variability. *Annual Review of Earth and Planetary Sciences*, 31(1), 429–467. https://doi.org/10.1146/annurev.earth.31.100901.141251

Gadgil, S., & Gadgil, S. (2006). The Indian monsoon, GDP and agriculture. *Economic & Political Weekly*, 41(47), 4887–4895. https://doi.org/10.2307/4418949

Galy, V., & Eglinton, T. (2011). Protracted storage of biospheric carbon in the Ganges–Brahmaputra basin. *Nature Geoscience*, 4(12), 843–847. https://doi.org/10.1038/ngeo1293

Galy, V., Eglinton, T., France-Lanord, C., & Sylva, S. (2011). The provenance of vegetation and environmental signatures encoded in vascular plant biomarkers carried by the Ganges-Brahmaputra rivers. *Earth and Planetary Science Letters*, 304(1–2), 1–12. https://doi.org/10.1016/j.epsl.2011.02.003

Gebregiorgis, D, Hathorne, E. C., Giosan, L., Clemens, S., Nürnberg, D., & Frank, M. (2018). Southern Hemisphere forcing of South Asian monsoon precipitation over the past ~1 million years. *Nature Communications*, 9(1), 4702. https://doi.org/10.1038/s41467-018-07076-2

Gebregiorgis, Daniel, Clemens, S., Hathorne, E., Giosan, L., Thirumalai, K., & Frank, M. (2020). A Brief Commentary on the Interpretation of Chinese Speleothem $\delta^{18}O$ Records as Summer Monsoon Intensity Tracers. *Quaternary*, 3(1), 7. https://doi.org/10.3390/quat3010007

Giosan, L., Ponton, C., Usman, M., Blusztajn, J., Fuller, D. Q., Galy, V., et al. (2017). Massive erosion in monsoonal central India linked to late Holocene land cover degradation. *Earth Surface Dynamics*, 5(4), 781–789. https://doi.org/10.5194/esurf-5-781-2017

Hein, C. J., Galy, V., Galy, A., France-Lanord, C., Kudrass, H., & Schwenk, T. (2017). Post-glacial climate forcing of surface processes in the Ganges–Brahmaputra River basin and implications for carbon sequestration. *Earth and Planetary Science Letters*, 478, 89–101. https://doi.org/10.1016/J.EPSL.2017.08.013

Howell, P., Pisias, N., Ballance, J., Baughman, J., & Ochs, L. (2006). ARAND Time-Series Analysis Software. Providence, R.I.: Brown University.

Hu, J., Emile-Geay, J., Tabor, C., Nusbaumer, J., & Partin, J. (2019). Deciphering Oxygen Isotope Records from Chinese Speleothems with an Isotope-Enabled Climate Model.

Paleoceanography and Paleoclimatology, 2019PA003741. https://doi.org/10.1029/2019PA003741
Hurley, J. V., & Boos, W. R. (2015). A global climatology of monsoon low-pressure systems. *Quarterly Journal of the Royal Meteorological Society*, 141(689), 1049–1064. https://doi.org/10.1002/qj.2447
IAEA/WMO. (2019). Global Network of Isotopes in Precipitation. The GNIP Database. Accessible at: https://nucleus.iaea.org/wiser.
Jalihal, C., Helena Catharina Bosmans, J., Srinivasan, J., & Chakraborty, A. (2019). The response of tropical precipitation to Earth's precession: the role of energy fluxes and vertical stability. *Climate of the Past*, 15, 449–462. https://doi.org/10.5194/cp-15-449-2019
Kathayat, G., Cheng, H., Sinha, A., Spötl, C., Edwards, R. L., Zhang, H., et al. (2016). Indian monsoon variability on millennial-orbital timescales. *Scientific Reports*, 6(1), 24374. https://doi.org/10.1038/srep24374
Konecky, B., Russell, J., & Bijaksana, S. (2016). Glacial aridity in central Indonesia coeval with intensified monsoon circulation. *Earth and Planetary Science Letters*, 437, 15–24. https://doi.org/10.1016/j.epsl.2015.12.037
Kumar, B., Rai, S. P., Kumar, U. S., Verma, S. K., Garg, P., Kumar, S. V. V., et al. (2010). Isotopic characteristics of Indian precipitation. *Water Resources Research*, 46(12). https://doi.org/10.1029/2009WR008532
Laskar, J., Robutel, P., Joutel, F., Gastineau, M., Correria, A. C. M., & Levrard, B. (2004). A long-term numerical solution for the insolation quantities of the Earth. *Astronomy and Astrophysics*, 428, 261–285. https://doi.org/10.1051/0004-6361:20041335
Lee, J., Fox-Kemper, B., Horvat, C., & Ming, Y. (2019). The response of East Asian monsoon to the precessional cycle: A new study using the Geophysical Fluid Dynamics Laboratory model. *Geophysical Research Letters*. https://doi.org/10.1029/2019gl082661
Lisiecki, L. E., & Raymo, M. E. (2005). A Pliocene-Pleistocene stack of 57 globally distributed benthic δ18O records. *Paleoceanography*, 20(1), 1–17. https://doi.org/10.1029/2004PA001071
Lo, L., Chang, S. P., Wei, K. Y., Lee, S. Y., Ou, T. H., Chen, Y. C., et al. (2017). Nonlinear climatic sensitivity to greenhouse gases over past 4 glacial/interglacial cycles. *Scientific Reports*, 7(1), 1–7. https://doi.org/10.1038/s41598-017-04031-x
Loulergue, L., Schilt, A., Spahni, R., Masson-Delmotte, V., Blunier, T., Lemieux, B., et al. (2008). Orbital and millennial-scale features of atmospheric CH_4 over the past 800,000 years. *Nature*, 453(7193), 383–386. https://doi.org/10.1038/nature06950
Paillard, D., Labeyrie, L., & Yiou, P. (1996). Macintosh Program performs time-series analysis. *Eos, Transactions American Geophysical Union*, 77(39), 379–379. https://doi.org/10.1029/96EO00259
Pathak, A., Ghosh, S., Alejandro Martinez, J., Dominguez, F., & Kumar, P. (2017). Role of oceanic and land moisture sources and transport in the seasonal and interannual variability of summer monsoon in India. *Journal of Climate*, 30(5), 1839–1859. https://doi.org/10.1175/JCLI-D-16-0156.1
Rao, Z., Li, Y., Zhang, J., Jia, G., & Chen, F. (2016). Investigating the long-term palaeoclimatic controls on the δD and $\delta^{18}O$ of precipitation during the Holocene in the Indian and East Asian monsoonal regions. *Earth-Science Reviews*, 159, 292–305. https://doi.org/10.1016/J.EARSCIREV.2016.06.007
Roy, P. S., Behera, M. D., Murthy, M. S. R., Roy, A., Singh, S., Kushwaha, S. P. S., et al. (2015). New vegetation type map of India prepared using satellite remote sensing: Comparison with global vegetation maps and utilities. *International Journal of Applied Earth Observation and Geoinformation*, 39, 142–159. https://doi.org/10.1016/j.jag.2015.03.003
Ryan, W. B. F., S.M. Carbotte, J. Coplan, S. O'Hara, A. Melkonian, R. Arko, R.A. Weissel, V. Ferrini, A. Goodwillie, F. Nitsche, J. Bonczkowski, and R. Zemsky (2009), Global Multi-

Resolution Topography (GMRT) synthesis data set, *Geochem. Geophys. Geosyst.*, 10, Q03014. https://doi.org/10.1029/2008GC002332

Sachse, D., Billault, I., Bowen, G. J., Chikaraishi, Y., Dawson, T. E., Feakins, S. J., et al. (2012). Molecular Paleohydrology: Interpreting the Hydrogen-Isotopic Composition of Lipid Biomarkers from Photosynthesizing Organisms. *Annu. Rev. Earth Planet. Sci*, 40(1), 221–49. https://doi.org/10.1146/annurev-earth-042711-105535

Sarkar, S., Prasad, S., Wilkes, H., Riedel, N., Stebich, M., Basavaiah, N., & Sachse, D. (2015). Monsoon source shifts during the drying mid-Holocene: Biomarker isotope based evidence from the core "monsoon zone" (CMZ) of India. *Quaternary Science Reviews*, 123, 144–157. https://doi.org/10.1016/j.quascirev.2015.06.020

Schrag, D. P., Hampt, G., & Murray, D. W. (1996). Pore Fluid Constraints on the Temperature and Oxygen Isotopic Composition of the Glacial Ocean. *Science*, 272(5270), 1930–2. https://doi.org/10.1126/science.272.5270.1930

Seth, A., Giannini, A., Rojas, M., Rauscher, S. A., Bordoni, S., Singh, D., & Camargo, S. J. (2019). Monsoon Responses to Climate Changes—Connecting Past, Present and Future. *Current Climate Change Reports*, 5(2), 63–79. https://doi.org/10.1007/s40641-019-00125-y

Shukla, J. (2007). Monsoon mysteries. *Science*, 318(5848), 204–205. https://doi.org/10.1126/science.1150045

Tabor, C. R., Otto-Bliesner, B. L., Brady, E. C., Nusbaumer, J., Zhu, J., Erb, M. P., et al. (2018). Interpreting Precession-Driven $\delta^{18}O$ Variability in the South Asian Monsoon Region. *Journal of Geophysical Research: Atmospheres*, 123(11), 5927–5946. https://doi.org/10.1029/2018JD028424

Wang, B., Xiang, B., Li, J., Webster, P. J., Rajeevan, M. N., Liu, J., & Ha, K. J. (2015). Rethinking Indian monsoon rainfall prediction in the context of recent global warming. *Nature Communications*, 6(1), 7154. https://doi.org/10.1038/ncomms8154

Yatagai, A., Kamiguchi, K., Arakawa, O., Hamada, A., Yasutomi, N., & Kitoh, A. (2012). Aphrodite constructing a long-term daily gridded precipitation dataset for Asia based on a dense network of rain gauges. *Bulletin of the American Meteorological Society*, 93(9), 1401–1415. https://doi.org/10.1175/BAMS-D-11-00122.1

Yoon, J.-H., & Chen, T.-C. (2005). Water vapor budget of the Indian monsoon depression. *Tellus A: Dynamic Meteorology and Oceanography*, 57(5), 770–782. https://doi.org/10.3402/tellusa.v57i5.14737

Zhang, H., Cheng, H., Baker, J., & Kathayat, G. (2020). Response to Comments by Daniel Gebregiorgis et al. "A Brief Commentary on the Interpretation of Chinese Speleothem $\delta^{18}O$ Records as Summer Monsoon Intensity Tracers". *Quaternary*, 3, 7. Quaternary, 3(1), 8. https://doi.org/10.3390/quat3010008

Zorzi, C., Sanchez Goñi, M. F., Anupama, K., Prasad, S., Hanquiez, V., Johnson, J., & Giosan, L. (2015). Indian monsoon variations during three contrasting climatic periods: The Holocene, Heinrich Stadial 2 and the last interglacial-glacial transition. *Quaternary Science Reviews*, 125, 50–60. https://doi.org/10.1016/j.quascirev.2015.06.009

CHAPTER 2:

BAY OF BENGAL PRECIPITATION ISOTOPE GRADIENTS REFLECT CONTINENTALITY OF PLEISTOCENE INDIAN SUMMER MONSOON MOISTURE TRANSPORT PATHS

S. M. McGrath[1], S. C. Clemens[1], Y. Huang[1]

[1] *Department of Earth, Environmental, and Planetary Sciences, Brown University, Providence, Rhode Island, USA,*

Key points

- U1448 $\delta D_{wax\text{-}veg}$, a precipitation isotope proxy, shows half the glacial-interglacial variability compared to U1446 $\delta D_{wax\text{-}veg}$ suggesting a more stable, proximal moisture source feeds the Indian Summer Monsoon branch over Andaman Islands, Irrawaddy River, and Salween River basins compared to the core monsoon zone of India.
- Compared to U1448, U1446 $\delta D_{wax\text{-}veg}$ has large interglacial variability attributed to moisture sources and transport paths. The larger interglacial sea surface temperature (SST) variability of Bay of Bengal SST gradients promotes both proximal convective and distal advective systems that into the core monsoon zone of India during interglacials
- The stable water isotope tracer-enabled version of the Community Earth System Model (iCESM) consistently underestimates precipitation isotope ranges and does not replicate proxy precipitation isotope gradient across the Bay of Bengal.

Abstract

Indian Summer Monsoon precipitation proxies show different phase (timing) responses relative to orbital scale forcings. While all precipitation proxies show significant orbital structure across eccentricity, obliquity, and precession cycles, precipitation isotope proxies lead runoff proxies over precession and obliquity cycles by about 4 and 7 kyr, respectively. Here we present an orbital scale terrestrial-based precipitation isotope ($\delta D_{wax\text{-}veg}$) reconstructed based on leaf wax δD from Site U1448 in the Andaman Sea over the last 640 kyr. Site U1448 captures terrestrial Indian Summer Monsoon hydrologic changes from the Irrawaddy basin, Salween basin, and Andaman Islands. We interpret the δD variability to reflect Indian Summer Monsoon circulation encompassing changes in precipitation, moisture source, and moisture transport dynamics. We find rainfall/runoff (NGHP-17 $\delta^{18}O_{sw}$) and precipitation isotope ($\delta D_{wax\text{-}veg}$) proxies from the Andaman Sea, are coherent across eccentricity and precession and have the consistent lead/lag phase relationship with those from Indian Margin Site U1446. Comparison of δD records from the eastern (Andaman Sea Site U1448) and western (Indian Margin Site U1446) Bay of Bengal shows a muted U1448 glacial-interglacial precipitation isotope variability suggesting a more stable, proximal moisture source feeds the Indian Summer Monsoon branch over Andaman Islands, Irrawaddy River, and Salween River basins. Larger interglacial U1446 precipitation isotope and sea surface temperature (SST) variability suggest Bay of Bengal SST gradients promoted both proximal Bay of Bengal convective systems and distal Indian Ocean advective systems into the core monsoon zone during interglacials. The gradient between Site U1446 and U1448 indicates that the core monsoon zone (U1446) precipitation isotopes are lighter

and more variable due to distal moisture sources and transport paths. The proxy precipitation isotope gradient is not replicated in stable water isotope tracer-enabled version of the Community Earth System Model (iCESM), which suggests the opposite gradient between these sites.

1. Introduction

Monsoon rainfall is critical to the billions of people living within India and the Southeast Asia peninsula where the summer rainfall can supply over 90% of the annual rains (Fig. 1). Variability of the summer monsoon circulation and rainfall is predicted to increase with modern climate change (Gadgil, 2003). Here we reconstruct monsoon variability over the orbital scale in the Late Pleistocene for Andaman Sea Site U1448.

Monsoon rainfall is difficult to reconstruct in the past due to a lack of quantitative proxies that are directly comparable to models. However, precipitation isotopes are powerful paleoclimate proxies that give insights on hydroclimate. Precipitation isotopes yield information about monsoon precipitation, moisture source, transport dynamics. Precipitation isotopes can be reconstructed from a multitude of proxy types including leaf waxes and speleothems. Additionally, models incorporate precipitation isotopes allowing direct model-proxy comparisons.

Multiple seasonal studies of precipitation isotopes collected over the Andaman Islands show there is a local amount effect (Laskar et al., 2013) and that precipitation isotopes are also influenced by moisture source and convective activity, with distal moisture sources and deep convection both leading to lighter values (Chakraborty et al., 2016). Sinha et al., (2019) study modern atmospheric moisture transport processes in the Bay of Bengal through precipitation isotopes. Overall, they find a positive correlation between the precipitation isotopes at the Andaman Islands and core monsoon zone of India rainfall amount and precipitation isotopes. The precipitation isotopes experience systematic depletions in response to large-scale convection occurring over the Bay of Bengal and are modulated by the integrated effect of convective activities. Seasonal precipitation isotopes appear to be linked with the monsoon intra-seasonal variability and synoptic scale fluctuations (Sinha et al., 2019).

Modern interannual studies over the Andaman Islands and Southeast Asia show precipitation isotopes are influenced by the amount effect, moisture source and transport, and convective activity. Over 80% of precipitation occurs during the summer monsoon season between May and September with moisture coming from the Arabian Sea and Western tropical Indian Ocean (Jaglan et al., 2020). The other 20% of precipitation occurs over the winter and comes from the Bay of Bengal and South China Sea (Jaglan et al., 2020). Wei et al. (2018) study interannual precipitation isotopes from multiple sites across the Southeast Asian peninsula showing that rainfall isotope ratios are both significantly correlated with local rainfall amount and regional outgoing longwave radiation, a measure for large scale convective activity. They find rainfall isotopes over Southeast Asia peninsula are not correlated with local air temperature, cloud-top pressure, or cloud-top temperature. This suggests that interannual rainfall isotope ratios in this region are controlled not only by local rain amount (amount effect) but also by large-scale circulation (Wei et al., 2018).

Recent studies show a that Indian Summer Monsoon (ISM) precipitation isotope proxies and qualitative ISM rainfall proxies show different phase (timing) responses relative to orbital scale forcings (Clemens et al., 2021; McGrath et al., 2021). In the core monsoon zone of India (Fig. 1), precipitation isotopes lead rainfall/runoff proxies over precession and obliquity cycles by about 4 and 7 kyr, respectively. This indicates that these proxies capture different aspects of the ISM system, with the phase difference highlighting the different forcing mechanisms of core monsoon zone circulation surrounding moisture source and transport verse ISM rainfall amount.

Here we compare the core monsoon zone of India precipitation isotope and rainfall signals with those from the Andaman Sea, where we created a 640 kyr orbital scale precipitation isotope proxy record from the Andaman Sea Site U1448. Hydrogen isotopes from leaf wax (δD_{wax}) are a proxy for terrestrial precipitation isotopes (δD_{precip}). δD_{wax} are the δD of long-chain ($>n\text{-}C_{25}$) lipid *n*-alkanoic acids, components of waxy coatings on terrestrial plant leaves that are transported by water and wind into the ocean and are preserved in sediments (Sachse et al., 2012). Study of modern δD_{wax} in the Ganges–Brahmaputra basin has been demonstrated as a reliable proxy for basin-integrated δD_{precip} (Galy et al., 2011). The U1448 δD_{wax} record allows us to build on published seawater isotopes ($\delta^{18}O_{sw}$), a rainfall/runoff proxy at nearby Site NGHP-17. Through comparison with Site U1446 δD_{wax} record, we also investigate a precipitation isotope gradient across the Bay of Bengal, the core convective region of the Indian Summer Monsoon (ISM).

1.1 Site Description

IODP Expedition 353 recovered sediment from a rise in the Andaman Sea (eastern Bay of Bengal) Site U1448 (10°38.0'N, 93°00.0'E, 1091mbsl, 44km offshore) (Fig. 1) (Clemens et al., 2016). This site targets environmental and hydrologic changes from the Irrawaddy basin, Salween basin, and Andaman Islands. These areas experience over 90% of total annual rainfall during the summer monsoon season (June-August) with about 500 mm of rain per month and an average temperature of 28°C (Mitchell & Jones, 2005). Terrigenous sediment supply to the Andaman Sea is dominantly from the Irrawaddy and Salween Rivers (Colin et al., 1999, 2006) with contributions from the Indo-Burman-Arakan mountain ranges as well as the Andaman Islands (Awasthi et al., 2014). Due to Site U1448's location in the Andaman Sea, Little Andaman Island is likely a source of terrigenous materials as well. Although residence time could impose a lag in sedimentary systems, even in the much larger floodplain system of the Ganges-Brahmaputra catchment, leaf wax fatty acids have been shown to have short residence times (from 0.015 to 1.2 kyr) (French et al., 2018; Galy & Eglinton, 2011) that do not interfere with the timing of the forcing and response investigated here. Additionally, in previous orbital scale leaf wax studies within the Bay of Bengal, the phase relationships between the precipitation isotopes recorded from leaf waxes are in phase with the precipitation isotopes recorded in speleothems that have independent, well constrained age models (McGrath et al., 2021).

Glacial sea level changes may influence sediment supply to Site U1448. When sea level drops approximately 40 meters below modern sea level, the Andaman Islands become connected and the Andaman Sea connection to the Pacific Ocean is cutoff by the Sunda shelf exposure (Fig. 1). Additionally, as sea level drops the Irrawaddy and Salween deltas move closer to Site U1448. However, U1448 benthic foraminifera $\delta^{18}O$ record shows a good, continuous stratigraphy (Fig. 2) and the accumulation rates suggest a relatively stable sediment supply that mildly increases during glacial to interglacial transitions (Table 1).

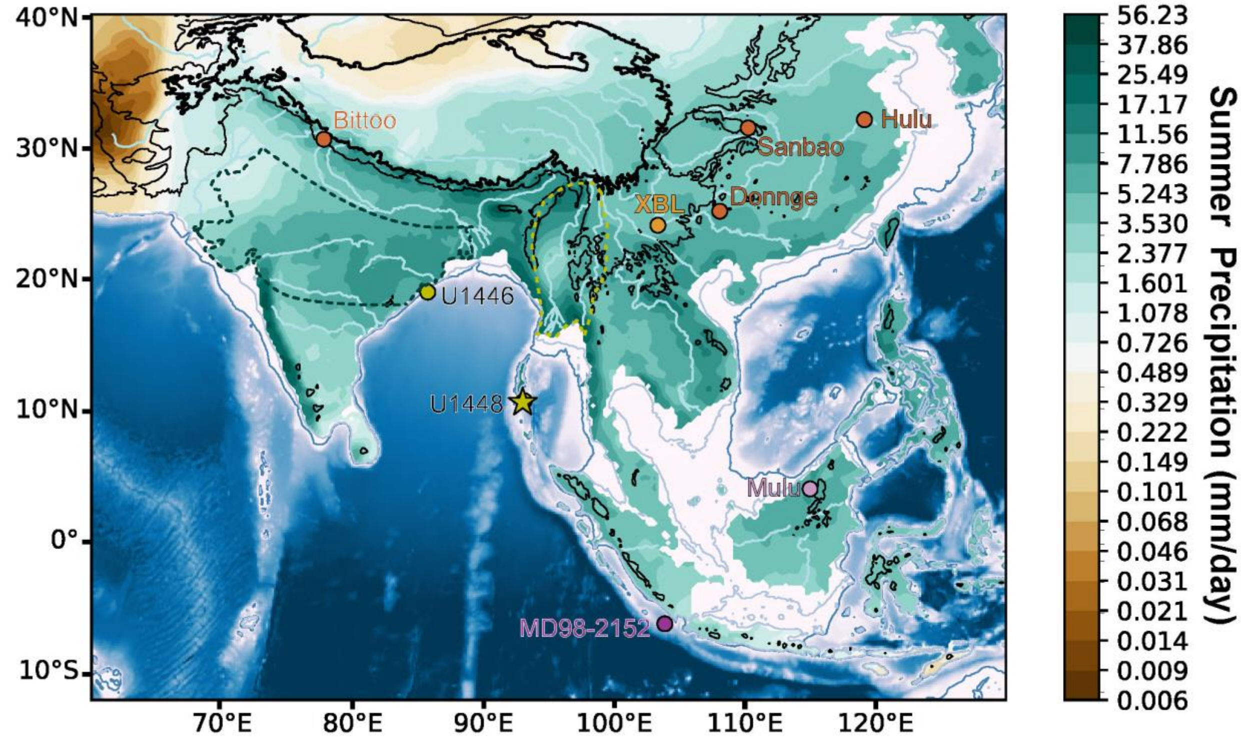

Figure 1.

Mean June-September precipitation from APHRODITE (mm day^{-1}; 1998-2015; V1901) (Yatagai et al., 2012) plotted with a logarithmic scale with ocean bathymetry (from GeoMapApp www.geomapapp.org). Over the ocean, the light blue contour indicates 40m below sea level, the dark blue contour indicates 120m below sea level. On land, thin black line contour indicates 1000m elevation, thick black line contour indicates 3000m elevation. The yellow dashed line outlines the Irrawaddy and Salween River Basins and the green dashed line outlines the core monsoon zone of India (Gadgil, 2003). The yellow star marks Site U1448 and NGHP-17.

2. Methods

2.1 Age Model

The age model of Site U1448 is based on two radiocarbon dates, and tie points between benthic foraminifera $\delta^{18}O$ and the LR04 global $\delta^{18}O$ benthic stack (Lisiecki & Raymo, 2005) using Analyseries (Paillard et al., 1996). Two radiocarbon dates are measured on *Globigerinoides ruber* (white *sensu stricto*) picked from the 250–355 μm size fraction. Details of the U1448 benthic record are available in Clemens (2022). Correlations, tie points, and radiocarbon dates are shown in Figure 2 and Table 1.

2.2 Organic Analyses

Lipids from 275 samples are extracted from 3 to 8 g of dry sediment with an Accelerated Solvent Extractor 200 (Dionex) with dichloromethane (DCM): methanol 9:1 (v: v). The extracts are dried under N_2 and separated on aminopropyl silica gel flash columns, eluting neutral fractions with DCM: isopropanol 2:1 (v: v) and acid fractions with 4% acetic acid in diethyl ether. All flash column separations use three column volumes of each eluent. Acid fractions are methylated in anhydrous 5% HCl in methanol at 60°C overnight. Samples are further cleaned using silica gel flash columns: polar compounds are removed with hexane, fatty acid methyl esters (FAMEs, our target compounds) are eluted with DCM. The δD of the C_{28} *n*-alkanoic acid are measured using Gas Chromatography-Pyrolysis Isotope Ratio Mass Spectrometry at Brown University. Samples are run in triplicate. The pooled standard deviation of triplicate samples is 1.8‰, and the standard deviation of a standard run every 3 injections is 2.5‰. The $\delta^{13}C$ of the C_{28} n-alkanoic acid are using Gas Chromatography-Pyrolysis Isotope Ratio Mass Spectrometry at Brown University. Samples are run in duplicate. The reproducibility of the $\delta^{13}C$ measurement based on repeated analyses was better than ± 0.2 ‰. Samples have been corrected for the methyl group added during fatty acid derivatization using the known isotopic composition of the acidified methanol used in methylation.

2.3 Vegetation Corrections

δD_{wax} are corrected for vegetation effects using paired $\delta^{13}C_{wax}$ measurements and methods outlined in Konecky et al. (2016). The δD_{wax} values were corrected for variable hydrogen isotope fractionation using C28*n*-acid endmember $\delta^{13}C$ values of -36.9‰ and -19.5‰ for C3 and C4 plants (Chikaraishi et al., 2004; Chikaraishi & Naraoka, 2007), respectively. On average the vegetation correction increases the $\delta D_{wax\ value}$ by 97‰.

Equation 6: $\%\mathbf{C_4} = \frac{\boldsymbol{\delta^{13}C_{wax} - \delta^{13}C_{C3}}}{\boldsymbol{\delta^{13}C_{C4} - \delta^{13}C_{C3}}}$

Equation 7: $\%\mathbf{C_3} = \mathbf{100} - \%\mathbf{C_4}$

where: $\delta^{13}C_{C3} = -19.5‰$ and $\delta^{13}C_{C4} = -36.9‰$

Equation 8: $\boldsymbol{\varepsilon}_{\mathbf{wax-Pveg}} = (\%\mathbf{C_3} * \boldsymbol{\varepsilon}_{\mathbf{C27.alk-P_{C3}}}) + (\%\mathbf{C_4} * \boldsymbol{\varepsilon}_{\mathbf{C27.alk-P_{C4}}}) + \boldsymbol{\varepsilon}_{\mathbf{alkane-acid}}$

where: $\varepsilon_{C27.alk-P_{C3}} = 128.9 \pm 29.8‰$,

$\varepsilon_{C27.alk-P_{C4}} = -125.4 \pm 34.0‰$, and $\varepsilon_{alkane-acid} = 25‰$.

Equation 9: $\boldsymbol{\delta D_{wax-veg}} = \frac{\boldsymbol{\delta D_{wax} + 1000}}{\boldsymbol{\varepsilon_{wax-Pveg}/1000 + 1}} - \mathbf{1000}$

3. Results

3.1. U1448 δD_{wax}

δD_{wax} records are corrected to allow for comparison with other precipitation isotope proxies, and modern precipitation isotope measurements. A common correction that is applied to δD_{wax} records is an ice volume correction that adjusts for the effect of global ice volume on the ocean isotopic reservoir, corrected by assuming a 1‰ ^{18}O-enrichment in the last glacial maximum (LGM) oceans (Schrag et al., 1996). Here we do not apply the ice volume correction because the sea-water enrichment is included in the modeling simulations; therefore, to ensure a direct comparison, the global ice volume signal must be included in the proxy data. Thus, here were only correct for the vegetation. All climatic interpretations are made from the corrected $\delta D_{wax\text{-}veg}$ record. However, the results and interpretation of the $\delta D_{wax\text{-}veg}$ record would be the same regardless of whether the vegetation correction is incorporated.

The δD_{wax} and $\delta D_{wax\text{-}veg}$ have the same structure, the vegetation correction shifts the $\delta D_{wax\text{-}veg}$ average by 97‰ heavier and increases the range by 3‰ (Fig. 2a). The average $\delta D_{wax\text{-}veg}$ value is -46‰. We calculate an average glacial-interglacial change to compare with other proxy locations and model simulations. We define glacial (interglacial) periods based on the timing of the Marine Isotope Stage (MIS) and U1448 benthic stratigraphy. Specifically, we define glacial periods as last glacial interval (14–72 ka), MIS 6 (126–190 ka), MIS 8 (244–300 ka), MIS 10 (338–373 ka), MIS 12 (426–477 ka), MIS 14 (526-563 ka) and MIS 16 (620-640 ka). Likewise, interglacial periods are defined as the MIS1 (0-12 ka), MIS 5 (73– 123 ka), MIS 7 (192-242 ka) and 241–235 ka), MIS 9 (302–336 ka), MIS 11 (377–423 ka), MIS 13 (479-523 ka), and MIS 15 (564-620 ka). Excluding the Holocene, interglacial values average -48‰, ranging 28‰ from -38‰ to -66‰ and glacial values average -45‰, ranging 23‰ from -34‰ to -57‰ (Fig. 4). The Holocene has enriched δD values compared to previous interglacial intervals (Fig. 2).

This glacial-interglacial structure is present in the spectral analysis of record. There is a large spectral peak at 100 kyr eccentricity frequency with minor peaks at 41 kyr obliquity, 23kyr and 19 kyr precession frequencies (Fig. 3b). Relative to ETP, a normalize average record of eccentricity, tilt (obliquity) and negative precession (June 21 perihelion), only obliquity is highly coherent. Coherence at other orbital bands is, however, significant with other proxy records as discussed below.

4. Discussion

4.1 U1448 $\delta D_{wax-veg}$ and Modern Precipitation Isotopes

The U1448 $\delta D_{wax-veg}$ Holocene values fall within range of modern hydrogen precipitation isotopes collected from over Andaman Islands, Irrawaddy River, and Salween River basins. The Holocene $\delta D_{wax-veg}$ average value is -43‰ with a range of 21‰. At the Andaman Islands, event based precipitation hydrogen isotopes vary from 6 to -50‰ δD (Chakraborty et al., 2016) There is a lack of spatial coverage for measurements over the Irrawaddy River and Salween River basins, however, a GNIP station at Yangoon, Myanmar (16°46′11.99″N, 96°10′11.99″E) has a 3-year weighted mean of -29.5 ± 1.5‰ (IAEA/WMO, 2019). Just outside the Salween River Basin, Chiang Mai, Thailand (18.8°N, 99.0°E, 313m) has a 12-year weighted mean of -48.1‰ (Wei et al., 2018).

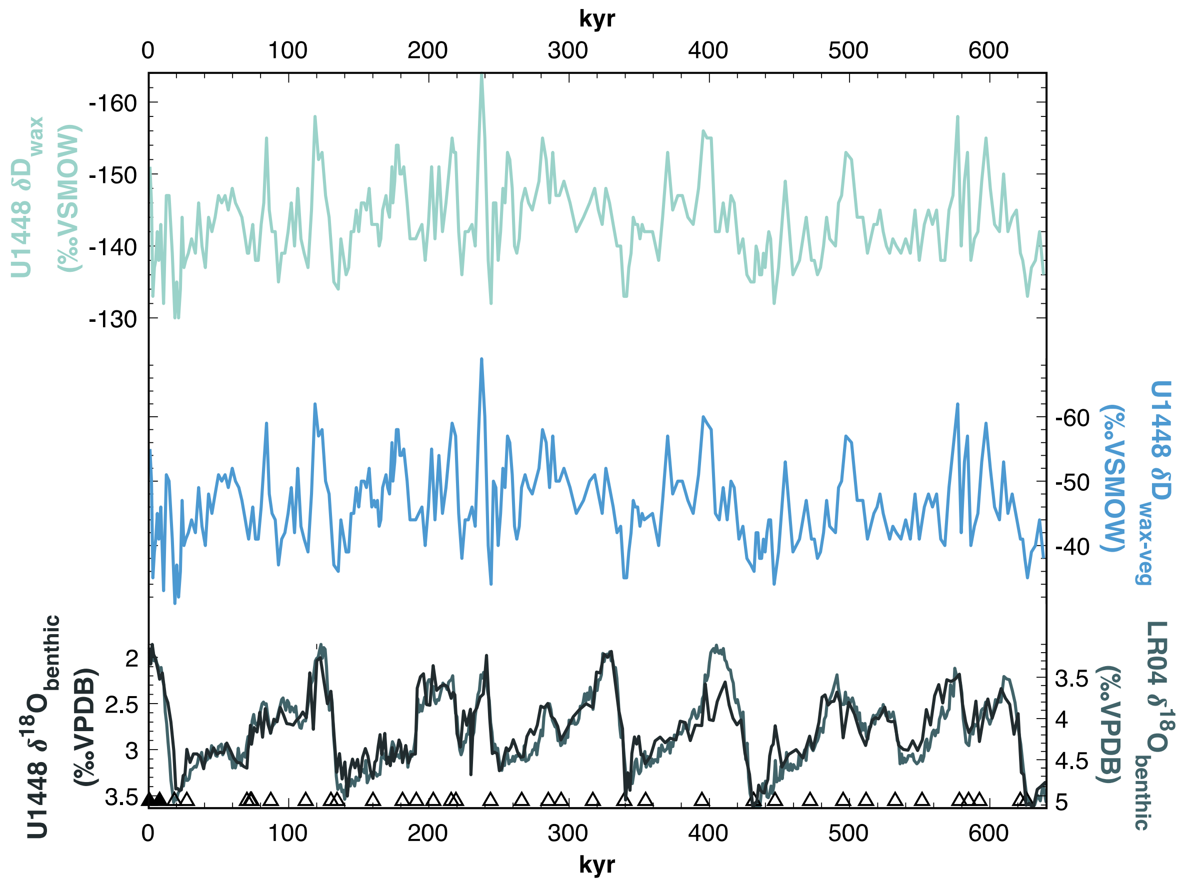

Figure 2

Proxy timeseries. From top to bottom: U1448 δD_{wax}, U1448 $\delta D_{wax\text{-}veg}$ and U1448 benthic $\delta^{18}O$ stratigraphy overlays the LR04 stack (Lisiecki & Raymo, 2005) with closed triangles indicating radiocarbon dates and open triangles indicating tie points.

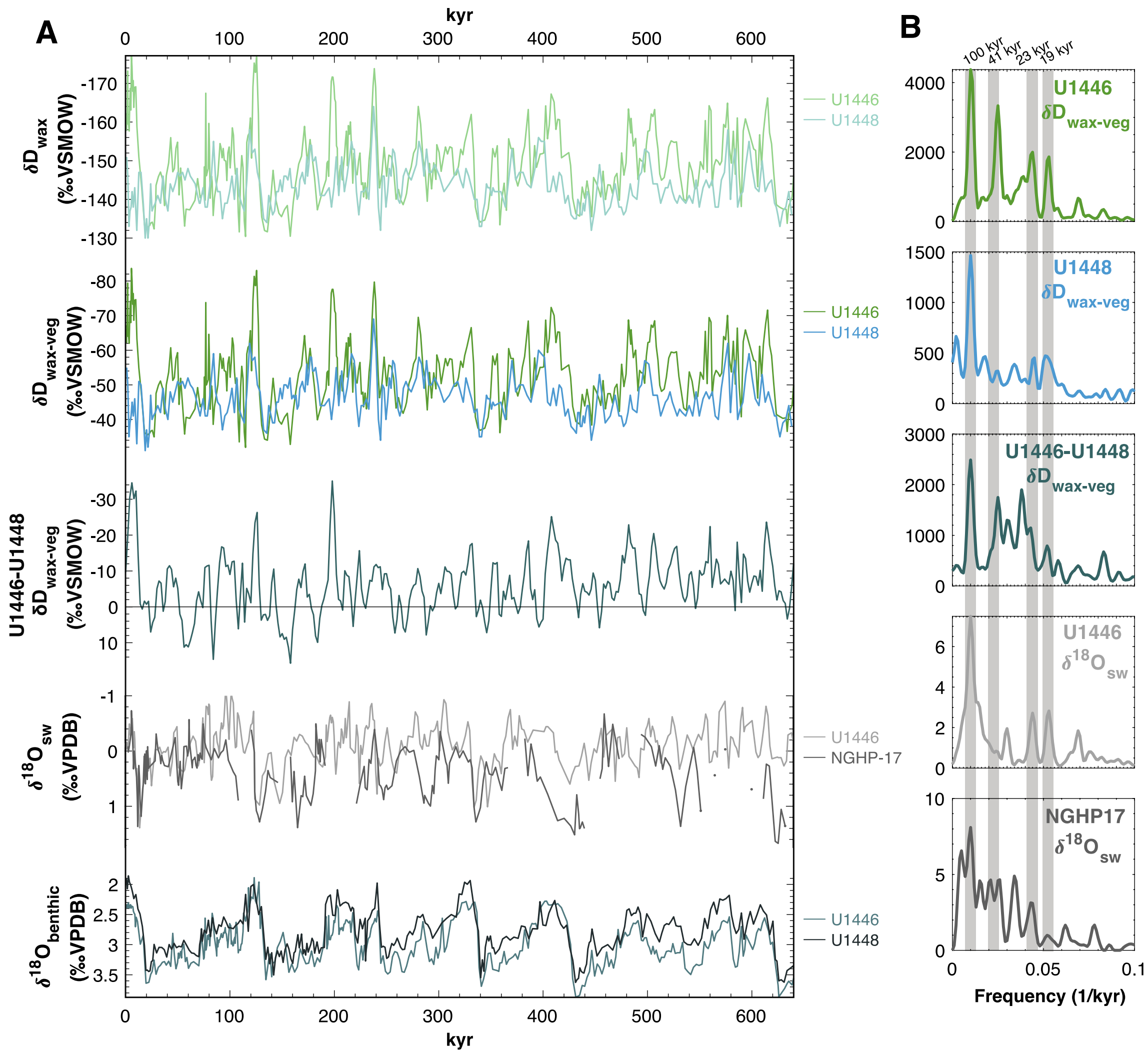

Figure 3

Precipitation and Seawater Isotopes timeseries and spectra. A) From top to bottom: δDwax records with U1448 in blue and U1446 in green, δDwax-veg records with U1448 in blue and U1446 in green, U1446 minus U1448 δDwax-veg, δ18Osw records with NGHP-17 in dark gray and U1446 in light gray, and benthic δ18O stratigraphy with U1848 in dark gray and U1446 in light gray. B) Spectral Power of U1446 δDwax-veg, U1448 δDwax-veg, U1446-U1448 δDwax-veg, U1446 δ18Osw, and NHGP-17 δ18Osw. The gray bars highlight 100-kyr eccentricity, 41-kyr obliquity, 23-kyr and 19-kyr precession frequencies.

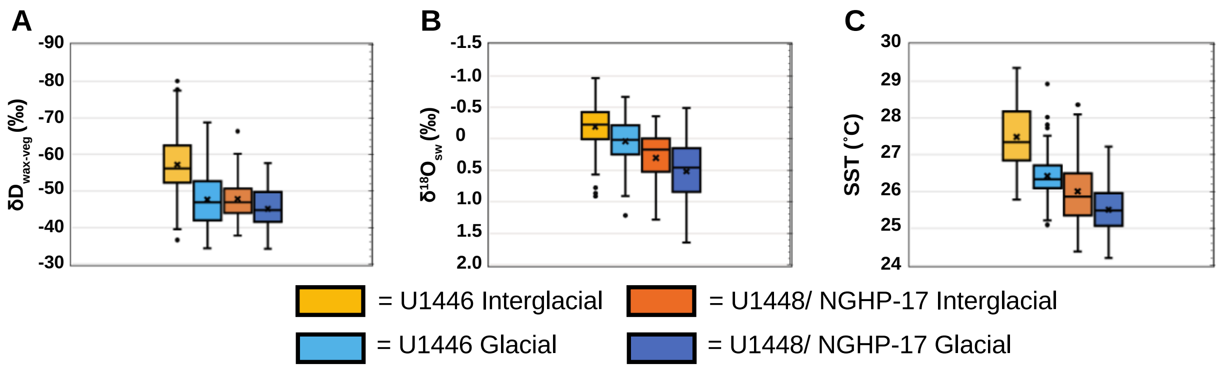

Figure 4

Box and whisker charts comparing the glacial-interglacial variability across the Bay of Bengal. A) U1446 and U1448 δDwax-veg B) U1446 and NGHP-17 δ18Osw, and C) U1446 Mg/Ca SST and NGHP-17 TEX86 SST corrected by -2 degrees offset to make it directly comparable with Mg/Ca SST estimates.

4.2 Local Precipitation and Seawater Isotopes

Site U1448 builds off Site NGHP-17, allowing for the direct comparison between precipitation isotopes and seawater isotopes. The NGHP-17 $\delta^{18}O_{seawater}$ signal is a proxy for Andaman Sea surface salinity (Gebregiorgis et al., 2018). Andaman Sea surface salinity is related to precipitation-evaporation rate, Bay of Bengal circulation, and river runoff. In the modern, river runoff is the main control of Bay of Bengal salinity, and changes in river runoff are dominated by ISM rainfall (Pant et al., 2015; Sengupta et al., 2006). Thus, commonalities between the NGHP-17 $\delta^{18}O_{seawater}$ record and the U1448 $\delta D_{wax\text{-}veg}$ record are likely due to the amount effect (Fig 3, Table 3).

U1448 $\delta D_{wax\text{-}veg}$ is highly coherent with NGHP-17 $\delta^{18}O_{seawater}$ across eccentricity and precession, with large phase offsets (Table 3). U1448 $\delta D_{wax\text{-}veg}$ always leads NGHP-17 $\delta^{18}O_{seawater}$, consistent with the phase relationships between Northern Indian Margin Site U1446 δD_{wax} (McGrath et al., 2021) and $\delta^{18}O_{seawater}$ (Clemens et al., 2021). The high coherence suggests that while there may be the amount effect over glacial-interglacial and precession cycles, the phasing (timing) of the lightest precipitation isotope occurs before the maximum rainfall and runoff. This is consistent with the modern observations that while the amount effect influences precipitation isotopes, it may not be the largest factor. The phase of the precipitation isotopes is likely set by changes of the large-scale monsoon circulation process including moisture source and transport. This indicates that large scale circulation changes lead maximum monsoon rainfall across the Bay of Bengal.

4.3 Regional Bay of Bengal Precipitation Isotope Records

Comparison of U1448 $\delta D_{wax-veg}$ record with Site U1446 (Northern Indian Margin) $\delta D_{wax-veg}$ record (McGrath et al., 2021), which collects the terrestrial precipitation isotope signal from the core monsoon zone of India, shows similar glacial-interglacial structure with large differences in amplitude. The average U1446 $\delta D_{wax-veg}$ value is -53‰, 7‰ lighter than the average U1448 $\delta D_{wax-veg}$ value (Fig 3). Additionally, the U1446 $\delta D_{wax-veg}$ record has a larger range of 52‰, with a maximum of -32‰ and a minimum of -84‰ (Fig. 3). U1448 and U1446 have similar maximum values, with the difference in range due to the lighter U1446 $\delta D_{wax-veg}$ minimum values.

Both U1448 and U1446 have glacial-interglacial variability, tending to be heavier during glacials and lighter during interglacials. U1446 $\delta D_{wax-veg}$ interglacial values average -57‰, ranging 43‰ from -37‰ to -80‰ and glacial values average -47‰, ranging 34‰ from -34‰ to -68‰. U1446 has an average glacial-interglacial difference of 10‰, larger than the U1448 average glacial-interglacial difference of 3‰ (Fig 4).

Spectral analysis shows U1448 and U1446 $\delta D_{wax-veg}$ records are highly coherent across eccentricity and within phase error, indicating a consistent basin-scale response (Table 3). This indicates that over eccentricity band the core monsoon zone and the Andaman Islands, Irrawaddy River, and Salween River Basins have similar precipitation, moisture source and transport dynamics over glacial-interglacial cycles. While U1448 and U1446 $\delta D_{wax-veg}$ records are highly coherent and in phase across obliquity, there is little spectral power at obliquity in U1448 $\delta D_{wax-veg}$ record. The low coherence at precession and lack of significant spectral power at obliquity is interpreted as the result of U1448 $\delta D_{wax-veg}$ lacking the transport path across India that drives light precipitation isotopes captured at Site U1446. However, relative to ETP, U1448 $\delta D_{wax\text{-}veg}$ shares the same precession and obliquity phase as U1446 precipitation isotopes that are in line with internal forcing from radiative effects of greenhouse gasses and ice volume (McGrath et al., 2021).

The differences in the U1448 and U1446 $\delta D_{wax\text{-}veg}$ records is explored by subtracting the U1448 $\delta D_{wax\text{-}veg}$ record from the U1446 $\delta D_{wax\text{-}veg}$ to look at the $\Delta\ \delta D_{wax\text{-}veg}$ (Fig 3). Differences in the eastern (U1448) and western (U1446) Bay of Bengal $\delta D_{wax\text{-}veg}$ records indicate regional heterogeneity possibly related to the convective (local Bay of Bengal) versus advective (from the Arabian Sea and western tropical Indian Ocean) moisture transport. When the $\Delta\ \delta D_{wax\text{-}veg}$ signal is negative, that indicates U1446 $\delta D_{wax\text{-}veg}$ is lighter, likely due to moisture transport from Arabian Sea and western tropical Indian Ocean that travels over the Indian subcontinent. The $\Delta\ \delta D_{wax\text{-}veg}$ has strong, coherent orbital frequencies (Fig. 3, Table 2). The orbital coherence and phasing of the $\Delta\ \delta D_{wax\text{-}veg}$ record is consistent with U1446 $\delta D_{wax\text{-}veg}$ signal and the findings in McGrath *et al.,* 2021 that lighter precipitation isotopes at Site U1446 are due to sourcing from distal regions and longer transport paths. U1448 $\delta D_{wax\text{-}veg}$ signal does not capture cross-continent moisture dynamics. Thus, the muted precipitation isotope signal at Site U1448 indicates that the Southeast Asian peninsula has a more stable, proximal moisture source than the core monsoon zone of India.

4.4 Precipitation Isotope Interglacial Variability

There is much larger interglacial variability and range within U1446 $\delta D_{wax\text{-}veg}$ compared to U1448 $\delta D_{wax\text{-}veg}$ (Fig. 4). Increased precipitation isotope ranges during interglacial suggest a more erratic monsoon circulation system feeding into the core monsoon zone compared to the Andaman Islands, Irrawaddy River, and Salween River Basins. Rainfall/runoff salinity proxies from the Bay of Bengal (U1446 (Clemens et al., 2021) and NGHP-17 (Gebregiorgis et al., 2018) $\delta^{18}O_{seawater}$) both show increased mean rainfall/runoff during interglacial compared to their glacial values, and the variability is consistent: U1446 has a about 1.5‰ $\delta^{18}O_{seawater}$ range during both glacials and interglacials and NGHP-17 has about a 1.75‰ $\delta^{18}O_{seawater}$ range during interglacials and a larger 2.1‰ $\delta^{18}O_{seawater}$ range during glacials (Fig. 4). Thus, the interglacial precipitation isotope variability is likely not driven by rainfall changes, but by changes in monsoon circulation surrounding moisture source and transport.

Both sites have sea surface temperature (SST) proxies. Site U1446 TEX86 SST is corrected by 2 degrees in order to bring the temperature in range of the Mg/Ca measured at Site U1446 (Clemens et al., 2021) and directly compare with the NGHP-17 Mg/Ca SST record (Gebregiorgis et al., 2018). The sea surface temperature (SST) proxies at Site U1446 and NGHP-17 both show warmer and larger interglacial SST variability (Fig. 4). This suggests the increased interglacial moisture source and transport variability to the core monsoon zone may be sensitive to Bay of Bengal SSTs, with warmer and larger Bay of Bengal SST gradients promoting both proximal Bay of Bengal convective systems and distal advective moisture from the tropical western Indian Ocean. Proximal Bay of Bengal convective systems contribute relatively heavier isotopes than the distal advective moisture from the tropical western Indian Ocean leading to a large range of precipitation isotope values during interglacials.

4.5 Comparison with Asian Orbital-Scale Precipitation Isotope Proxy Records

Precipitation isotope records across India and southeast Asia show similar spectral structures. Across the India Summer Monsoon system, U1446 and U1448 $\delta D_{wax-veg}$, as well as speleothems $\delta^{18}O$ records from Bittoo (Kathayat et al., 2016) and Xiabialong (XBL) (Cai et al., 2015) exhibit strong glacial-interglacial signals (Fig. 5a). All have strong eccentricity spectral power (Fig 5b). Spectral analysis shows the speleothems $\delta^{18}O$ records have lower coherence with Site U1448 $\delta D_{wax-veg}$ (Table 3) than with U1446 $\delta D_{wax-veg}$ (Chp 1, Table S3)

Further south Mulu (Borneo) speleothems $\delta^{18}O$ (Carolin et al., 2016; Meckler et al., 2012) and Sumatra MD98-2512 $\delta D_{wax-veg}$ (Windler et al., 2020) exhibit similar spectral structures as the precipitation isotopes from the ISM region, dominated by eccentricity, with lesser amounts of precession and obliquity. Both Mulu $\delta^{18}O$ and MD98-2512 $\delta D_{wax-veg}$ are highly coherent across eccentricity and precession with U1448 $\delta D_{wax-veg}$. At eccentricity, Mulu $\delta^{18}O$, MD98-2512 $\delta D_{wax-veg}$ and U1448 $\delta D_{wax-veg}$ are all in phase suggesting similar glacial-interglacial forcings influence the precipitation isotopes. Mulu, MD98-2512 and U1448 precipitation isotopes are likely impacted by sea level change due to large shelf exposure over the Andaman Sea at Site U1448 and the Sunda Shelf proximity to Mulu and Site MD98-2512. As shelf exposure increases during glacials, transport paths over land increase leading to lighter precipitation isotopes and potentially dampening the magnitude of glacial-interglacial amplitude precipitation isotope change.

These findings further highlight a common glacial-interglacial variability in precipitation isotopes across the ISM and southeast Asia (McGrath et al., 2021; Windler et al., 2021). The East Asian speleothems (Cheng et al., 2016) are the only precipitation isotope that does not show dominant eccentricity or glacial- interglacial variability. If, as studies suggest, the East Asian speleothems capture the upstream depletion from ISM (Pausata et al., 2011), then we would expect to find amplified signals of ISM precipitation isotopes within the East Asian speleothems. However, the lack of dominant eccentricity and glacial-interglacial variability suggest East Asian speleothems do not represent regional ISM variability at orbital time scales (McGrath et al., 2021; Windler et al., 2021).

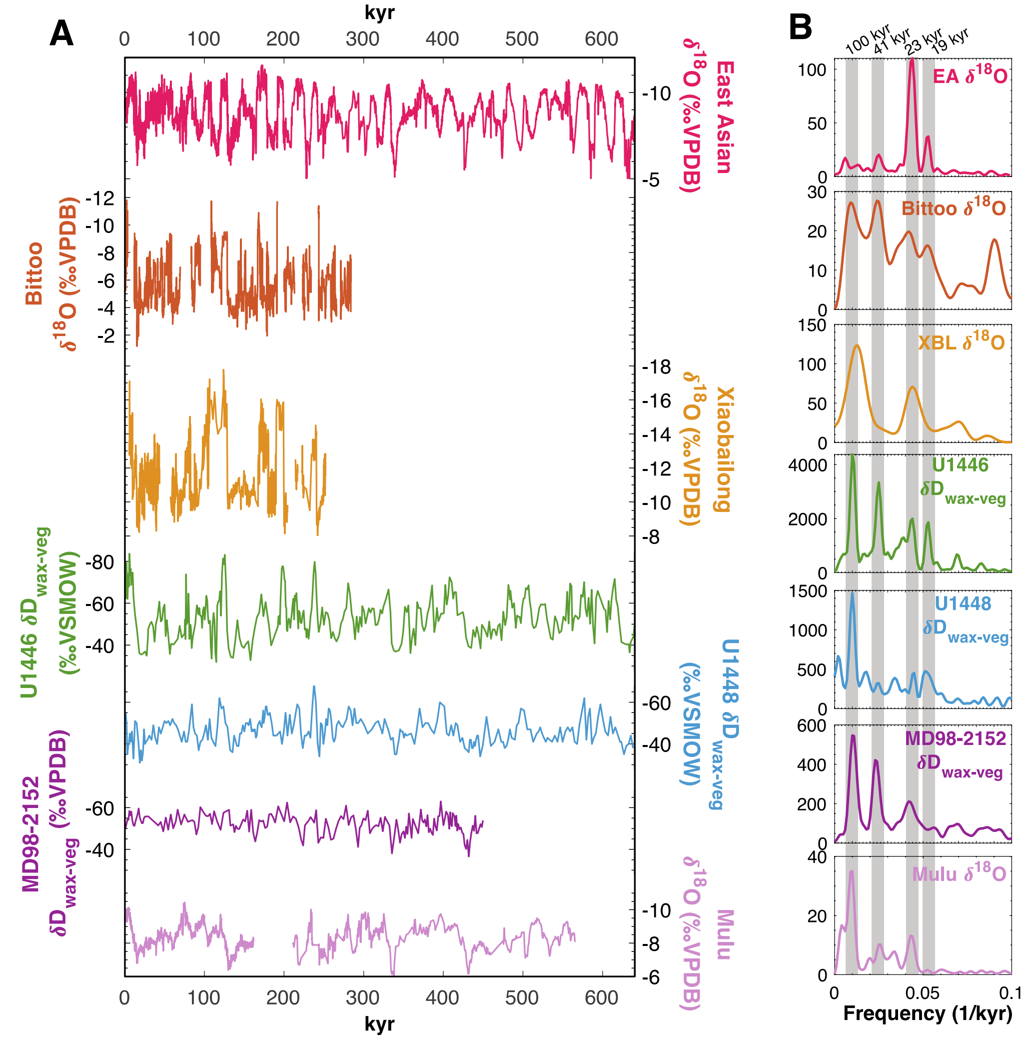

Figure 5

Orbital scale precipitation isotope proxy records of A) timeseries and B) spectra. From top to bottom: East Asian speleothem $\delta^{18}O$ (Cheng et al., 2016), Bittoo speleothem $\delta^{18}O$ (Kathayat et al., 2016), Xiaobailong (XBL) speleothem $\delta^{18}O$ (Cai et al., 2015), U1446 $\delta D_{wax\text{-}veg}$ (McGrath et al., 2021), U1448 $\delta D_{wax\text{-}veg}$, MD98-2152 $\delta D_{wax\text{-}veg}$ (Windler et al., 2020) and Mulu (Borneo) speleothem $\delta^{18}O$ (Carolin et al., 2016; Meckler et al., 2012). The gray bars highlight 100-kyr eccentricity, 41-kyr obliquity, 23-kyr and 19-kyr precession frequencies.

4.6 Model Comparison

The stable water isotope tracer-enabled version of the Community Earth System Model (iCESM) is a current state-of-the-art coupled climate model that best simulates the relationship between precipitation isotope and convective activity (Hu et al., 2018). This model has been used to explore precipitation isotopes over the Asian monsoon region relative to insolation (Hu et al., 2019; Tabor et al., 2018) and glacial-interglacial (Windler et al., 2020) variability.

Modeled precipitation isotopes over the Andaman Islands, Irrawaddy River, and Salween River Basins have a smaller range compared to the U1448 $\delta D_{wax-veg}$ precipitation isotope proxy. Over precession-scale insolation changes, there is a modeled ~2‰ $\delta^{18}O$ (~16‰ δD) summer monsoon precipitation isotope change (Hu et al., 2019; Tabor et al., 2018) whereas the U1448 $\delta D_{wax-veg}$ exhibits an average of about 20‰ δD (~2.5‰ $\delta^{18}O$) range over precession cycles. Over glacial-interglacial conditions, the model varies spatially across the Andaman Islands, Irrawaddy River, and Salween River Basins, exhibiting glacial-interglacial differences from +8 to -8‰ δD, with lighter values further east over land (Windler et al., 2020). The U1448 $\delta D_{wax-veg}$ precipitation isotope proxy has a glacial-interglacial transition difference average of -12‰ δD (Fig. 2), larger than the modeled difference (-8‰ δD). The underestimation of precipitation isotope insolation and glacial-interglacial range is apparent across the ISM with U1446 $\delta D_{wax-veg}$ (McGrath et al., 2021) and Bittoo $\delta^{18}O$ (Tabor et al., 2018) ranges larger than the modeled precipitation isotopes.

The modeled precipitation isotope gradient across the Bay of Bengal does not align with the precipitation isotope proxies. The model consistently shows larger changes in precipitation isotopes over Andaman Islands, Irrawaddy River, and Salween River Basin than core monsoon zone of India. Over insolation changes, the model shows a 1‰ $\delta^{18}O$ difference between the core monsoon zone and the Andaman Islands and Irrawaddy River, with Andaman Islands, Irrawaddy River, and Salween River Basin exhibiting lighter values (Hu et al., 2019; Tabor et al., 2018). The U1446-U1448 Δ $\delta D_{wax-veg}$ shows an average precession cycle range of about 20‰ δD (~2.5‰ $\delta^{18}O$) (Fig. 3) with the core monsoon zone exhibiting significantly lighter values. Thus, the model and proxy records strongly disagree on the spatial relationship of precipitation isotopes across the Bay of Bengal. This disagreement may be due to the model grid size inaccurately replicating ISM circulation and rainfall patterns. Acosta & Huber (2017) find that only high-resolution models (½° or smaller spatial resolution) capture the Indo-Gangetic low-level jet responsible for bringing moisture into India from the Bay of Bengal.

5. Conclusions

Southeast Asian orbital-scale precipitation isotopes are dominated by glacial-interglacial variability, unlike the East Asian Speleothems. U1448 $\delta D_{wax-veg,}$ shows a muted glacial-interglacial variability, and lacks large obliquity and precession variability compared to U1446 $\delta D_{wax-veg}$. This suggests a relatively stable, proximal moisture source feeds the Indian Summer Monsoon branch over Andaman Islands, Irrawaddy River, and Salween River basins that is mainly impacted by differences in glacial-interglacial forcings. The monsoon circulation over Andaman Islands, Irrawaddy River, and Salween River basins is in phase with internal climate forcing from radiative forcing of greenhouse gas and ice volume, indicating it may strengthen with modern climate change.

The larger precipitation isotope interglacial variability at U1446 suggests more variable monsoon circulation over the core monsoon zone than the Andaman Islands, Irrawaddy River, and Salween River Basins (U1448). The lack of large interglacial variability in Bay of Bengal seawater isotopes suggests the precipitation isotope interglacial variability is driven by moisture source and transport- not precipitation differences. The presence of large interglacial Bay of Bengal SST variability suggest that warm Bay of Bengal SST gradients promote both proximal convective systems and distal advective moisture from the tropical western Indian Ocean into the core monsoon zone.

While precipitation isotope proxies are a useful tool because they are directly comparable to models, state of the art models currently do not accurately replicate precipitation proxy patterns in the core convective region of the ISM. The stable water isotope tracer-enabled version of the Community Earth System Model (iCESM) underestimates precipitation isotope ranges and does not replicate precipitation isotope gradients across the Bay of Bengal. High-resolution models may be able to improve the proxy-model precipitation isotope relationship.

Table 1.

Depth- age tie points

U1448 CCSFD (m)	Time (kyr)	Accumulation Rate (m/kyr)	Notes
0.01	0.56	0.134	Radiocarbon
0.99	7.90	0.071	Radiocarbon
1.74	18.53	0.107	
2.69	27.34	0.060	
5.25	70.21	0.177	
5.70	72.76	0.580	Toba Ash
6.11	73.48	0.071	
7.09	87.22	0.061	
8.61	112.11	0.056	
9.61	130.11	0.034	
9.76	134.54	0.077	
11.73	160.16	0.113	
14.10	181.16	0.069	
14.78	190.97	0.061	
15.52	203.09	0.056	
16.24	215.91	0.110	
16.61	219.29	0.061	
18.11	243.88	0.083	
19.96	266.11	0.055	
21.02	285.13	0.060	
21.57	294.26	0.032	
22.28	316.92	0.053	
23.47	339.32	0.090	
24.83	354.48	0.039	
26.39	394.67	0.049	
28.21	431.54	0.109	
29.88	446.80	0.029	
30.61	471.80	0.065	
32.13	495.34	0.035	
32.70	511.75	0.061	
33.98	532.50	0.042	
34.78	551.64	0.048	
36.06	578.33	0.063	
36.47	584.85	0.056	
36.90	592.54	0.046	
38.25	621.67	0.088	
38.65	626.19	0.049	

Table 2.

Proxy coherence and phase relationships relative to orbital parameters.

	Eccentricity (~100 kyr)		Obliquity (~41 kyr)		Precession (~23 kyr)	
Record	Coherence	Phase (°)	Coherence	Phase (°)	Coherence	Phase (°)
U1448 $\delta^{13}C_{wax}$ avg	0.72	7 ± 28	0.69	-7 ± 30	0.36	64 ± 55
U1448 δD_{wax}	0.63	-40 ± 34	0.95	-52 ± 11	0.62	-76 ± 35
U1448 $\delta D_{wax\text{-}veg}$	0.63	-44 ± 34	0.95	-54 ± 9	0.63	-74 ± 34
U1448 $\delta D_{wax\text{-}iv}$	0.44	-136 ± 48	0.56	63 ± 39	0.28	-72 ± 62
U1448 δD_{precip}	0.47	-134 ± 46	0.54	61 ± 41	0.31	-67 ± 60
U1446 $\delta D_{wax\text{-}veg}$	0.88	-9 ± 17	0.92	-58 ± 13	0.94	-78 ± 11
U1446-U1448 $\delta D_{wax\text{-}veg}$	0.82	11 ± 21	0.83	-59 ± 20	0.89	-78 ±16
Bittoo $\delta^{18}O$	0.93	-5 ± 12	0.94	-54 ± 12	0.93	-76 ± 12
XBL $\delta^{18}O$	0.81	-1 ± 21	0.75	-115 ± 26	0.99	-60 ± 5
Mulu $\delta^{18}O$	0.66	-57 ± 32	0.93	-134 ± 12	0.81	-155 ± 21
MD98-2152 $\delta D_{wax\text{-}veg}$	0.68	-62 ± 35	0.7	-117 ± 26	0.37	-152 ± 49
GHG RF	0.89	17 ± 16	0.81	-60 ± 22	0.86	-70 ± 18
Ice volume	0.91	-1 ± 14	0.97	-62 ± 8	0.93	-74 ± 12

Note. All coherence and phase calculated over the 0 to 640 ka intervals except for Bittoo (0-284 ka), XBL (0-252 ka), Mulu (0-566) and MD98-2152 (0-450).

Isotope are multiplied by -1 such that the phase of isotopic proxies reflects lighter isotopic values; calculated using ARAND software (Howell et al., 2006) with 50% lags, on timesteps from 0.05 to 2kyr.

0.55 is the confidence interval for coherency.

Values above 0.78 pass statistical test for non-zero coherency at 80% level.

Values above 0.91 pass statistical test for non-zero coherency at 95% level.

Table 3.

Proxy coherence and phase relationships relative to U1448 $\delta D_{wax-veg}$. Negative (positive) phase indicates U1448 $\delta D_{wax-veg}$ lags (leads).

	Eccentricity (~100 kyr)		Obliquity (~41 kyr)		Precession (~23 kyr)	
Record	Coherence	Phase (°)	Coherence	Phase (°)	Coherence	Phase (°)
NGHP $\delta^{18}O_{sw}$	0.95	33 ± 10	0.65	109 ± 33	0.88	72 ± 17
NGHP SST	0.66	-95 ± 32	0.76	-27 ± 26	0.92	-19 ± 14
U1446 $\delta D_{wax-veg}$	0.80	-34 ± 22	0.89	-1 ± 16	0.51	6 ± 42
Bittoo $\delta^{18}O$	0.70	-98 ± 29	0.95	0 ± 9	0.75	50 ± 26
XBL $\delta^{18}O$	0.27	102 ± 62	0.97	41 ± 7	0.83	13 ± 21
MD98-2152 $\delta D_{wax-veg}$	0.79	-18 ± 27	0.64	58 ± 34	0.88	20 ± 16
Mulu $\delta^{18}O$	0.85	-20 ± 19	0.75	71 ± 26	0.86	64 ± 18
LR04	0.80	-49 ± 22	0.93	7 ± 12	0.78	6 ± 30
GHG RF	0.78	-72 ± 24	0.79	-4 ± 29	0.60	-29 ± 36

Note. All coherence and phase calculated over the 0 to 640 ka intervals except for Bittoo (0-284 ka), XBL (0-252 ka), Mulu (0-566) and MD98-2152 (0-450).
Isotope are multiplied by -1 such that the phase of isotopic proxies reflects lighter isotopic values; calculated using ARAND software (Howell et al., 2006) with 50% lags, on timesteps from 0.05 to 2kyr.

0.55 is the confidence interval for coherency.

Values above 0.78 pass statistical test for non-zero coherency at 80% level.

Values above 0.91 pass statistical test for non-zero coherency at 95% level.

References

Acosta, R. P., & Huber, M. (2017). The neglected Indo-Gangetic Plains low-level jet and its importance for moisture transport and precipitation during the peak summer monsoon. *Geophysical Research Letters*, 44(16), 8601–8610. https://doi.org/10.1002/2017GL074440

Awasthi, N., Ray, J. S., Singh, A. K., Band, S. T., & Rai, V. K. (2014). Provenance of the Late Quaternary sediments in the Andaman Sea: Implications for monsoon variability and ocean circulation. *Geochemistry, Geophysics, Geosystems*, 15(10), 3890–3906. https://doi.org/10.1002/2014GC005462

Cai, Y., Fung, I. Y., Edwards, R. L., An, Z., Cheng, H., Lee, J. E., et al. (2015). Variability of stalagmite-inferred Indian monsoon precipitation over the past 252,000 y. *Proceedings of the National Academy of Sciences of the United States of America*, 112(10), 2954–2959. https://doi.org/10.1073/pnas.1424035112

Carolin, S. A., Cobb, K. M., Lynch-Stieglitz, J., Moerman, J. W., Partin, J. W., Lejau, S., et al. (2016). Northern Borneo stalagmite records reveal West Pacific hydroclimate across MIS 5 and 6. *Earth and Planetary Science Letters*, 439, 182–193. https://doi.org/10.1016/J.EPSL.2016.01.028

Chakraborty, S., Sinha, N., Chattopadhyay, R., Sengupta, S., Mohan, P. M., & Datye, A. (2016). Atmospheric controls on the precipitation isotopes over the Andaman Islands, Bay of Bengal. *Scientific Reports*, 6. https://doi.org/10.1038/srep19555

Cheng, H., Edwards, R. L., Sinha, A., Spötl, C., Yi, L., Chen, S., et al. (2016). The Asian monsoon over the past 640,000 years and ice age terminations. *Nature*, 534(7609), 640–646. https://doi.org/10.1038/nature18591

Chikaraishi, Y., & Naraoka, H. (2007). $\delta^{13}C$ and δD relationships among three *n*-alkyl compound classes (*n*-alkanoic acid, *n*-alkane and *n*-alkanol) of terrestrial higher plants. *Organic Geochemistry*, 38(2), 198–215. https://doi.org/10.1016/j.orggeochem.2006.10.003

Chikaraishi, Y., Naraoka, H., & Poulson, S. R. (2004). Carbon and hydrogen isotopic fractionation during lipid biosynthesis in a higher plant (Cryptomeria japonica). *Phytochemistry*, 65(3), 323–330. https://doi.org/10.1016/j.phytochem.2003.12.003

Clemens, S. C. (2022). Data report: U1448 Pleistocene Benthic Stable Isotopes, Andaman Sea. In Clemens, S.C., Kuhnt, W., LeVay, L.J., Indian Monsoon Rainfall. *Proceedings of the International Ocean Discovery Program*, (Vol. 353). College Station.

Clemens, S. C., Kuhnt, W., LeVay, L. J., Anand, P., Ando, T., Bartol, M., et al. (2016). Site U1448. *Proceedings of the International Ocean Discovery Program*, (Vol. 353). https://doi.org/10.14379/iodp.proc.353.108.2016

Clemens, S. C., Yamamoto, M., Thirumalai, K., Giosan, L., Richey, J. N., Nilsson-Kerr, K., et al. (2021). Remote and local drivers of pleistocene South Asian summer monsoon precipitation: A test for future predictions. *Science Advances*, 7(23). https://doi.org/10.1126/sciadv.abg3848

Colin, C., Turpin, L., Bertaux, J., Desprairies, A., & Kissel, C. (1999). Erosional history of the Himalayan and Burman ranges during the last two glacial–interglacial cycles. *Earth and Planetary Science Letters*, 171(4), 647–660. https://doi.org/10.1016/S0012-821X(99)00184-3

Colin, C., Turpin, L., Blamart, D., Frank, N., Kissel, C., & Duchamp, S. (2006). Evolution of weathering patterns in the Indo-Burman Ranges over the last 280 kyr: Effects of sediment provenance on 87 Sr/86 Sr ratios tracer. *Geochemistry*, *Geophysics*, *Geosystems*, 7(3), 1–16. https://doi.org/10.1029/2005GC000962

Gadgil, S. (2003). The Indian Monsoon and its Variability. *Annual Review of Earth and Planetary Sciences*, 31(1), 429–467. https://doi.org/10.1146/annurev.earth.31.100901.141251

Galy, V., Eglinton, T., France-Lanord, C., & Sylva, S. (2011). The provenance of vegetation and environmental signatures encoded in vascular plant biomarkers carried by the Ganges-Brahmaputra rivers. *Earth and Planetary Science Letters*, 304(1–2), 1–12. https://doi.org/10.1016/j.epsl.2011.02.003

Gebregiorgis, D., Hathorne, E. C., Giosan, L., Clemens, S., Nürnberg, D., & Frank, M. (2018). Southern Hemisphere forcing of South Asian monsoon precipitation over the past ~1 million years. *Nature Communications*, 9(1), 4702. https://doi.org/10.1038/s41467-018-07076-2

Hu, J., Emile-Geay, J., Nusbaumer, J., & Noone, D. (2018). Impact of Convective Activity on Precipitation δ 18 O in Isotope-Enabled General Circulation Models. *Journal of Geophysical Research: Atmospheres*, 123(23), 13,595-13,610. https://doi.org/10.1029/2018JD029187

Hu, J., Emile-Geay, J., Tabor, C., Nusbaumer, J., & Partin, J. (2019). Deciphering Oxygen Isotope Records From Chinese Speleothems With an Isotope-Enabled Climate Model. *Paleoceanography and Paleoclimatology*, 2019PA003741. https://doi.org/10.1029/2019PA003741

IAEA/WMO. (2019). Global Network of Isotopes in Precipitation. The GNIP Database. Accessible at: https://nucleus.iaea.org/wiser.

Jaglan, S., Gupta, A. K., Cheng, H., Clemens, S. C., Dutt, S., & Balaji, S. (2020). Indian summer monsoon variability during the last millennium as recorded in stalagmite from Baratang Mahadev cave, Andaman Islands. *Palaeogeography, Palaeoclimatology, Palaeoecology*, 557, 109908. https://doi.org/10.1016/J.PALAEO.2020.109908

Kathayat, G., Cheng, H., Sinha, A., Spötl, C., Edwards, R. L., Zhang, H., et al. (2016). Indian monsoon variability on millennial-orbital timescales. *Scientific Reports*, 6(1), 24374. https://doi.org/10.1038/srep24374

Laskar, A. H., Yadava, M. G., Ramesh, R., Polyak, V. J., & Asmerom, Y. (2013). A 4 kyr stalagmite oxygen isotopic record of the past Indian Summer Monsoon in the Andaman Islands. *Geochemistry, Geophysics, Geosystems*, 14(9), 3555–3566. https://doi.org/10.1002/GGGE.20203/FORMAT/PDF

Lisiecki, L. E., & Raymo, M. E. (2005). A Pliocene-Pleistocene stack of 57 globally distributed benthic $\delta^{18}O$ records. *Paleoceanography*, 20(1), 1–17. https://doi.org/10.1029/2004PA001071

McGrath, S. M., Clemens, S. C., Huang, Y., & Yamamoto, M. (2021). Greenhouse Gas and Ice Volume Drive Pleistocene Indian Summer Monsoon Precipitation Isotope Variability. *Geophysical Research Letters*, 48(4). https://doi.org/10.1029/2020GL092249

Meckler, A. N., Clarkson, M. O., Cobb, K. M., Sodemann, H., & Adkins, J. F. (2012). Interglacial hydroclimate in the tropical West Pacific through the late pleistocene. *Science*, 336(6086), 1301–1304. https://doi.org/10.1126/SCIENCE.1218340/SUPPL_FILE/MECKLER.SM.PDF

Mitchell, T. D., & Jones, P. D. (2005). An improved method of constructing a database of monthly climate observations and associated high-resolution grids. *International Journal of Climatology*, 25.

Paillard, D., Labeyrie, L., & Yiou, P. (1996). Macintosh Program performs time-series analysis. *EOS, American Geophysical Union*, 77(39), 379–379. https://doi.org/10.1029/96eo00259

Pant, V., Girishkumar, M. S., Udaya Bhaskar, T. V. S., Ravichandran, M., Papa, F., & Thangaprakash, V. P. (2015). Observed interannual variability of near-surface salinity in the Bay of Bengal. *Journal of Geophysical Research: Oceans*, 120(5), 3315–3329. https://doi.org/10.1002/2014JC010340

Pausata, F. S. R., Battisti, D. S., Nisancioglu, K. H., & Bitz, C. M. (2011). Chinese stalagmite $\delta^{18}O$ controlled by changes in the Indian monsoon during a simulated Heinrich event. *Nature Geoscience*, 4(7), 474–480. https://doi.org/10.1038/ngeo1169

Sachse, D., Billault, I., Bowen, G. J., Chikaraishi, Y., Dawson, T. E., Feakins, S. J., et al. (2012). Molecular Paleohydrology: Interpreting the Hydrogen-Isotopic Composition of Lipid

Biomarkers from Photosynthesizing Organisms. *Annu. Rev. Earth Planet. Sci*, 40(1), 221–49. https://doi.org/10.1146/annurev-earth-042711-105535
Sengupta, D., Bharath Raj, G. N., & Shenoi, S. S. C. (2006). Surface freshwater from Bay of Bengal runoff and Indonesian Throughflow in the tropical Indian Ocean. *Geophysical Research Letters*, 33(22), L22609. https://doi.org/10.1029/2006GL027573
Sinha, N., Chakraborty, S., Chattopadhyay, R., Goswami, B. N., Mohan, P. M., Parua, D. K., et al. (2019). Isotopic investigation of the moisture transport processes over the Bay of Bengal. *Journal of Hydrology*, 2, 100021. https://doi.org/10.1016/J.HYDROA.2019.100021
Tabor, C. R., Otto-Bliesner, B. L., Brady, E. C., Nusbaumer, J., Zhu, J., Erb, M. P., et al. (2018). Interpreting Precession-Driven $\delta^{18}O$ Variability in the South Asian Monsoon Region. *Journal of Geophysical Research: Atmospheres*, 123(11), 5927–5946. https://doi.org/10.1029/2018JD028424
Wei, Z., Lee, X., Liu, Z., Seeboonruang, U., Koike, M., & Yoshimura, K. (2018). Influences of large-scale convection and moisture source on monthly precipitation isotope ratios observed in Thailand, Southeast Asia. *Earth and Planetary Science Letters*, 488, 181–192. https://doi.org/10.1016/J.EPSL.2018.02.015
Windler, G., Tierney, J. E., Zhu, J., & Poulsen, C. J. (2020). Unraveling Glacial Hydroclimate in the Indo-Pacific Warm Pool: Perspectives From Water Isotopes. *Paleoceanography and Paleoclimatology*, 35(12), e2020PA003985. https://doi.org/10.1029/2020PA003985
Windler, G., Tierney, J. E., & Anchukaitis, K. J. (2021). Glacial-Interglacial Shifts Dominate Tropical Indo-Pacific Hydroclimate During the Late Pleistocene. *Geophysical Research Letters*, 48(15), e2021GL093339. https://doi.org/10.1029/2021GL093339

CHAPTER 3:

LATE PLEISTOCENE SUNDA SHELF SUBMERSION PROMOTES INDIAN SUMMER MONSOON INTERGLACIAL-GLACIAL VARIABILITY

S. M. McGrath[1], S. C. Clemens[1], Y. Huang[1]

[1] *Department of Earth, Environmental, and Planetary Sciences, Brown University, Providence, Rhode Island, USA,*

Key points

- From 640 to 250 kyr, there is relatively stable C_3/C_4 vegetation pattern across the Andaman Islands, Irrawaddy River Basin, and Salween River Basin
- After 250 ka, there is an amplification of C_4 vegetation expansion during glacial periods
- The 250 ka shift is present in vegetation records from Southeast Asia and the maritime continent but not present in the core monsoon zone of India
- Sunda shelf first was inundated similar to the modern extent over an interglacial cycle between MIS 11 and MIS 7, leading to the glacial-interglacial variability of the Indian Summer Monsoon
- Over the same period, a change in equatorial Pacific SST gradient leads to El Niño -like state; relatively warmer tropical Indian Ocean SST leads to a strong ENSO-ISM relationship

Abstract

Many studies suggest that glacial Sunda Shelf exposure causes climate feedbacks that leads to a drier Indian Summer Monsoon (ISM). However, recent discoveries show that the Sunda Shelf was permanently exposed prior to ~400 ka, and that the shelf was first inundated over an interglacial cycle sometime between MIS 11 and MIS 7. We created a continuous (0-640 kyr) orbital scale leaf wax carbon isotope ($\delta^{13}C_{wax}$) from Site U1448 (10°38.0’N, 93°00.0’E) in the Andaman Sea representing the Southeast Asian vegetation of the Andaman Islands, Irrawaddy River Basin, and Salween River Basin. A dramatic C_3/C_4 vegetation shift occurs around 250 ka, interpreted as the first large-scale shelf inundation, and leading to amplified glacial-interglacial vegetation variability due to C_4 expansion. The amplified glacial-interglacial C_3/C_4 vegetation structure since 250 ka is consistent and coherent across Southeast Asia peninsula and the Sunda Shelf. We find the glacial C_4 expansion is due to land exposure and an enhanced El Niño like climate state that promotes drier, and relatively warmer glacial periods. Post 250 ka, there is a smaller Pacific Sea surface temperature (SST) gradient due to warmer eastern equatorial Pacific SST favoring El Niño conditions. Additionally, there is relatively warmer tropical Indian Ocean glacial SST. These conditions contributed to a strong ENSO-ISM relationship during the glacial periods, weakening the ISM rainfall and enhancing C_4 vegetation variability over the last 250 kyr.

1. Introduction

Southeast Asia, including the southeast Asian peninsula and maritime continent, contain approximately 2.9 million km^2 of forests, accounting for 17% of tropical forests by area (FAO, 2022). Modern interannual variations in tropical forest are thought to be relatively modest and have adapted to grow in a relatively narrow climate range. Hence, the relative impact of climate change on tropical vegetation has the potential to be significant since predicted changes in temperature and precipitation are great compared to normal interannual variations (Chambers et al., 2012). Over Southeast Asia, most of the annual rainfall occurs during the summer monsoon season (June through September) with vegetation stability linked to the Indian Summer Monsoon (Suepa et al., 2016; Y. Zhang et al., 2016). Vegetation phenology shifts occur during prolonged dry seasons as evidenced by El Niño events (Diem et al., 2018; Suepa et al., 2016; Y. Zhang et al., 2016).

We turn to paleoclimate timescales to reconstruct C_3 and C_4 vegetation changes. Modern tropical forests are dominated by C_3 vegetation. Changes in the proportion of C_3 and C_4 vegetation will shift depending on temperature, precipitation, and CO_2 conditions (i.e. Dunlea et al., 2020; Edwards et al., 2010; Feakins et al., 2020; Huang et al., 2001, 2007; O'Mara et al., 2022; Polissar et al., 2019; Yamamoto et al., 2022). C_4 plants have an advantage over C_3 plants in low-CO2 environments (Cerling et al., 1998; Yamamoto et al., 2022). Drier and warmer conditions favor C4 grasses over C3 forests (Edwards et al., 2010).

Studies across Southeast Asia suggest glacial-interglacial vegetation variability is driven by multiple forcings. Yamamoto et al. (2022) demonstrates that C4 plant relative abundances on the mid Indian subcontinent during the past 1.46 million years correlates strongly to atmospheric pCO2. Winder et al. (2019) suggest Sumatra glacial-interglacial variability is controlled by "shelf exposure" in which a weaker walker circulation is driven by the exposure of the Sunda and Sahul shelves. Li et al. (2015) correlate El Niño

Southern Oscillation (ENSO) changes with changes in Southeast Asia vegetation recorded from South China Sea marine sediment cores.

To study vegetation variability and the forcing mechanisms that cause C_3/C_4 vegetation shifts, we create a 640-thousand-year (kyr) orbital scale record of vegetation from leaf waxes at Site U1448. Long-chain lipid *n*-alkanoic acids and *n*-alkanes are components of waxy coatings on terrestrial plant leaves that are transported by wind and water into the ocean and are preserved in sediments (G. Eglinton & Hamilton, 1967; T. I. Eglinton & Eglinton, 2008). We use two leaf wax proxies to examine the vegetation: *n*-alkanoic acids carbon isotopes and n-alkane chain lengths. Leaf wax carbon isotopes ($\delta^{13}C_{wax}$) are a proxy for C_3/C_4 plant abundance (Huang et al., 2001). The average chain length of *n*-alkanes is a proxy for environmental shifts indicated by plants synthesizing longer chain lengths due to high temperatures or dry conditions, to prevent water loss (i.e. Dodd & Afzal-Rafii, 2000; Rommerskirchen et al., 2006; Schefuß et al., 2003) or changes in the proportion of C_3 and C_4 vegetation (Badewien et al., 2015; He et al., 2016).

1.1 Site Description

IODP Expedition 353 recovered sediment from a rise in the Andaman Sea (eastern Bay of Bengal) Site U1448 (10°38.0'N, 93°00.0'E, 1091mbsl, 44km offshore) (Fig. 1) (Clemens et al., 2016). This site records hydroclimate and environmental changes from the Irrawaddy basin, Salween basin, and Andaman Islands. These areas experience over 90% of total annual rainfall during the summer monsoon season with about 500 mm of rain per month and an average temperature of 28°C (Mitchell & Jones, 2005). Terrigenous sediment supply to the Andaman Sea is dominantly from the Irrawaddy and

Salween Rivers (Colin et al., 1999, 2006) with contributions from the Indo-Burman-Arakan mountain ranges as well as the Andaman Islands (Awasthi et al., 2014). Due to Site U1448 location in the Andaman Sea, Little Andaman Island may also be a source of terrigenous materials. Although residence time could impose a lag in sedimentary systems, even in the much larger floodplain system of the Ganges-Brahmaputra catchment, leaf wax fatty acids have been shown to have short residence times (from 0.015 to 1.2 kyr) (French et al., 2018; Galy & Eglinton, 2011) that do not interfere with the timing of the forcing and response investigated here. Additionally, in previous orbital scale leaf wax studies within the Bay of Bengal, the phase relationships between the precipitation isotopes recorded from leaf waxes are in phase with the precipitation isotopes recorded in speleothems that have independent, well constrained age models (McGrath et al., 2021).

Glacial-age sea level changes may influence sediment supply to Site U1448. When sea level drops approximately 40 meters below modern sea level, the Andaman Islands become connected and the Andaman Sea connection to the Pacific Ocean is greatly reduced (Fig. 1). Additionally, as sea level drops the Irrawaddy and Salween deltas move closer to Site U1448. U1448 benthic foraminifera $\delta^{18}O$ record shows a good, continuous stratigraphy (Fig. 2) and the accumulation rates suggest a relatively stable sediment supply that mildly increases, ~1.5 times the average accumulation rate during glacial to interglacial transitions (Table 1).

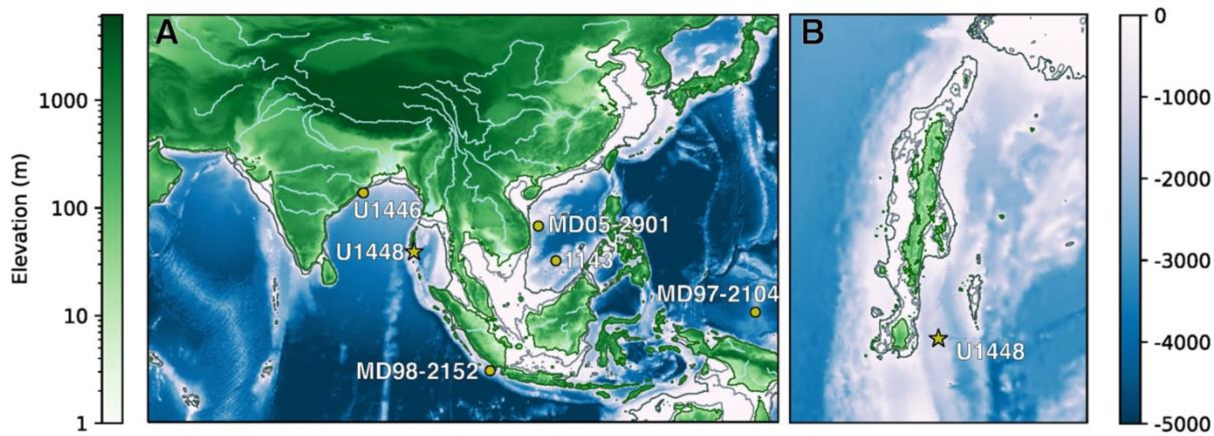

Figure 1.

Bathymetry and elevation map. Yellow star marks Site U1448. A) Yellow circles mark Site U1446, MD98-2152, ODP Site 1143, MD05-2901 and MD97-2104. ODP Site 846 (3° 5’ S, 90° 49’ W) is located off the map in the eastern equatorial Pacific Ocean cold tongue. Figure made with GeoMapApp (www.geomapapp.org) (Ryan et al., 2009) B) Close up of Andaman Island with high resolution base map data (GEBCO Compilation Group, 2021). Dark grey line indicates 120m below sea level, light gray line indicates 40m below sea level.

2. Methods

2.1 Age Model

The age model of Site U1448 is based on two radiocarbon dates, and tie points between benthic foraminifera $\delta^{18}O$ and the LR04 global $\delta^{18}O$ benthic stack (Lisiecki & Raymo, 2005) using Analyseries (Paillard et al., 1996). Two radiocarbon dates are measured on *Globigerinoides ruber* (white *sensu stricto*) picked from the 250–355 μm size fraction. Details of the U1448 benthic record are available in Clemens (2022). Correlations, tie points, and radiocarbon dates are shown in Figure 2 and Table 1.

2.2 Organic Geochemical Analyses

Lipids are extracted from 3 to 8g of freeze-dried sediment with an Accelerated Solvent Extractor 200 (Dionex) using a 9:1 mixture of dichloromethane: methanol. The extracts are dried under N2 and separated on aminopropyl silica gel flash columns eluting neutral fractions with dichloromethane (DCM): isopropanol 2:1 (v: v) and acid fractions with 4% acetic acid in diethyl ether. All flash column separations use three column volumes of each eluent. The neutral fraction containing the n-alkanes are quantified on a GC-FID using an internal standard. Acid fractions are methylated in anhydrous 5% HCl in methanol at 60°C overnight. Samples are further cleaned using silica gel flash columns: polar compounds are removed with hexane, fatty acid methyl esters (FAMEs) are eluted with DCM. The $\delta^{13}C$ of the *n*-alkanoic acids are measured using Gas Chromatography-Pyrolysis Isotope Ratio Mass Spectrometry at Brown University. Samples are run in duplicate with standards run every 4 injections. The reproducibility of the $\delta^{13}C$ measurement based on repeated analyses was better than ±0.2‰. Samples have been corrected for the methyl group added during fatty acid derivatization using the known isotopic composition of the acidified methanol used in methylation.

3. Results

3.1 Variability of $\delta^{13}C_{wax}$ *n*-Alkanoic Acids

The average leaf wax carbon isotope from alkanoic acids ($\delta^{13}C_{wax}$) value was calculated by averaging the $\delta^{13}C$ of C_{26}, C_{28}, C_{30} and C_{32}. The $\delta^{13}C$ of the C_{26}, C_{28}, C_{30} and C_{32} all exhibit the same structure (Fig. 2a). On average, the $\delta^{13}C$ values of C_{26} and C_{28} are within the range of 0.8‰ and the C_{30} and C_{32} are within the range of 1.4‰. The $\delta^{13}C$ values of C_{30} and C_{32} are on average 3.5‰ depleted compared to the $\delta^{13}C$ values of C_{26} and C_{28}, with exceptions during the last two glaciations when all $\delta^{13}C$ values converge.

The $\delta^{13}C_{wax}$ record shows enriched values during glacial periods and depleted values during interglacial periods. Spectral analysis of the $\delta^{13}C_{wax}$ indicates $\delta^{13}C_{wax}$ is dominated by the 100 kyr eccentricity cycle with no significant peaks at obliquity or precession cycles (Fig. 2b).

The glacial-interglacial variability of the $\delta^{13}C_{wax}$ shifts around 250 ka. Prior to 250 ka, the $\delta^{13}C_{wax}$ variability exhibits a muted 0.3‰ range over the glacial-interglacial cycles. After 250 ka, the $\delta^{13}C_{wax}$ variability increases to 3‰ range over the glacial-interglacial cycles. The post 250 ka amplification of glacial- interglacial variability is present in all *n*-fatty acids with C30 and C32 showing the largest glacial-interglacial range (7‰ and 9‰, respectfully).

3.2 Variability of *n*-Alkanes

The *n*-alkanes average chain length (ACL) is calculated by:

Equation 10: $ACL = \frac{27\times C_{27}+29\times C_{29}+31\times C_{31}+33\times C_{33}}{C_{27}+C_{29}+C_{31}+C_{33}}$.

The ACL $_{record}$ shows longer values during glacial periods and shorter values during interglacial periods. Spectral analysis of the ACL indicates ACL is dominated by the 100 kyr eccentricity cycle, with a minor obliquity peak and no significant peaks at precession cycles (Fig. 2b).

Prior to 250 ka, the ACL signal is very stable with an average of 30.5 and standard deviation of 0.1. After 250 ka, the ACL decreases with an average of 30.1, standard deviation of 0.3, and minimum of 29.2 (Fig. 2a). The ACL is mainly driven by the change from C31 abundance to C29 abundance and is evident in the ratio of C29/C31. Prior to 250 kyr, the ratio of C29/C31 averages 0.5 and after 250 kyr, the ratio of C29/C31 averages 0.8. Over 250 kyr, glacial periods have longer ACL, and interglacial periods have shorter ACL.

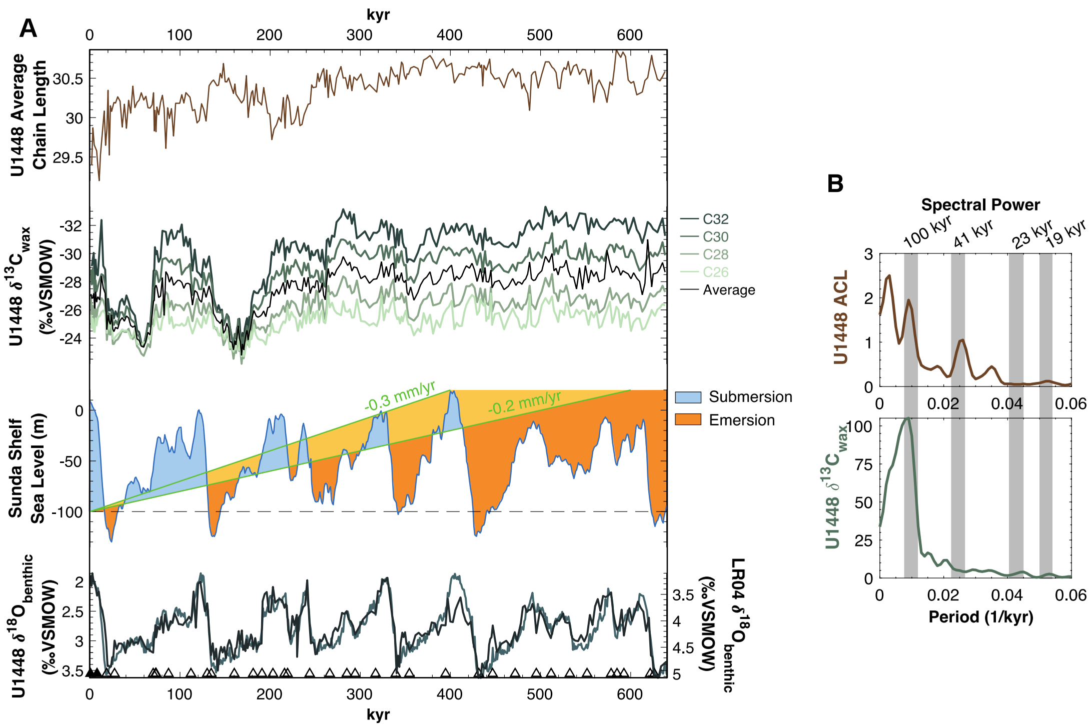

Figure 2.

A) Vegetation proxy records from U1448 and Sunda Shelf exposure. From top to bottom: *n*-alkane average chain length, $\delta^{13}C_{wax}$, global sea level curve (Spratt & Lisiecki, 2016) with black dash line indicating shelf exposure in absence of subsidence and green lines indicating Sunda Shelf subsidence rate (Sarr et al., 2019), and U1448 benthic $\delta^{18}O$ stratigraphy overlays the LR04 stack (Lisiecki & Raymo, 2005) with closed triangles indicating radiocarbon dates and open triangles indicating tie points. B) Spectral Power of U1448 *n*-alkane average chain length and average $\delta^{13}C_{wax}$ signal.

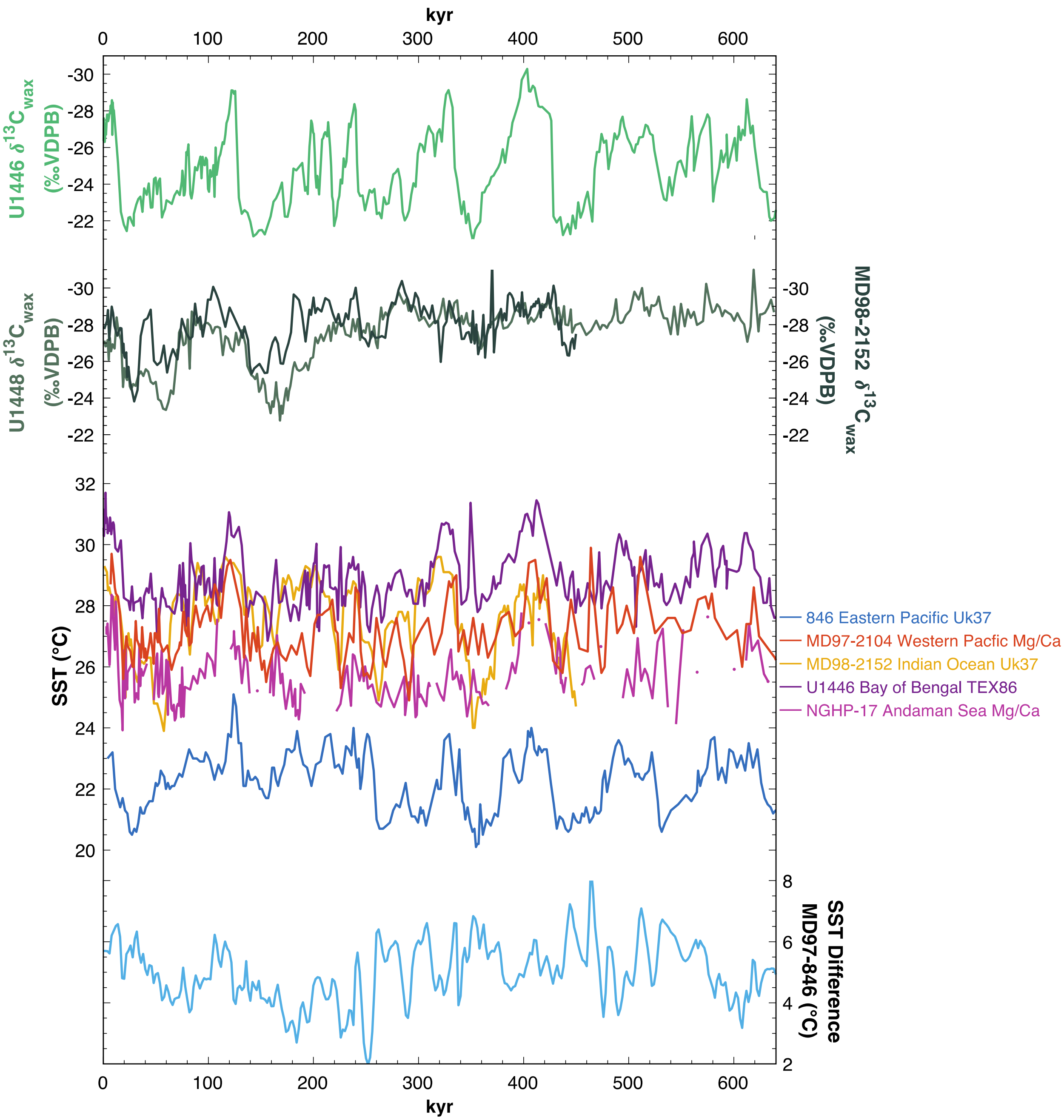

Figure 3

Proxy stack From top to bottom: Core Monsoon Zone U1446 $\delta^{13}C_{wax}$ (Yamamoto et al., 2022), southeast Asia U1448 $\delta^{13}C_{wax}$, Sumatra MD98-2152 $\delta^{13}C_{wax}$ (Windler et al., 2019), Sea surface temperature (SST) from NGHP-17 Mg/Ca (Gebregiorgis et al., 2018), U1446 Tex86 (Clemens et al., 2021), MD98-2152 Uk37 (Windler et al., 2019), MD97-2104 Mg/Ca (De Garidel-Thoron et al., 2005), and Site 846 Uk37(Liu & Herbert, 2004) and ENSO proxy SST difference from western – eastern pacific (De Garidel-Thoron et al., 2005; Liu & Herbert, 2004).

4. Discussion

4.1 Consistent Vegetation Response Across Independent Proxies

The shift at 250 kyr is present in all vegetation proxies at Site U1448, including the $\delta^{13}C_{wax}$ and ACL records (Fig 2a). All U1448 vegetation proxies suggest a very stable vegetation structure from 640-250 kyr with slight glacial-interglacial differences. The 640-250 kyr glacial-interglacial range of the U1448 $\delta^{13}C_{wax}$ records indicates mild C_4 expansion during glacials suggesting cooler and slightly drier conditions. The longer ACL during glacials suggest C_4 and grass expansion over C_3 tree as grasses in tropics have greater chain length than trees (Badewien et al., 2015; Rommerskirchen et al., 2006; Vogts et al., 2009).

After 250 kyr, the glacial-interglacial variability increases in both $\delta^{13}C_{wax}$ and ACL records. The average $\delta^{13}C_{wax}$ record glacial-interglacial variability increases by 10 times. The $\delta^{13}C_{wax}$ C30 and C32 records show enhanced amplitude of glacial-interglacial change relative to that of the $\delta^{13}C_{wax}$ C26 and C28 records. The interglacial ACL shifts by 0.5 shorter compared to the pre-250 ka values. These changes in both $\delta^{13}C_{wax}$ and ACL records support C_4 grass expansion during glacials. The shortest ACL during the Holocene suggest significantly warmer and wetter conditions compared to the previous interglacial. Overall, the U1448 vegetation proxies indicate a relatively stable C_3 dominated vegetation from 640 kyr until a shift around 250 ka followed by enhanced glacial-interglacial vegetation variability and C_4 expansion during glacial intervals.

4.2 Regional Differences in Carbon Isotope Signals

The U1448 $\delta^{13}C_{wax}$ record has a very different signal from the Site U1446 $\delta^{13}C_{wax}$ record (Fig. 3). Indian margin Site U1446 (19°5.0'N, 85°44.0'E, 1440mbsl, 70km offshore) (Fig. 1) is located near the mouth of the Mahanadi River (western Bay of Bengal). This site captures terrestrial sediment from the core monsoon zone of India including the Mahanadi River Basin and drainage basins in northern Bay of Bengal. The U1446 $\delta^{13}C_{wax}$ record shows consistent, large glacial-interglacial variability and that is primarily driven by CO_2 variability due to its unique setting (Yamamoto et al., 2022). U1446 $\delta^{13}C_{wax}$ has glacial value maxima around -22 ‰ and interglacial minima around -28‰, a range of 6‰ (Fig. 3) – double the U1448 $\delta^{13}C_{wax}$ glacial-interglacial range over 0-250 ka. Comparatively, U1448 $\delta^{13}C_{wax}$ shows a muted C_4 expansion during glacial intervals with a maximum of about -24‰ and interglacial values of about 29‰.

Evolutionary Lomb-Scargle power spectrum of U1446 $\delta^{13}C_{wax}$ (Fig. 4a) shows strong 100kyr eccentricity power throughout the record with the strongest 100kyr power between 500 to 300 ka. There is a period between 250 and 200 kyr where eccentricity power declines and obliquity and precession power increase. The evolutionary power spectrum of U1448 $\delta^{13}C_{wax}$ shows the opposite trend (Fig. 4b), with the strongest 100kyr eccentricity power after 250 kyr. Overall, U1446 and U1448 $\delta^{13}C_{wax}$ records have weak coherence relationships (Fig. 5a).

The differences in the $\delta^{13}C_{wax}$ evolution and power spectra, coupled with low coherence between them implies that vegetation from the land east of the Bay of Bengal including Andaman Islands, Irrawaddy River, and Salween River basins, have different forcing mechanisms relative the land west of the Bay of Bengal including the Core Monsoon Zone of India. The Core Monsoon Zone vegetation has a strong relationship with atmospheric carbon dioxide concentrations (Yamamoto et la., 2022). The week relationship between U1446 and U1448 $\delta^{13}C_{wax}$ suggest over orbital timescale, vegetation in the Andaman Islands, Irrawaddy and Salween River basins are not very sensitive to atmospheric carbon dioxide concentrations changes.

4.3 Amplification of the Glacial-Interglacial Signal

While the two Bay of Bengal based $\delta^{13}C_{wax}$ records show different signals, U1448 $\delta^{13}C_{wax}$ has a very similar structure to the tropical Indian Ocean MD98-2152 $\delta^{13}C_{wax}$ record (Fig. 3). MD98-2152 (6.33 S, 103.88 E, 1796 mbsl), is located off the southwest margin of the Sunda Shelf in the southern Sumatran margin (Fig. 1). This site captures the terrestrial signal from the Sumatra and Java Islands. The MD98-2152 $\delta^{13}C_{wax}$ record shows increasing glacial variability over the last two glacial periods (Windler et al., 2019) with less glacial-interglacial variability between 450 ka to 250 ka, very similar to U1448 $\delta^{13}C_{wax}$ record (Fig. 3). This similar structure is evident within the evolutionary power spectra of the records. Both U1448 and MD98-2152 $\delta^{13}C_{wax}$ records show 100kyr eccentricity power that is amplified after 250 ka (Fig. 4 b, c). These two records are highly coherent (Fig. 5b).

Windler et al., 2019 interpret the amplification in the $\delta^{13}C_{wax}$ glacial variability as resulting from global sea level (Waelbroeck et al., 2002) changes influencing Sunda Shelf exposure during the last two glacial periods. If global sea level and Sunda Shelf exposure are the primary driving factors for $\delta^{13}C_{wax}$ glacial variability at U1448, then according to the global sea level curves (Spratt & Lisiecki, 2016), there should be large $\delta^{13}C_{wax}$ glacial variability during marine isotope stage (MIS) 12 (478-424 kyr) and MIS 16 (676-621 kyr) as well. The lack of large glacial $\delta^{13}C_{wax}$ variability at these times in the U1448 record indicates that global sea level is not the dominant driving factor for vegetation change.

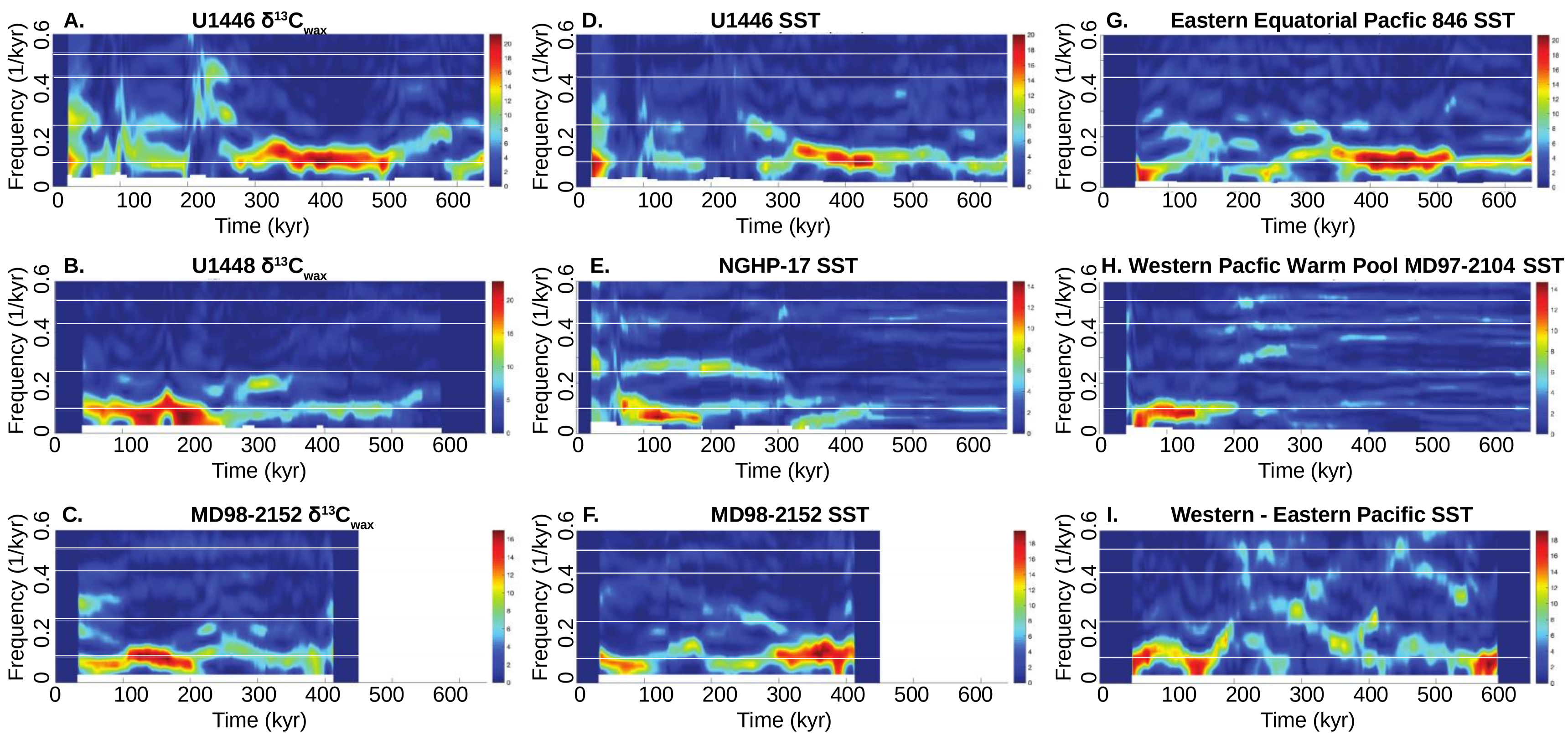

Figure 4

Evolutionary Lombe-Scargle power spectrums: A) U1446 $\delta^{13}C_{wax}$, B) U1448 $\delta^{13}C_{wax}$, C) MD98-2152 $\delta^{13}C_{wax}$, D) U1446 SST, E) NGHP-17 SST, F) MD98-2152, G) ODP Site 846 SST, H) MD97-2105 SST, I) the difference of western Pacific warm pool site Md98-2105 minus eastern Pacific ODP Site 846 SST. White lines at 0.01 indicate 100kyr eccentricity, 0.024 indicate 41kyr obliquity, 0.043 and 0.052 indicate 23 and 19 kyr precession frequencies.

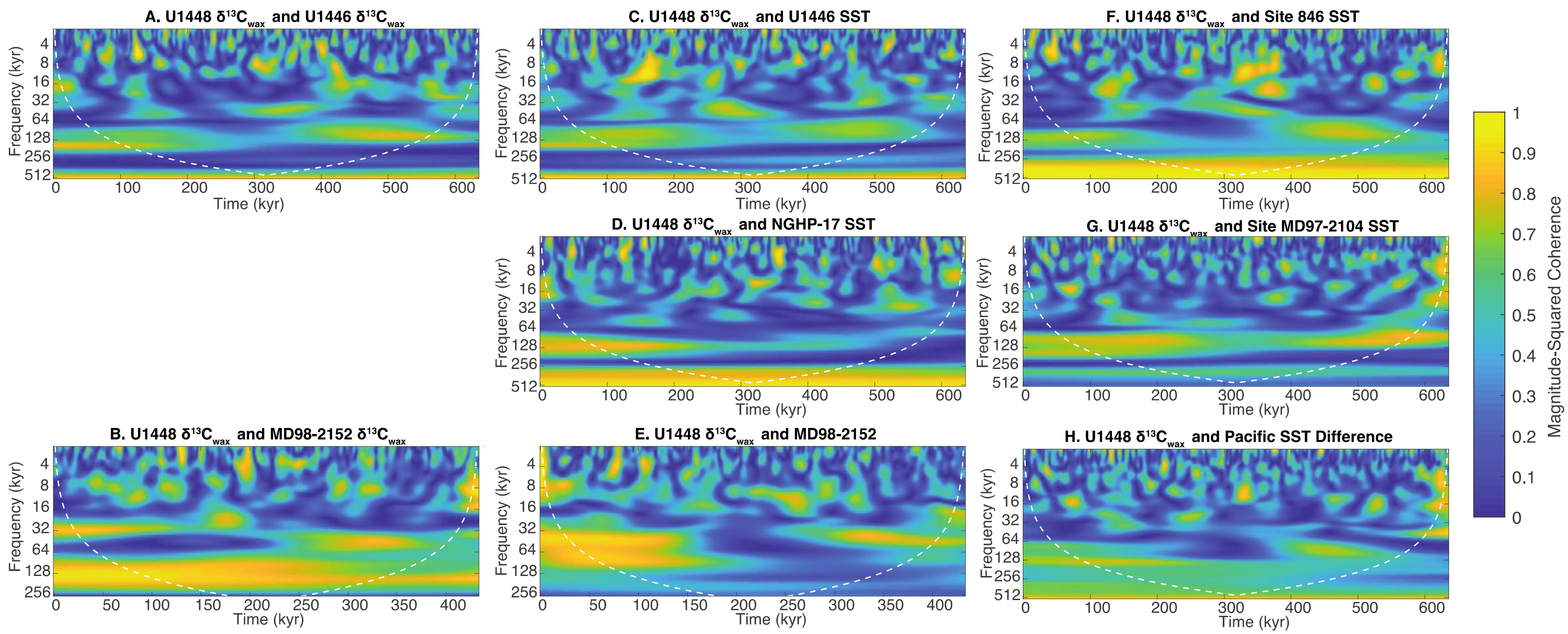

Figure 5

Wavelet Coherence: U1448 $\delta^{13}C_{wax\ vs}$, A) U1446 $\delta^{13}C_{wax}$, B) MD98-2152 $\delta^{13}C_{wax}$, C) U1446 SST, D) NGHP-17 SST, E) MD98-2152, F) ODP Site 846 SST, G) MD97-2105 SST, H) the difference of western Pacific warm pool site Md98-2105 minus eastern Pacific ODP Site 846 SST.

4.4 Sunda Shelf Subsiding

The Sunda Shelf is subsidising and as late at ~400 ka, the shelf was permanently exposed (Sarr et al., 2019) (Fig. 2). Sarr er al. (2019) calculates the long-term subsidence rate to be between 0.2 mm per year and 0.3 mm per year, which implies the first submersion of the Sunda Shelf to be during an interglacial period between 410 ka in MIS 11 and 240 ka in MIS 7. This submersion of the shelf would have perturbed the vegetation, flooding and depositing marine sediment over the shelf during interglacial intervals, and allowed for larger C_4 expansion on the exposed shelf during the following glacial intervals.

A subsidence rate between 0.2mm and 0.3 mm per year is consistent with the large vegetation shifts at 250 ka. The U1448 $\delta^{13}C_{wax}$ exhibits a minor 2‰ shift in C_3 and C_4 proportions at 360 ka, during MIS 10, the glacial interval after the estimated first, brief submersion of the Sunda Shelf. After 250 ka, there are wholescale shifts in in C_3 and C_4 proportions, corresponding to the larger and longer submersion during MIS 9. From 250 ka onwards, the amplification of the glacial-interglacial vegetation signal due to the increase in amplitude of the submersion of the shelf. These results point to a long-term subsidence rate closer to 0.3mmm/yr.

Model results of Southeast Asia during the last glacial maximum show a mixture of deciduous tropical trees and C_4 grass (Di Nezio et al., 2016) and aligning with the C_4 expansion evident in U1448 and MD98-2152 $\delta^{13}C_{wax}$ records. The glacial C_4 expansion is caused by both land exposure and climate feedbacks from the shelf exposure. In the following sections we show that paleoclimate proxies align with model results; the change in Sunda Shelf exposure influences Indian Ocean SST and walker circulation resulting in changes in monsoon precipitation (DiNezio et al., 2018; Dinezio & Tierney, 2013; Di Nezio et al., 2016).

4.5 Comparison of Vegetation with Sea Surface Temperature Records

All three sites have local sea surface temperature (SST) records and show glacial-interglacial trends that are similar to the local $\delta^{13}C_{wax}$ signal (Table 2, Fig. 3). SST derived from $\delta^{18}O$ and Mg/Ca analyses from NGHP-17 (Gebregiorgis et al., 2018) is located near Site U1448. The NGHP-17 SST evolutionary power spectrum shows an amplification in the 100kyr eccentricity cycle after 250 ka (Fig. 4) and is highly coherent with U1448 $\delta^{13}C_{wax}$ (Fig. 5). The MD98-2152 SST derived from Uk37' analysis (Windler et al., 2019) shows strong 100 kyr power throughout the record, however, the strongest power is prior to 250 ka. There is low coherence between MD98-2152 $\delta^{13}C_{wax}$ and SST; however, there is coherence between U1448 $\delta^{13}C_{wax}$ and MD98-2152 SST around the obliquity and eccentricity bands post 250 ka (Fig. 5). U1446 SST is derived from TEX86 (Clemens et al., 2021) and shows a very similar evolutionary power spectrum compared to U1446 $\delta^{13}C_{wax}$ (Fig. 4); the two records have high coherence across the records. U1448 $\delta^{13}C_{wax}$ has weak coherence with U1446 SST (Fig. 5).

Altogether, these relationships indicate that Indian Ocean SST is intimately coupled with the local C_3/C_4 vegetation structure. Bay of Bengal SSTs have strong relationships with the local vegetation structures, with eastern Bay of Bengal SSTs related to core monsoon zone vegetation change and Andaman Sea SSTs related to local Southeast Asia peninsula vegetation change. The local SST relationship is weaker in the tropical Indian Ocean at site MD98-2152 with the local Sumatra and Java Island vegetation change. Post-250 ka the shelf submersion and exposure cycles cause larger glacial-interglacial variability of tropical Indian Ocean SSTs, leading to warmer glacial and interglacial SSTs at Site U1448 and MD98-2152 compared to pre-250ka glacial and interglacial SSTs (Table 2). Additionally, Post-250 ka, interglacial-glacial north to south SST difference aligns with model results that show the largest glacial cooling at the equatorial eastern Indian ocean (MD98-2152) and the smallest glacial cooling in the northern Bay of Bengal (U1446) (Table 2) although the models overestimate the degree of cooling (DiNezio et al., 2018). This cooling of the equatorial eastern Indian ocean weakens the Indian Ocean walker circulation leading to drier conditions over Southeast Asia and the Maritime continent (DiNezio et al., 2018; Dinezio & Tierney, 2013; Di Nezio et al., 2016).

4.6 Relationship between Vegetation and ENSO

There is a very strong relationship between Pacific Ocean SSTs and the 250 ka amplification of the glacial-interglacial variability of the $\delta^{13}C_{wax}$ at Site U1448 and MD98-2152. The Western Pacific Warm Pool (WPWP) site MD97-2104 (De Garidel-Thoron et al., 2005) shows large glacial-interglacial SST variability that is amplified over the last 250 kyr (Fig 4). There is a high coherence between the $\delta^{13}C_{wax}$ records at Site U1448, MD98-2152 and MD97-2104 SST records over the last 250 kyr. In the eastern equatorial Pacific cold tongue there is also a change in glacial-interglacial SST variability over the last two glacial periods. This is seen at both ODP Site 846 (Liu & Herbert, 2004) and Site 1239 (Etourneau et al., 2010). The evolutionary power spectrum of the ODP Site 846 SST shows strong 100 kyr eccentricity power between 640 and 250 ka (Fig. 4), with weaker power from 250 ka to present.

The difference between western Pacific Site MD97-2104 SST and eastern Pacific ODP Site 846 SST has been used as an El Niño Southern Oscillation (ENSO) proxy (De Garidel-Thoron et al., 2005) with a larger SST difference representing La Nina like conditions, and a smaller SST difference representing El Niño like conditions. Both $\delta^{13}C_{wax}$ from U1448 and MD98-2152 show strong similarities in the evolutionary power spectra with the ENSO SST proxy (Fig. 4) and have high coherence at the 100 kyr eccentricity band that increases over the last 250 kyr (Fig. 5).

Previous studies from sites in the South China Sea that integrate the terrestrial changes in Vietnam, the Pearl River, Red River and Mekong River have noted this change in ENSO and related it to associated changes in vegetation (Li et al., 2015) and runoff (Y. G. Zhang et al., 2007) around 250 ka. Zhang et al. (2007) found a decline in runoff around 240 ka at ODP Site 1143 (southern South China Sea) which they linked with changes in the Pacific Ocean SST gradient and ENSO-like conditions. Li et al. (2015) created an *n*-alkane record from site MD05-2901 (South China Sea) showing reduced glacial-interglacial variability of ACL around 270 ka, inferred to reflect reduced humidity during glacial periods. While the ACL records at Site U1448 and MD05-2901 show different shifts in variability, the timing and direction of change at both sites support drier glacial conditions fostered from an El Niño -like state.

The shift in the SST difference between the western Pacific and eastern Pacific indicates a smaller SST gradient post 250 ka that favors El Niño -like conditions. This shift is driven by the eastern equatorial Pacific cold tongue temperatures (Etourneau et al., 2010; Liu & Herbert, 2004) that remain relatively warmer during glacials over the last 250 kyr. From discrete time interval reconstructions of El Niño amplitude over the last

285 kyr, Rustic et al. 2020 find there are more discrete intervals of enhanced El Niño amplitude than weakened El Niño amplitude. The enhanced El Niño amplitude is attributed to a shoaling of the Pacific thermocline (Rustic et al., 2020). The shift in eastern equatorial Pacific cold tongue SSTs aligns with the subsidence of the Sunda Shelf, suggesting that the shift to a El Niño -like conditions is related to glacial-interglacial variability of the shelf exposure.

In the modern, El Niño is related with weaker Indian Summer Monson causing warmer and drier summer monsoon conditions through the displacement of the Walker circulation (Sikka, 1980; Webster & Yang, 1992). Over the recent decades, the ENSO-ISM relationship has waxed and waned over Indian subcontinent (Kumar et al., 1999; Yu et al., 2021), however, there has consistently been a strong negative correlation between ENSO and rainfall over the southeast Asian peninsula and maritime continent (B. Wang et al., 2020). This strong ENSO-monsoon-vegetation relationship over Southeast Asian peninsula and maritime continent is apparent in the paleoclimate records. While the core monsoon zone vegetation proxies from U1446 lack the 250ka vegetation shift, the Southeast Asian peninsula vegetation proxies from U1448 and the maritime continent vegetation proxies from MD98-2152 both show a strong ENSO-monsoon-vegetation relationship.

Additionally, in the modern, there is a significant relationship between the SST of the tropical Indian Ocean and the strength of the ENSO-ISM relationship. The warmer the SST of the tropical Indian Ocean, the stronger the ENSO-ISM relationship is, resulting in drier, warmer monsoon conditions (Yu et al., 2021). This stronger relationship between the tropical Indian Ocean SST, ENSO, and the ISM can be seen during the last two glacial periods. The last two glacial periods SST are relatively warmer than the previous glacial SST at Andaman Sea site NGHP-17 and tropical Indian Ocean site MD98-2152. Precipitation and runoff ($\delta^{18}O_{sw}$, Rb/Ca) proxies from the Bay of Bengal Site U1446 (Clemens et al., 2021) show relatively larger 100 kyr cycle variability since the Sunda Shelf has been submerged, especially over the last 2 glacial-interglacial cycles that indicate weaker ISM rainfall conditions during glacials. This suggests the El Niño -like conditions contributed to weakening ISM rainfall as well as altering the C3/C4 vegetation structure.

The result is that the ISM is both weakened through weaker glacial Walker circulation due to both the glacial Indian Ocean SST response (described in section 4.4) and enhanced El-Nino like conditions. The weakened walker circulation promotes drier ISM aiding in the expansion of C_4 vegetation during glacial periods.

5. Conclusions

There is a shift in the vegetation structure of Southeast Asia around 250 ka that aligns with the subsidence in the Sunda Shelf. Post 250 ka, Site U1448 and MD98-2152 $\delta^{13}C_{wax}$ records show amplification of the glacial-interglacial cycles. The Sunda Shelf submersion enhances C_4 expansion during glacials through both land exposure and climate feedbacks. Land exposure and glacial SSTs drive weakening of the Indian ocean walker circulation. The Indian Ocean walker circulation is further weakened by a shift in ENSO mean state to El-Niño conditions, due to the warming of glacial Eastern Equatorial Pacific SST. The relatively warmer glacial SST in the tropical Indian Ocean enhanced the ENSO-ISM relationship creating weaker glacial monsoons. The weaker monsoon system led to drier conditions that favor C_4 vegetation expansion during glacials over Southeast Asia and the

Sunda shelf. These results indicate that the southeast Asian peninsula vegetation is sensitive to a strengthened ISM-ENSO relationship. The risk of intense El Niño with modern climate change leading to drier, warmer monsoon seasons will threaten the tropical forest vegetation and favor the expansion of C_4 plants in the region.

Table 1

Depth- age tie points

U1448 CCSFD (m)	Time (kyr)	Accumulation Rate (m/kyr)	Notes
0.01	0.56	0.134	Radiocarbon
0.99	7.90	0.071	Radiocarbon
1.74	18.53	0.107	
2.69	27.34	0.060	
5.25	70.21	0.177	
5.70	72.76	0.580	Toba Ash
6.11	73.48	0.071	
7.09	87.22	0.061	
8.61	112.11	0.056	
9.61	130.11	0.034	
9.76	134.54	0.077	
11.73	160.16	0.113	
14.10	181.16	0.069	
14.78	190.97	0.061	
15.52	203.09	0.056	
16.24	215.91	0.110	
16.61	219.29	0.061	
18.11	243.88	0.083	
19.96	266.11	0.055	
21.02	285.13	0.060	
21.57	294.26	0.032	
22.28	316.92	0.053	
23.47	339.32	0.090	
24.83	354.48	0.039	
26.39	394.67	0.049	
28.21	431.54	0.109	
29.88	446.80	0.029	
30.61	471.80	0.065	
32.13	495.34	0.035	
32.70	511.75	0.061	
33.98	532.50	0.042	
34.78	551.64	0.048	
36.06	578.33	0.063	
36.47	584.85	0.056	
36.90	592.54	0.046	
38.25	621.67	0.088	
38.65	626.19	0.049	

Table 2

Table 2. Glacial Interglacial averages, and variability pre/post 250 kyr

Proxy	Pre- 250 ka					Post-250 ka					Summary of post 250 ka changes
	Interglacial		Glacial		Interglacial-glacial difference	Interglacial		Glacial		Interglacial-glacial difference	
	average	standard deviation	average	standard deviation		average	standard deviation	average	standard deviation		
U1448 $\delta^{13}C_{wax}$ (permil)	-28.6	0.5	-28.3	0.7	-0.3	-27.4	0.7	-24.7	0.9	-2.7	larger G/IG variability
MD98-2152 $\delta^{13}C_{wax}$ (permil)	-28.8	0.7	-28.0	1.2	-0.8	-28.5	0.8	-26.7	1.3	-1.9	larger G/IG variability
U1446 $\delta^{13}C_{wax}$ (permil)	-26.5	3.0	-23.4	1.4	-3.1	-25.8	1.7	-22.8	1.1	-3.0	no change
NGHP-17 SST (Mg/Ca) (°C)	25.4	4.3	25.0	3.4	0.4	26.2	1.1	25.5	0.8	0.7	larger G/IG variability, warmer SSTs
MD98-2152 SST (Uk37) (°C)	27.7	4.2	26.3	1.1	1.4	28.3	0.9	27.2	1.3	1.2	warmer SSTs
U1446 SST (TEX86) (°C)	29.7	0.8	28.5	0.6	1.2	29.2	1.0	28.3	0.7	0.9	no change

References

Awasthi, N., Ray, J. S., Singh, A. K., Band, S. T., & Rai, V. K. (2014). Provenance of the Late Quaternary sediments in the Andaman Sea: Implications for monsoon variability and ocean circulation. *Geochemistry, Geophysics, Geosystems,* 15(10), 3890–3906. https://doi.org/10.1002/2014GC005462

Badewien, T., Vogts, A., & Rullkötter, J. (2015). n-Alkane distribution and carbon stable isotope composition in leaf waxes of C_3 and C4 plants from Angola. *Organic Geochemistry*, 89–90, 71–79. https://doi.org/10.1016/J.ORGGEOCHEM.2015.09.002

Cerling, T. E., Ehleringer, J. R., & Harris, J. M. (1998). Carbon dioxide starvation, the development of C_4 ecosystems, and mammalian evolution. *Philosophical Transactions of the Royal Society of London. Series B: Biological Sciences,* 353(1365), 159–171. https://doi.org/10.1098/RSTB.1998.0198

Chambers, J., Fisher, R., Hall, J., Norby, R. J., Wofsy, S. C., & Stover, D. (2012). *Research Priorities for Tropical Ecosystems Under Climate Change Workshop Report*, June 4-5, 2012. https://doi.org/10.2172/1471591

Clemens, S.C., Kuhnt, W., LeVay, L. J., Anand, P., Ando, T., Bartol, M., et al. (2016). Site U1448. *Proceedings of the International Ocean Discovery Program,* (Vol. 353). https://doi.org/10.14379/iodp.proc.353.108.2016

Clemens, Steven C. (2022). Data report: U1448 Pleistocene Benthic Stable Isotopes, Andaman Sea. In Clemens, S.C., Kuhnt, W., LeVay, L.J., Indian Monsoon Rainfall. *Proceedings of the International Ocean Discovery Program,* (Vol. 353). College Station.

Clemens, Steven C., Yamamoto, M., Thirumalai, K., Giosan, L., Richey, J. N., Nilsson-Kerr, K., et al. (2021). Remote and local drivers of pleistocene South Asian summer monsoon precipitation: A test for future predictions. *Science Advances*, 7(23). https://doi.org/10.1126/sciadv.abg3848

Clemens, Steven C, Yamamoto, M., Thirumalai, K., Giosan, L., Richey, J. N., Nilsson-Kerr, K., et al. (2021). Remote and local drivers of pleistocene South Asian summer monsoon precipitation: A test for future predictions. *Science Advances*, 7(23). https://doi.org/10.1126/sciadv.abg3848

Colin, C., Turpin, L., Bertaux, J., Desprairies, A., & Kissel, C. (1999). Erosional history of the Himalayan and Burman ranges during the last two glacial–interglacial cycles. *Earth and Planetary Science Letters*, 171(4), 647–660. https://doi.org/10.1016/S0012-821X(99)00184-3

Colin, C., Turpin, L., Blamart, D., Frank, N., Kissel, C., & Duchamp, S. (2006). Evolution of weathering patterns in the Indo-Burman Ranges over the last 280 kyr: Effects of sediment provenance on $^{87}Sr/^{86}Sr$ ratios tracer. *Geochemistry, Geophysics, Geosystems*, 7(3), 1–16. https://doi.org/10.1029/2005GC000962

Diem, P. K., Pimple, U., Sitthi, A., Varnakovida, P., Tanaka, K., Pungkul, S., et al. (2018). Shifts in growing season of tropical deciduous forests as driven by El Niño and La Niña during 2001-2016. *Forests*, 9(8), 448. https://doi.org/10.3390/f9080448

Dinezio, P. N., & Tierney, J. E. (2013). The effect of sea level on glacial Indo-Pacific climate. *Nature* Geoscience, 6(6), 485–491. https://doi.org/10.1038/ngeo1823

DiNezio, P. N., Tierney, J. E., Otto-Bliesner, B. L., Timmermann, A., Bhattacharya, T., Rosenbloom, N., & Brady, E. (2018). Glacial changes in tropical climate amplified by the Indian Ocean. *Science Advances*, 4(12). https://doi.org/10.1126/SCIADV.AAT9658/SUPPL_FILE/AAT9658_SM.PDF

Dodd, R. S., & Afzal-Rafii, Z. (2000). Habitat-related adaptive properties of plant cuticular lipids. *Evolution*, 54(4), 1438. https://doi.org/10.1554/0014-3820(2000)054[1438:hrapop]2.0.co;2

Dunlea, A. G., Giosan, L., & Huang, Y. (2020). Pliocene expansion of C_4 vegetation in the Core Monsoon Zone on the Indian Peninsula. *Climate of the Past*, 16(6), 2533–2546. https://doi.org/10.5194/CP-16-2533-2020

Edwards, CP, O., CA, S., SA, S., WJ, B., PA, C., et al. (2010). The origins of C_4 grasslands: integrating evolutionary and ecosystem science. *Science*, 328, 587–59. https://doi.org/10.1126/science.1177216

Eglinton, G., & Hamilton, R. J. (1967). Leaf epicuticular waxes. *Science*, 156(3780), 1322–1335. https://doi.org/10.1126/SCIENCE.156.3780.1322

Eglinton, T. I., & Eglinton, G. (2008). Molecular proxies for paleoclimatology. *Earth and Planetary Science Letters*, 275(1–2), 1–16. https://doi.org/10.1016/J.EPSL.2008.07.012

Etourneau, J., Schneider, R., Blanz, T., & Martinez, P. (2010). Intensification of the Walker and Hadley atmospheric circulations during the Pliocene–Pleistocene climate transition. *Earth and Planetary Science Letters*, 297(1–2), 103–110. https://doi.org/10.1016/J.EPSL.2010.06.010

FAO. (2022). *Global Forest Resources Assessment 2020: Main report*. Rome. https://doi.org/10.4060/ca9825en

Feakins, S. J., Liddy, H. M., Tauxe, L., Galy, V., Feng, X., Tierney, J. E., et al. (2020). Miocene C_4 Grassland Expansion as Recorded by the Indus Fan. *Paleoceanography and Paleoclimatology*, 35(6). https://doi.org/10.1029/2020PA003856

De Garidel-Thoron, T., Rosenthal, Y., Bassinot, F., & Beaufort, L. (2005). Stable sea surface temperatures in the western Pacific warm pool over the past 1.75 million years. *Nature*, 433(7023), 294–298. https://doi.org/10.1038/nature03189

GEBCO Compilation Group. (2021). GEBCO 2021 Grid. https://doi.org/10.5285/c6612cbe-50b3-0cff-e053-6c86abc09f8f

Gebregiorgis, D., Hathorne, E. C., Giosan, L., Clemens, S., Nürnberg, D., & Frank, M. (2018). Southern Hemisphere forcing of South Asian monsoon precipitation over the past ~1 million years. *Nature Communications*, 9(1), 4702. https://doi.org/10.1038/s41467-018-07076-2

He, Y., Gao, J., Guo, N., & Guo, Y. (2016). Variations of Leaf Cuticular Waxes Among C_3 and C_4 Gramineae Herbs. *Chemistry & Biodiversity*, 13(11), 1460–1468. https://doi.org/10.1002/CBDV.201600030

Huang, Y., Street-Perrott, F. A., Metcalfe, S. E., Brenner, M., Moreland, M., & Freeman, K. H. (2001). Climate change as the dominant control on glacial-interglacial variations in C_3 and C_4 plant abundance. *Science*, 293(5535), 1647–1651. https://doi.org/10.1126/SCIENCE.1060143

Huang, Y., Clemens, S. C., Liu, W., Wang, Y., & Prell, W. L. (2007). Large scale hydrological change drove the late Miocene C_4 plant expansion in the Himalayan foreland Arabian Peninsula. *Geology*, 35(6), 531–534. https://doi.org/10.1130/G23666A.1

Kumar, K. K., Rajagopalan, B., & Cane, M. A. (1999). On the weakening relationship between the Indian monsoon and ENSO. *Science*, 284(5423), 2156–2159. https://doi.org/10.1126/SCIENCE.284.5423.2156

Li, L., Li, Q., Li, J., Wang, H., Dong, L., Huang, Y., & Wang, P. (2015). A hydroclimate regime shift around 270 ka in the western tropical Pacific inferred from a late Quaternary n-alkane chain-length record. *Palaeogeography, Palaeoclimatology, Palaeoecology*, 427, 79–88. https://doi.org/10.1016/J.PALAEO.2015.03.025

Lisiecki, L. E., & Raymo, M. E. (2005). A Pliocene-Pleistocene stack of 57 globally distributed benthic $\delta^{18}O$ records. *Paleoceanography*, 20(1), 1–17. https://doi.org/10.1029/2004PA001071

Liu, Z., & Herbert, T. O. (2004). High-latitude influence on the eastern equatorial Pacific climate in the early Pleistocene epoch. *Nature*, 427(6976), 720–723. https://doi.org/10.1038/nature02338

McGrath, S. M., Clemens, S. C., Huang, Y., & Yamamoto, M. (2021). Greenhouse Gas and Ice Volume Drive Pleistocene Indian Summer Monsoon Precipitation Isotope Variability. *Geophysical Research Letters*, 48(4). https://doi.org/10.1029/2020GL092249

Mitchell, T. D., & Jones, P. D. (2005). An improved method of constructing a database of monthly climate observations and associated high-resolution grids. *International Journal of Climatology*, 25.
Di Nezio, P. N., Timmermann, A., Tierney, J. E., Jin, F. F., Otto-Bliesner, B., Rosenbloom, N., et al. (2016). The climate response of the Indo-Pacific warm pool to glacial sea level. *Paleoceanography*, 31(6), 866–894. https://doi.org/10.1002/2015PA002890
O'Mara, N. A., Skonieczny, C., McGee, D., Winckler, G., Bory, A. J.-M., Bradtmiller, L. I., et al. (2022). Pleistocene drivers of Northwest African hydroclimate and vegetation. *Nature Communications* 2022 13:1, 13(1), 1–11. https://doi.org/10.1038/s41467-022-31120-x
Paillard, D., Labeyrie, L., & Yiou, P. (1996). Macintosh Program performs time-series analysis. *EOS, American Geophysical Union*, 77(39), 379–379. https://doi.org/10.1029/96eo00259
Polissar, P. J., Rose, C., Uno, K. T., Phelps, S. R., & deMenocal, P. (2019). Synchronous rise of African C_4 ecosystems 10 million years ago in the absence of aridification. *Nature Geoscience* 2019 12:8, 12(8), 657–660. https://doi.org/10.1038/s41561-019-0399-2
Rommerskirchen, F., Plader, A., Eglinton, G., Chikaraishi, Y., & Rullkötter, J. (2006). Chemotaxonomic significance of distribution and stable carbon isotopic composition of long-chain alkanes and alkan-1-ols in C_4 grass waxes. *Organic Geochemistry*, 37(10), 1303–1332. https://doi.org/10.1016/J.ORGGEOCHEM.2005.12.013
Rustic, G. T., Polissar, P. J., Ravelo, A. C., & White, S. M. (2020). Modulation of late Pleistocene ENSO strength by the tropical Pacific thermocline. *Nature Communications* 2020 11:1, 11(1), 1–11. https://doi.org/10.1038/s41467-020-19161-6
Ryan, W. B. F., Carbotte, S. M., Coplan, J. O., O'hara, S., Melkonian, A., Arko, R., et al. (2009). Global Multi-Resolution Topography synthesis. *Geochemistry, Geophysics, Geosystems*, 3(10). https://doi.org/10.1029/2008GC002332
Sarr, A., Husson, L., Sepulchre, P., Pastier, A., Pedoja, K., Elliot, M., et al. (2019). Subsiding Sundaland. Geological Society of America | GEOLOGY, 47, 119–122. https://doi.org/10.1130/G45629.1
Schefuß, E., Ratmeyer, V., Stuut, J. B. W., Jansen, J. H. F., & Sinninghe Damsté, J. S. (2003). Carbon isotope analyses of n-alkanes in dust from the lower atmosphere over the central eastern Atlantic. *Geochimica et Cosmochimica Acta*, 67(10), 1757–1767. https://doi.org/10.1016/S0016-7037(02)01414-X
Sikka, D. R. (1980). Some aspects of the large scale fluctuations of summer monsoon rainfall over India in relation to fluctuations in the planetary and regional scale circulation parameters. *Proc. Indian Acad. Sci. (Earth Planet. Sci.)* (89), 179–195. https://doi.org/10.1007/BF02913749
Spratt, R. M., & Lisiecki, L. E. (2016). A Late Pleistocene sea level stack. *Clim. Past*, 12, 1079–1092. https://doi.org/10.5194/cp-12-1079-2016
Suepa, T., Qi, J., Lawawirojwong, S., & Messina, J. P. (2016). Understanding spatio-temporal variation of vegetation phenology and rainfall seasonality in the monsoon Southeast Asia. *Environmental Research*, 147, 621–629. https://doi.org/10.1016/J.ENVRES.2016.02.005
Vogts, A., Moossen, H., Rommerskirchen, F., & Rullkötter, J. (2009). Distribution patterns and stable carbon isotopic composition of alkanes and alkan-1-ols from plant waxes of African rain forest and savanna C_3 species. *Organic Geochemistry*, 40(10), 1037–1054. https://doi.org/10.1016/J.ORGGEOCHEM.2009.07.011
Waelbroeck, C., Labeyrie, L., Michel, E., Duplessy, J. C., McManus, J. F., Lambeck, K., et al. (2002). Sea-level and deep water temperature changes derived from benthic foraminifera isotopic records. *Quaternary Science Reviews*, 21(1–3), 295–305. https://doi.org/10.1016/S0277-3791(01)00101-9
Wang, B., Luo, X., & Liu, J. (2020). How robust is the Asian precipitation-ENSO relationship during the industrial warming period (1901-2017)? *Journal of Climate*, 33(7), 2779–2792. https://doi.org/10.1175/JCLI-D-19-0630.1

Webster, P. J., & Yang, S. (1992). Monsoon and Enso: Selectively Interactive Systems. *Quarterly Journal of the Royal Meteorological Society*, 118(507), 877–926. https://doi.org/10.1002/QJ.49711850705

Windler, G., Tierney, J. E., DiNezio, P. N., Gibson, K., & Thunell, R. (2019). Shelf exposure influence on Indo-Pacific Warm Pool climate for the last 450,000 years. *Earth and Planetary Science Letters*, 516, 66–76. https://doi.org/10.1016/J.EPSL.2019.03.038

Yamamoto, M., Clemens, S. C., Seki, O., Tsuchiya, Y., Huang, Y., O'ishi, R., & Abe-Ouchi, A. (2022). Increased interglacial atmospheric CO2 levels followed the mid-Pleistocene Transition. *Nature* Geoscience, 15(4), 307–313. https://doi.org/10.1038/s41561-022-00918-1

Yu, S. Y., Fan, L., Zhang, Y., Zheng, X. T., & Li, Z. (2021). Reexamining the Indian Summer Monsoon Rainfall–ENSO Relationship From Its Recovery in the 21st Century: Role of the Indian Ocean SST Anomaly Associated With Types of ENSO Evolution. *Geophysical Research Letters*, 48(12). https://doi.org/10.1029/2021GL092873

Zhang, Y., Zhu, Z., Liu, Z., Zeng, Z., Ciais, P., Huang, M., et al. (2016). Seasonal and interannual changes in vegetation activity of tropical forests in Southeast Asia. *Agricultural and Forest Meteorology*, 224, 1–10. https://doi.org/10.1016/J.AGRFORMET.2016.04.009

Zhang, Y. G., Ji, J., Balsam, W. L., Liu, L., & Chen, J. (2007). High resolution hematite and goethite records from ODP 1143, South China Sea: Co-evolution of monsoonal precipitation and El Niño over the past 600,000 years. *Earth and Planetary Science Letters,* 264(1–2), 136–150. https://doi.org/10.1016/J.EPSL.2007.09.022